Tampere University

Noora Hytönen

EFFECT OF MICROSTRUCTURE ON BRITTLE FRACTURE INITIATION IN A REACTOR PRESSURE VESSEL WELD METAL

Faculty of Engineering and Natural Sciences
Master of Science Thesis
November 2019

ABSTRACT

Noora Hytönen: Effect of Microstructure on Brittle Fracture Initiation in a Reactor Pressure Vessel Weld Metal
Master of Science Thesis
Tampere University
Materials Science
November 2019

The weld can be the most life-limiting part in a reactor pressure vessel (RPV). During operation, the pressure vessel components are subjected to high temperature and neutron irradiation induced ageing, which cause embrittlement. The RPV head is only subjected to thermal ageing. Submerged arc welding method is commonly used in the construction of reactor pressure vessels. Welding is a complex process that often introduces inclusions and other second-phase particles in the weld, which play a role in brittle fracture. Non-metallic inclusions, such as oxides, are brittle particles that may initiate a cleavage fracture when the loading stress exceeds the critical stress at the crack front. Knowledge on ductile-to-brittle transition and all factors affecting that are a critical safety matter, and therefore understanding the fracture mechanics of an RPV is important.

A ferritic steel weld experiences a ductile-to-brittle transition, causing the metal to act brittle at low temperatures and ductile at elevated temperatures. Severe ageing is known to shift the transition temperature towards higher temperatures due to embrittlement. The brittle fracture must be avoided by securing that the weld metal remains ductile in all situations. Factors affecting the brittle fracture in RPVs have been researched, but more detailed knowledge on weld embrittlement in needed in order to increase the understanding of affecting parameters, and eventually increase the RPV life time and prevent the formation of brittle fracture.

This thesis is part of the BRUTE (Barsebäck RPV material used for true evaluation of embrittlement) project at VTT Technical Research Centre of Finland Ltd. The project belongs to the SAFIR2022 programme (The Finnish Research Programme on Nuclear Power Plant Safety 2019-2022). The aim of the thesis is to increase the understanding of factors affecting brittle fracture initiation in the RPV weld metal. The investigated material is from a decommissioned Swedish nuclear power plant reactor pressure vessel, Barsebäck Unit 2, which had been in effective operation for 23 years. The base material consists of standard bainitic pressure vessel steel and the weld metal is high in Ni and Mn. All the experiments were performed at VTT Centre for Nuclear Safety (CNS), pioneering the new laboratory facilities.

The experiments in this thesis concentrated on two main subjects, i.e., weld microstructure characterisation and brittle fracture mechanics. The general microstructural characterisation concluded that the weld is a high-quality weld throughout the wall thickness. The heat-affected zone (HAZ) consisted of fine-grained and coarse-grained regions. The solidification structure consisted of a typical multipass weld with as-welded and reheated regions. Acicular ferrite dominated the as-welded microstructure with some grain boundary ferrite between the columnar grains. Polygonal ferrite dominated the reheated microstructure with some grain boundary ferrite and acicular ferrite. The macro- and microhardness measurements of the weld showed homogeneous weld and the macrohardness profiles were plotted from the base material to the HAZ and to the weld metal. The transition temperature and ageing effect were determined by Charpy V-notch impact toughness test. The testing gave a transition temperature of -75 °C. In this thesis, the investigated fracture specimens were tested at low temperatures, i.e., in the brittle fracture regime. On all investigated brittle specimens the cleavage fracture initiated at a particle rich in Mn, Al, Si, and O, and the particle was always the largest at the area of a maximum crack driving force. No severe thermal ageing effect has been observed.

Keywords: pressure vessel steel, thermal ageing, weld microstructure, brittle fracture

TIIVISTELMÄ

Noora Hytönen: Reaktoripaineastian hitsausliitoksen mikrorakenteen vaikutus haurasmurtuman ydintymiseen
Diplomityö
Tampereen yliopisto
Materiaalitekniikka
Marraskuu 2019

Hitsausliitos on yksi reaktoripaineastian elinikää rajoittavimmista tekijöistä. Paineastian käytön aikana sen komponentit altistuvat korkealle lämpötilalle ja neutronisäteilylle, jotka aiheuttavat materiaalissa vanhenemista ja haurastumista. Reaktoripaineastian kansi altistuu pelkästään termiselle vanhenemiselle. Usein paineastioiden kokoonpanossa käytetään jauhekaarihitsausta. Hitsaus on monimutkainen prosessi, jonka myötä hitsiin muodostuu sulkeumia ja erkaumia, joilla on vaikutuksensa haurasmurtuman muodostumiseen. Epämetalliset sulkeumat, kuten oksidit, ovat hauraita partikkeleita ja saattavat ydintää lohkomurtuman, kun jännitys on suurempi kuin kriittinen jännitys särön kärjessä. Transitio sitkeästä käyttäytymisestä hauraaseen ja siihen vaikuttavat asiat ovat kriittisiä paineastian turvallisuudelle ja siksi reaktoripaineastian murtumismekaniikan ymmärtäminen on tärkeää.

Ferriittinen teräshitsi muuttuu sitkeästä hauraaksi lämpötilan laskiessa transitiolämpötilan alapuolelle. Voimakkan vanhenemisen tiedetään nostavan transitiolämpötilaa korkeampiin lämpötiloihin, mikä johtuu materiaalin haurastumisesta. Haurasmurtuman syntyminen tulee estää varmistamalla, että hitsi säilyy sitkeänä koko käytön ajan. Paineastiateräksiä ja haurasmurtumaan vaikuttavia tekijöitä on tutkittu, mutta avoimia kysymyksiä on vielä hitsin haurastumiseen vaikuttavista tekijöistä, jotta paineastian elinikää pystyttäisiin pidentämään ja murtuman muodostuminen voitaisiin estää.

Tämä diplomityö on osa Teknologian tutkimuskeskus VTT Oy:n BRUTE (Barsebäck RPV material used for true evaluation of embrittlement) projektia. Projekti kuuluu kansalliseen SAFIR2022 tutkimusohjelmaan (The Finnish Research Programme on Nuclear Power Plant Safety 2019-2022). Työn tavoite on lisätä haurasmurtumaan vaikuttavien tekijöiden ymmärrystä reaktoripaineastian hitsausliitoksessa. Tutkittava materiaali on käytöstäpoistetusta reaktoripaineastiasta ruotsalaisen ydinvoimalan Barsebäck 2 yksiköstä, joka on ollut toiminnassa yhteensä 28 vuotta. Perusmateriaali koostuu standardoidusta paineastiateräksestä ja hitsimetalli on niukkaseostettua terästä, jossa on korkeahko nikkeli- ja mangaanipitoisuus. Kokeellinen osuus työstä on tehty VTT:n Ydinturvallisuustalossa, ja työ on osa uuden laboratorion käyttöönottoa.

Diplomityön tutkimus koostuu hitsin mikrorakenteen karakterisoinnista ja haurasmurtumamekaniikasta. Yleisen karakterisoinnin mukaan tutkittu hitsi oli kokonaisuudessaan korkealaatuinen. Muutosvyöhyke koostui hienorakeisesta ja karkearakeisesta alueesta. Hitsi koostui monipalkohitsille tyypillisestä palkorakenteesta, jossa näkyivät sekä jähmettymisrakenne että uudelleen kuumennut alue. Jähmettymisrakenteesta suurin osa oli asikulaarista ferriittiä ja dendriittien välissä havaittiin raerajaferriittiä. Uudelleen kuumenneella alueella eniten oli polygonaalista ferriittiä ja jonkin verran raeraja- ja asikulaarista ferriittiä. Makro- ja mikrokovuuskokeiden perusteella hitsi on homogeeninen. Kovuusprofiili mitattiin perusmateriaalista muutosvyöhykkeeseen ja hitsiin. Transitionlämpötila ja vanhenemisen vaikutus määritettiin Charpy-V iskusitkeyskokeella. Tuloksista saatiin transitiolämpötilaksi -75 °C. Tässä diplomityössä tutkitut näytteet testattiin alhaisissa lämpötiloissa, eli transitiokäyrän haurasmurtuma-alueella. Kaikissa tutkituissa näytteissä lohkomurtuma ydintyi partikkelista, joka koostuu pääosin mangaanista, alumiinista, piistä ja hapesta. Ydintäjäpartikkeli oli kaikissa tapauksissa suurin yksittäinen partikkeli murtuma-aluella. Voimakasta termistä vanhenemista ei tulosten perusteella havaittu.

Avainsanat: reaktoripaineastia, terminen vanheneminen, hitsin mikrorakenne, haurasmurtuma

PREFACE

This thesis was executed at VTT Technical Research of Finland (VTT), and is a part of the BRUTE project (Barsebäck 2 RPV material used for true evaluation of embrittlement). BRUTE project is in the SAFIR2022 programme, which is funded by VYR (Nuclear Waste Management Fund), VTT Technical Research Centre of Finland and NKS (Nordisk Kärnsäkerhet). The amount of in-kind contribution from the BREDA project (Barsebäck REsearch&Development Arena) is substantial. The funding, access to plant relevant material and support from the funding organisation is highly appreciated.

The objective of the project and the thesis is to determine the mechanical and microstructural properties of Barsebäck 2 reactor pressure vessel weld. Another objective is to pioneer the new laboratory facilities of VTT Centre for Nuclear Safety (CNS). This thesis concentrates on the brittle fracture mechanics and the weld microstructure effect on it.

I am grateful to VTT for the opportunity of writing my Master Thesis. I would like to thank my supervisors at VTT, Ulla Ehrnstén for the great advice and guidance and Jari Lydman for all the support since the day one. Thanks to those in the team of Nuclear reactor materials who took part in the experimental part of the thesis and the project. Special acknowledgements to Johanna Lukin for the sample preparation and guidance in the hardness measurements, Pentti Arffman for the CVN testing, and Zaiquing Que for the inclusion analysis. I want to thank Pekka Nevasmaa for guidance in the welding metallurgy. I am thankful for the endless support from my colleagues at VTT, I could not have imagined a better place to write a thesis. I would also like to thank Professor Pasi Peura and Professor Veli-Tapani Kuokkala from Tampere University for valuable instructions, guidance and grammar check.

Thanks to my family for being my family, and thanks for the unconditional support. Special thanks to Tomi for encouraging me to do my absolute best and to aim higher than I ever believed I could achieve.

Espoo, 1st November 2019

Noora Hytönen

CONTENTS

LIST OF FIGURES

LIST OF TABLES

LIST OF SYMBOLS AND ABBREVIATIONS

$\mathbf{A_{c1}}$	critical temperature above which austenitisation begins
$\mathbf{A_{c3}}$	critical temperature above which steel is fully austenitised
$\mathbf{A_{e3}}$	full austenitisation temperature at equilibrium
$\mathbf{K_{IC}}$	critical stress intensity factor (MPa$\sqrt{\text{m}}$)
$\mathbf{K_I}$	stress intensity factor at Mode I loading (MPa$\sqrt{\text{m}}$)
$\mathbf{T_0}$	fracture toughness reference temperature, ASTM E1921 (°C)
$\mathbf{T_{28J}}$	28 J transition temperature (°C)
$\mathbf{T_{41J}}$	41 J transition temperature (°C)
$\mathbf{T_{68J}}$	68 J transition temperature (°C)
$\mathbf{\Delta G}$	Gibbs free energy (J)
$\mathbf{\Delta T_e}$	equilibrium melting temperature (°C)
$\mathbf{\Delta T}$	undercooling (°C)
$\mathbf{\Delta t_{8-5}}$	cooling time over the temperature range 800–500 °C
σ	standard deviation
θ	solid-liquid contact angle
$\mathbf{m}$	Weibull modulus
AC	alternating current
APT	atom probe tomography
bcc	body-centred cubic
BM	base material
BREDA	Barsebäck REsearch&Development Arena
BRUTE	Barsebäck RPV material used for true evaluation of embrittlement
BWR	boiling water reactor
C(T)	compact tension
CCT	continuous cooling transformation
CE	carbon equivalent
CG-HAZ	coarse-grained heat-affected zone
CNS	VTT Centre for Nuclear Safety
CVN	Charpy V-notch

DBTT	ductile-to-brittle transition temperature
DC	direct current
EBSD	electron backscatter diffraction
EDM	electric discharge machine
EDS	energy dispersive X-ray spectrometer
EFPY	effective full power years
fcc	face-centred cubic
FEG	field emission gun
FG-HAZ	fine-grained heat-affected zone
FIB	focused ion beam
HAZ	heat-affected zone
LOM	light optical microscopy
MC	Master Curve
MMA	manual metal arc welding
NPP	nuclear power plant
OES	optical emission spectroscopy
ppm	parts per million
PWHT	post-weld heat treatment
RPV	reactor pressure vessel
SAW	submerged arc welding
SEM	scanning electron microscopy
SMAW	shielded metal arc welding
STEM	scanning transmission electron microscopy
TEM	transmission electron microscopy
VTT	VTT Technical Research Centre of Finland Ltd
WM	weld metal

1 INTRODUCTION

Reactor pressure vessel (RPV) steels have been under extensive research over decades in terms of radiation effects and fracture mechanics. During the operation of a nuclear power plant (NPP), the pressure vessel is subjected to thermal loading and neutron irradiation, which both cause ageing induced embrittlement in the steel. A ferritic steel weld is the most life-limiting area in this type of a reactor pressure vessel, as the fracture mechanics plays an important role in the safe performance of a pressure vessel. Welding is one of the main joining methods in structural components due to its effective process, integrity, and reliability. However, a weld in an RPV introduces discontinuities in the otherwise consistent structure. The welds are susceptible to flaws and residual stresses due to complex metallurgical process, and are therefore more prone to structural failure than the matrix material [1]. The ductile-to-brittle transition in ferritic steels is a key matter in structural integrity assessment [2]. Hence, the fracture mechanics on welds is more complicated than in homogeneous metals and non-welded parts.

1.1 Background of the Project

The reactor pressure vessel is a cylindrical vessel containing e.g. the reactor core. The investigated Barsebäck nuclear power plant was a boiling water reactor (BWR). Typically, reactor pressure vessels are constructed of bainitic low-alloyed low-carbon steels with austenitic stainless steel cladding on the inner wall side to minimise corrosion. The weld in this design is of high-nickel low-carbon steel filler metal. The exposure to high pressure, elevated temperature, and neutron irradiation may cause material degradation in the pressure vessel weld metal [3]. Furthermore, the safety of the component is of a high importance.

This thesis is part of the project Barsebäck RPV material used for true evaluation of embrittlement (BRUTE) at VTT Technical Research Centre of Finland Ltd. The objective of the project is to determine the properties of a real pressure vessel and compare it to the idealised ageing management programme, i.e., survaillance program. Furhter the project will enable increased understanding of factors affecting brittle fracture after thermal ageing of pressure vessel steel weld, and in future studies also continue the investigations on irradiated material. The investigated materials in this thesis are trepans cut from the decommissioned Swedish Barsebäck Unit 2 boiling water reactor nuclear power plant, which has been operating for total of 28 years and 23 effective full power years (EFPY).

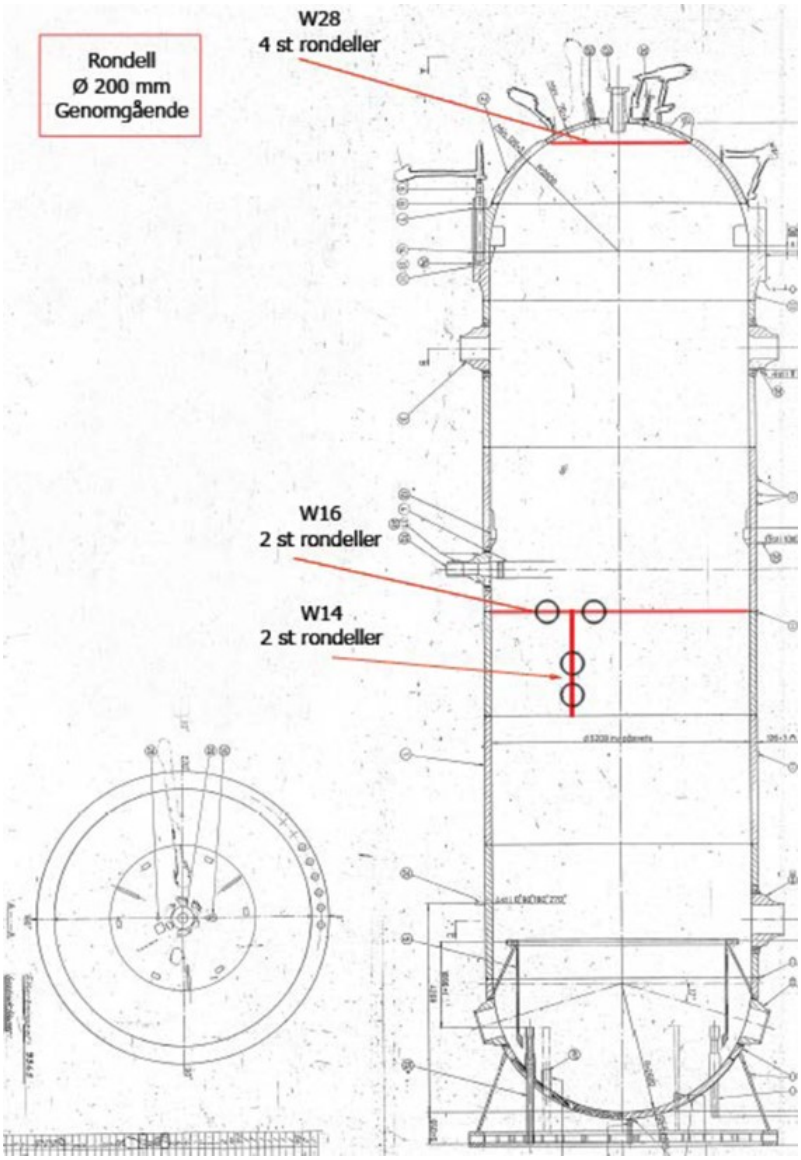

Figure 1.1. *Drawing of the Barsebäck 2 RPV showing the locations of all trepans cut from the welds [4]. The investigated trepans are from the head weld W28.*

The trepans have been removed from the head region of the reactor pressure vessel and they have diameter of 200 mm with full wall thickness. The RPV in question is shown in Figure 1.1, where the investigated weld is the W28 head weld. Both sides of the weld joint are investigated as the head is constructed of forging on the upper side and plate material on the bottom side. The possibly contaminated stainless steel cladding on the inner wall side has been removed from the surface of the trepans. The material characterisation includes both microstructural and mechanical aspect. All specimen preparation and testing in the BRUTE project is performed at VTT Centre for Nuclear Safety (CNS) laboratory. The project also provides the commissioning of the new laboratory and hot cells to prove its competence to the industry. The BRUTE project is part of the SAFIR 2022 programme, which is a national research programme launched for nuclear power plant safety. The material is provided through a broader Swedish project called BREDA.

The studied material is a low-carbon steel weld with nickel and manganese alloying. According to literature and surveillance experiments, the thermal ageing is known to cause embrittlement in the high-nickel weld metal. For reference studies, surveillance programs have been made to simulate the irradiation and ageing processes on the same material. In a welded RPV structure, the weld seams are the most critical parts in terms of the ageing effects, hence the characterisation is focused on the welds.

1.2 Scope of the Thesis

The research question of the thesis describes key issues delivered in the BRUTE project. The aim is to respond to the question of the effect of thermally aged RPV weld microstructure on the brittle fracture initiation, and whether there is a significant effect of thermal ageing on the steel weld after operation. According to the literature, the alloying elements and inclusion formation during welding produces discontinuities in the weld, and there is a shown correlation between the microstructure and brittle fracture [5]. Hence, this thesis contains two objectives, i.e, the weld metallurgy and brittle fracture mechanisms. The investigations concentrate on the cause of fracture initiation in a brittle fracture regime and to see the possible correlation with the weld microstructure. Similar studies have been made on pressure vessel steels of different operating condition. Often the microstructural characterisation concentrates on the nanoscale and nano-sized particles, but the micro- and macroscale are considered just as important.

The thesis begins with a literature review on the background theory of low-alloy steels, welding methods, and welding metallurgy. The second part of the theory includes the brittle fracture mechanisms in steels, covering the Griffith crack theory, ductile-to-brittle transition, and the brittle fracture initiation and its characterisation methods. The experimental methods and materials are given in Chapter 4, and the results of the experiments are delivered in Chapter 5. The obtained results and the completed investigation is discussed in Chapter 6 in correlation with the literature and previous experiments in the surveillance programmes. Future aspects are also discussed in the end of the thesis, since the investigations continue in the BRUTE project.

2 WELDING OF LOW-ALLOY STEELS

The base material in this study is a bainitic carbon-manganese low-alloy steel suitable for a reactor pressure vessel, which consists of plates and forged parts that are welded together. The requirements for the mechanical and physical properties of RPV steel materials are very high. Structural steels with high strength and high toughness have characteristic fine and uniform grain size [6]. In this chapter, the properties and chemistry of steel and weld materials are introduced. Also the welding processes and microstructures are described in detail.

In steels, carbon and other alloying elements have a significant effect on the phase transformation temperatures. In the formation of low-alloy and bainitic steels, carbon stabilises austenite with its higher solubility to it than to ferrite, which hence has slower reaction kinetics. Because of this, to some extent, carbon favours the formation of lower bainite. Although ferrite formation is rapid, alloying elements such as manganese and molybdenum promote the lower bainite formation during relatively rapid cooling. Due to the ferrite formation and adjacency of martensite reaction, it is rather difficult to form a fully bainitic structure. Very small additions of e.g. boron retard the ferrite formation to allow a near fully bainitic phase structure. The bainitic steels have relatively high-strength and low alloy concentration, where the latter improves the weldability and favours the tough acicular ferrite in the weld. [7] This subject is discussed further later.

Weldability in steels means the ability of a metal to be welded into a particularly and appropriately designed structure under specified manufacturing conditions and to perform sufficiently in the intended service. Thus, it is described in terms of how well the material withstands the thermal cycles from welding without significant degradation in properties of the weld and heat-affected zone (HAZ). Therefore, steels with good or excellent weldability have characteristic features such as low carbon content and reasonable alloying such that the phase transformations as well as grain growth are controllable. [8] Carbon affects significantly the microstructure when heating is involved. The carbon content must be taken into consideration especially in high-strength steels due to the possible formation of martensite. Theoretically, the carbon content of the steel is directly proportional to the hardness of martensite forming during sufficient cooling. The high hardness again, may cause brittleness in steels. The main concern with the large amount of martensite formation is the cold cracking caused by hydrogen in the iron lattice. In general, the risk for hydrogen embrittlement is greater the higher the hardness of the steel is. [6]

Welding includes a variety of processes for different materials and applications. The

methods can be classified by fusion or non-fusion, heat and pressure input, energy source and transfer types, and several other properties. Since there are many varieties within the methods, in this chapter only the methods used in this project are presented and discussed in more details. In fusion welding, sufficient melting is involved to form an atomic bond between the joint interfaces. Usually, the base material is melted and combined with a possible filler material. The process heats material locally above the melting point followed by solidification and cooling. The steel is subjected to severe thermal cycle as the steel reaches its melting point at the fusion line. The cooling rate is very high for most welding methods, which impacts the phase transformations and causes changes in the thermal and mechanical stress states. Additionally, further from the melted region, the temperature rises high enough to cause solid-phase transformations which are observed as e.g. changes in the substructure or grain size [9].

The main subject of this thesis is the weld of the head of the reactor pressure vessel, which consists of two high nickel filler materials. The base materials are SA 533 Grade B Class 1 plate and SA 508 Class 2 forging steel. In a welded component, the weld is typically the most prone part to deterioration. Generally, any discontinuity in the weld material microstructure is a possible initiation site for a fracture prior to the material's theoretical strength. Furthermore, some ageing phenomena are stronger in the weld metals than in the base materials. Therefore, the microstructure and fracture mechanics of the weld are more important when investigating the toughness and mechanical durability of an RPV.

2.1 Submerged Arc Welding

The submerged arc welding (SAW) process has a characteristic feature of a granular flux and molten slag covering the weld area. A continuous filler metal wire electrode is fed through the blanket of the granular flux to generate the arc to form the molten pool that is a mixture of the slag and the weld metal [10]. The principle of submerged arc welding is shown in the schematic in Figure 2.1. As the molten pool forms and solidifies, the lighter molten flux rises above the solidifying weld metal and forms a protective solid slag. After cooling, the solid slag is removed from the weld. The flux provides several advantages in the process compared to e.g. open arc welding, and produces high quality and clean weld joints. The advantages include high deposition rates, elimination of spatter and heat losses and prevention of arc radiation and sparks. It reduces the fumes generated during welding, and the contamination by impurity gases such as oxygen, nitrogen, and sulphur, and even hydrogen are low. [11] No shielding gas is needed due to the separation of molten metal from the air. To further increase the deposition rate, volatile alloying elements and metal powders can be included in the granular flux, and two or more electrodes can be used simultaneously. [10] The process can be fully automatised with typical usage of direct-current electrode positive and the flux can be reused after removal.

In joints involving several weld passes, the slag must be removed between each pass, which is an extra step in the process compared to open arc methods. Although the flux

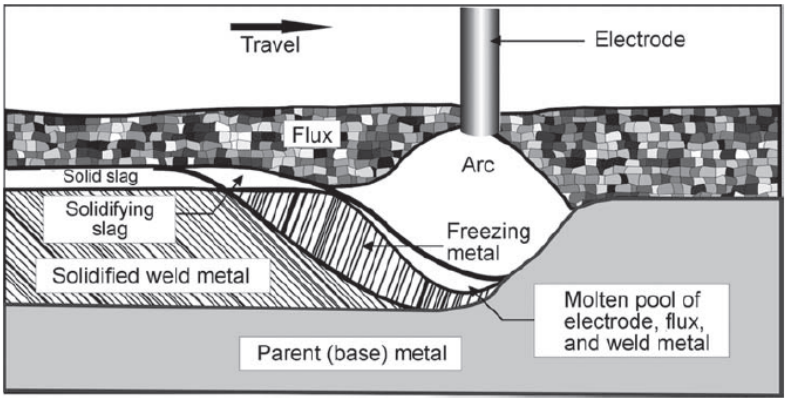

Figure 2.1. *Principle of the submerged arc welding and the weld pool formation. [11, p.335 Fig.2]*

protects the weld from major impurities and oxidation, some defects can still occur. An improper bead placement may cause lack of fusion or slag entrapment. Weld solidification cracking in the weld centre line is a problem especially with high-strength materials and is usually caused by excessive shrinking at solidification. If the bead shape and the joint design are poor, solidification cracking may be an issue. Hydrogen-induced cracking usually does not appear immediately after welding but even several days later. When combined with martensitic microstructure and residual stresses, hydrogen in the weld area may be detrimental [12]. Porosity due to entrapped gases is unlikely to occur due to the protective flux, but the lack of protection or other contaminants such as water and oil may still cause porosity in the weld. [11] Submerged arc welding is suitable in flat and horizontal positions and used in circumferential welding due to the effects of gravity on the molten slag and weld pool [9, 10]. In a double V-grooved weld joint, two thick plates are welded together by SAW. One side is first welded with multiple passes, after which the root is ground off to avoid lack of fusion or other weld defects. After this, the plates are welded from the other side of the plates to make an "X"-groove weld. This type of weld can be seen for example in very thick steel plates in pressure vessels.

Due to the high heat input and high deposition rate, the SAW method is most commonly used for thick steel plates and forgings, such as pressure vessels. In low-alloy steels in the heat-affected zone, the high heat input may cause grain growth, yet the low heat input causes undesirable excessive hardness and therefore is an important parameter in the process. Additionally, SAW is only suitable for ferrous metals and not for materials such as aluminium alloys.

2.2 Manual Metal Arc Welding

Another method used in the welding of an RPV head is the manual metal arc welding (MMA). The MMA method is also known as shielded metal arc welding (SMAW), and it is one of the most used electric arc welding processes. The filler material is a covered

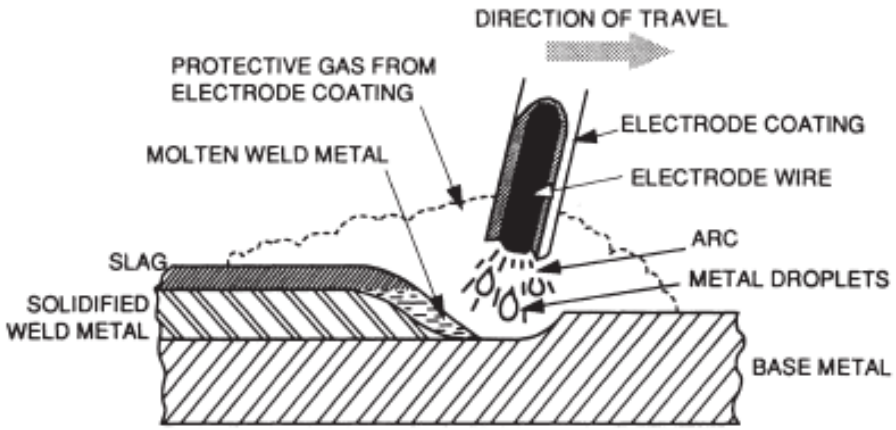

Figure 2.2. *Principle of the manual metal arc welding and the weld pool formation. [13, p.302 Fig.1]*

electrode, and the arc is generated between the electrode and the base material. A protective gas forms by the decomposition of the flux-covered consumable electrode stick, which shields the weld pool and the molten metal. The initiated arc melts the filler material at the tip of the electrode and the surface of the base materials. The molten filler material is transferred to the weld pool to form a weld deposit. The electrode coating forms a protective slag on top of the solidified weld metal. [13] The principle of the weld pool formation is presented in the Figure 2.2 schematically.

The MMA process is highly dependent on the operator skills, although it is in principle a simple method and easily available. The method is suitable for both ferrous and non-ferrous materials, and several different consumables can be used. Additionally, it is not limited by the base material geometry or thickness. However, the consumable electrode must be periodically replaced and the slag removed and cleaned, breaking the continuous welding process. In electric arc welding, the polarity has an effect on the depth of the weld pool, especially when direct current (DC) electrode is used. With negative polarity the weld is narrow and deep and with positive polarity the weld is wider and shallow [10]. Alternating current (AC), results in intermediate weld depth and width. The weld quality depends on the accessibility of the joint, welder skills, and the electrode. Poor quality may be due to difficult joint design, improper cleaning between beads, insufficient fusion or location of weld, and poor core wiring in the electrode. Wrong polarity or severe magnetic arc blow may cause spatter and an incomplete fusion due to an interaction between the magnetic fiend and the work piece. However, excellent quality can be achieved by MMA and it can therefore be successfully used also in several high-requirement weld parts such as reactor pressure vessels. [13]

2.3 Welding Metallurgy

During a multipass welding process, the materials are subjected to several thermal cycles, which can cause phase transformations and changes in the grain size and structure, appearing as distinct regions in the microstructure close to the weld and in the weld metal. The weld microstructure is characteristic to the metal as its final formation depends on alloying, austenitisation temperature, and the rate of heating and cooling. The basic structure of a weld can be divided into the fusion zone, the partially-melted zone, and the heat-affected zone, as presented in Figure 2.4. Typical microstructural changes in the heat-affected zone for a low-carbon Mn-alloyed steel during welding are recrystallisation, grain growth, and ageing. The most critical of these transformations is the grain growth, since it increases the hardenability of the HAZ and decreases the toughness of the metal. To prevent excessive grain growth at high temperatures, for instance fine TiN precipitates can be introduced in the material because of their ability to remain stable at high temperatures and act as barriers to grain growth during welding. [6] The chemical composition of the weld metal is controlled in order to obtain good weldability and the desired microstructure and mechanical properties, i.e., fine-grained and homogeneous acicular ferrite.

In low carbon steels, small carbon concentration variations can have a significant impact on the weld microstructure. With decreasing carbon concentration the sensitivity of growth kinetics increases the isothermal growth rate of Widmanstätten ferrite laths nearly exponentially going from about 0.1 to less than 0.05 wt% of carbon. Furthermore, the ferrite growth rate increases when the carbon concentration approaches its solubility in ferrite. [7] However, it is worth noting that the large Widmanstätten ferrite laths may lower the toughness and initiate cracks more easily than e.g. acicular ferrite plates [8].

Similarly to the base material, the filler alloy must be designed for welding. The filler metal alloys are composed such that the best possible microstructure is achieved while keeping the weldability at a reasonable level. In commercial steels, manganese, silicon, nickel and molybdenum are the most common alloying elements present. Alloying metals such as manganese and nickel are relatively large in atom size, and therefore they reside in the iron lattice as substitutional solid solution atoms and not as interstitials like carbon. In a low-carbon steel filler metal, manganese is an important element stabilising austenite and promoting refined acicular ferrite formation at approximately 1.5 wt% additions [14]. Manganese also has a deoxidising effect and it combines with the undesirable sulphur, forming manganese sulphides. Silicon acts as a deoxidiser similar to manganese. In bainitic steels, a relatively large silicon concentration prevents cementite formation. Since carbon content in weld metals is limited, additional strengthening elements must be added. Silicon and molybdenum are effective strengtheners of ferrite, as well as manganese and nickel. Even in low-alloy low-carbon steels they are efficient strengtheners due to their grain refining potential. However, the concentrations of interstitial solutes such as carbon and nitrogen have an impact on the strengthening. Sulphur and phos-

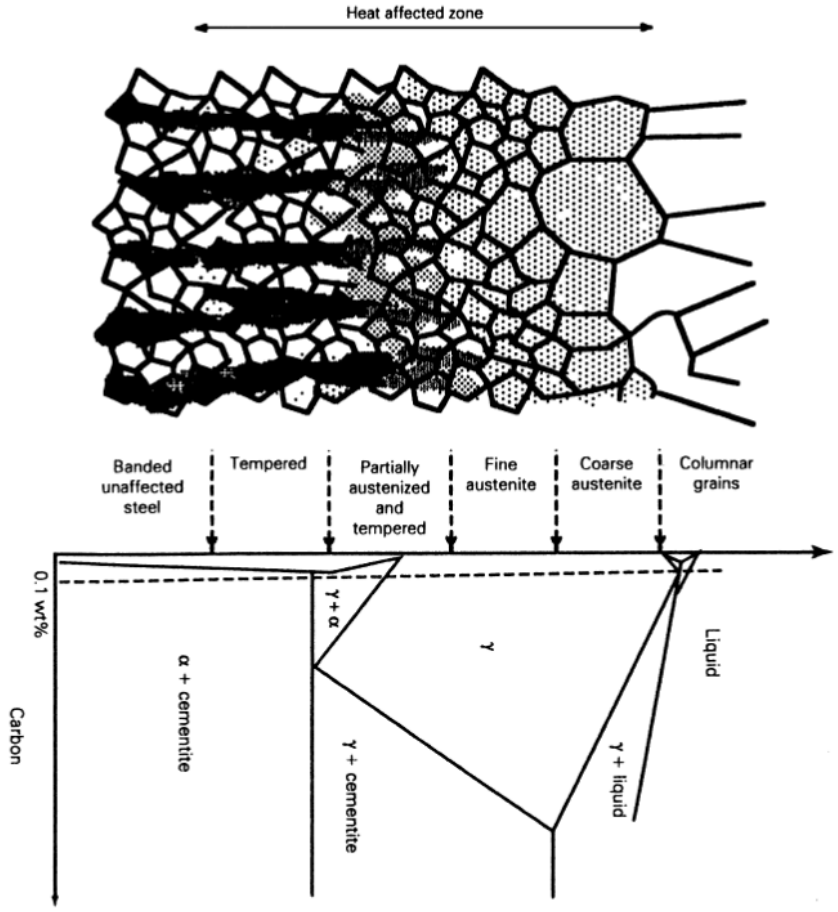

Figure 2.3. *Schematic presentation of the microstructure of the heat-affected zone in relation to a iron-carbon phase diagram [7, p.390 Fig.13.13].*

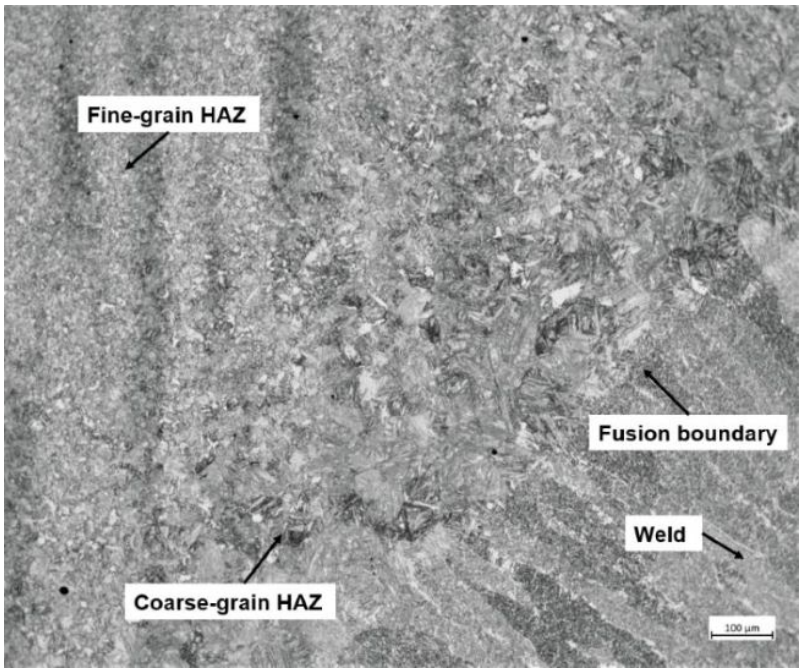

Figure 2.4. *Light optical microscopy image of the weld structure. From the top left to the bottom right: the fine- and coarse-grained heat-affected zones and the fusion zone.*

phorus are impurities and have an ability to segregate at the grain boundaries at higher temperatures and cause brittleness. [7] Nickel increases the proportion of acicular ferrite instead of grain boundary ferrite. However, excessive amount of nickel promotes martensite formation. If the manganese content is maximum 1.8 wt%, the amount of martensite increases when the nickel content is above 2.2 wt%. Boron has a low atomic weight so that, in terms of normal weight percentage, very small additions of boron are already effective. [15] Boron prevents phosphorus segregation at the grain boundaries, increases hardenability, and in a molybdenum containing steel also retards ferrite formation and promotes the bainite reaction [6].

When a steel is loaded over its yield point, the metal begins to deform due to the activation of dislocation movement, and the flow stress start to increase as the metal strain hardens. If the steel is unloaded and reloaded immediately, the strain hardening continues without a sharp yield point. If the loading is paused during deformation and left to age before reloading, interstitial atoms such as carbon and nitrogen diffuse even at low temperatures into the generated dislocations. At reloading, a new sharp yield point occurs at a higher stress, i.e., the yield strength and the ultimate strength have increased from the previous ones and elongation and reduction of area are decreased. The described phenomena is also known as strain ageing. [16] Carbon and nitrogen are inevitable in the steel and the weld metal. To prevent excessive strain ageing, small amounts of strong nitride formers such as aluminium or titanium may be added, which reduces the free nitrogen concentration in the solution to a very low level. Aluminium is also a grain refiner and an effective deoxidiser, and therefore the steels are often called "aluminium-killed" steel. In weld metals, high carbon concentration causes formation of cracks in the weld zone due to the hardenability effect. [7] The ability of forming martensite, i.e., hardenability, can be described by the carbon equivalent (CE), which can be calculated from the chemical composition of the steel. The CE describes the steel's hardenability, thus also indirectly its susceptibility to hydrogen embrittlement and further weldability. [12]

Hydrogen-induced cracking is often linked with welds in low-alloy steels. Generally, hydrogen must be taken into serious consideration in the brittle fracture assessment. In welding processes, hydrogen is always present in material fluxes, electrode surfaces, and gases involved, from which hydrogen easily diffuses to the heat-affected zone and weld metal during the cooling cycle. Hydrogen solubility is much higher in the molten than solid iron and the solubility in the solid steel decreases with temperature [8]. Furthermore, the solubility of hydrogen is much smaller in martensite than in ferrite and thus, in the case that martensite forms, hydrogen concentrates at the phase or inclusion boundaries. The highest risk is with untempered martensite, which is harder and more sensitive to embrittlement than tempered martensite. The hydrogen embrittled microstructure combined with residual stresses from the thermal cycles causes a high risk for crack initiation. In order to control the amount of hydrogen in the process and the weld, the microstructure formation and cooling cycle must be carefully regulated. [6] In favourable conditions, the highly mobile atomic hydrogen concentrates in the discontinuities and fissures. In the thermal cycles during solidification and solid-state transformations, hydrogen accumulates at the

existing defects, which are then enlarged and the consequent volume changes cause internal micro-cracks. The formed micro-cracks with sharp tips involve also high stress concentrations, where additional atoms further gather. The stresses caused as described are relieved as the cracks extend and possibly continue until failure. Thus, it can be concluded that hydrogen-induced cracks occur by distinct steps. The diffusible hydrogen that has dissolved in the steel plays an important role in hydrogen embrittlement. First, the more hydrogen is dissolved, the less stress and time are required to initiate a crack. Second, the microstructure of the steel in the weld affected area affects the material's susceptibility to hydrogen-induced cracking. For example, martensite with higher carbon content is the most problematic concerning hydrogen, showing high brittleness compared to a bainitic steel with lower strength and acicular microstructure. [8] Methods for lowering the risk of hydrogen embrittlement are preheating the work piece, to maintain sufficient interpass temperatures during welding, and post-weld heat treatment (PWHT) to remove hydrogen.

As mentioned in Chapter 2.1, the submerged arc welding process decreases the hydrogen contamination during welding because the molten metal, which has high hydrogen solubility, is protected from the surrounding air and other possible external impurities by the flux. Another method that decreases the susceptibility to hydrogen-induced cracking is the microstructure control, where martensite formation is avoided and bainite formation promoted. Also the amount of residual stresses can be minimised by a post-weld heat treatment. A high-temperature tempering may, however, allow hydrogen to diffuse to the bulk or to the surface where it can recombine and evaporate as a gas. [8, p.388]

2.3.1 Weld Microstructure

The weld region can be divided into two main areas, the fusion zone and the heat-affected zone. Their metallurgy is very different from each other by the phases present as well as the grain size and the microstructure. The fusion zone forms from the melt of the filler material and the base material, and is a solidification microstructure. The heat-affected zone is a region which has been affected by the thermal cycles and the high temperature of the welding process, which has caused possible phase transformations and changes in the grain sizes without melting the material. As the weld solidifies and cools down, there is a possibility for a whole variety of phase transformations of the steel to occur. [7] Metals that are strengthened by e.g. work hardening or precipitation hardening can be affected significantly during welding, as the high temperature in the heat-affected region reduces the strength by microstructure changes [10].

To understand the phenomena of microstructure formation during cooling, it is important to examine the temperature range of 800 to 500°C on a continuous cooling transformation (CCT) diagram. The cooling time in this temperature range determines the microstructure the steel obtains during the solid-state transformation, which further will establish e.g. its cracking sensitivity. The maximum resistance to cracking is achieved by reducing the

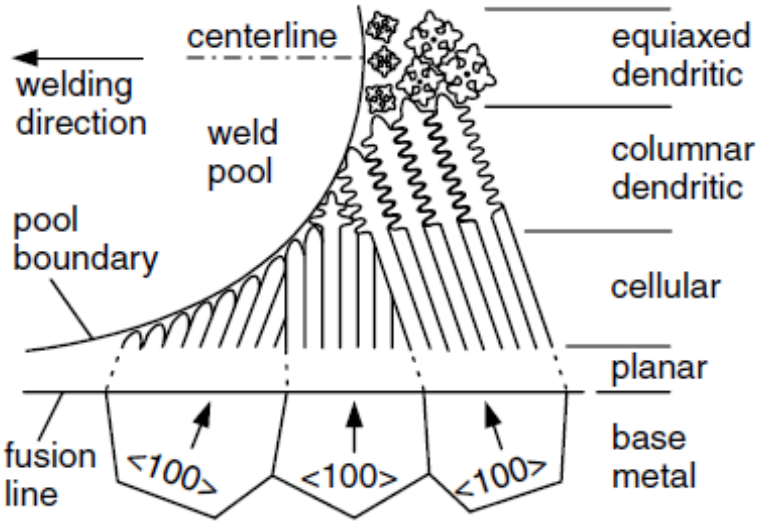

Figure 2.5. *The solidification modes across the fusion zone behind the weld pool: planar, cellular, columnar dendritic, equiaxed dendritic. Additionally, the epitaxial growth is schematically shown. [10, p.202 Fig.8.5]*

amount of untempered martensite. [8, p.387] During cooling in the temperature range from 800 to 500 °C, several factors affect the microstructure development such as the cooling time (Δt_{8-5}), steel alloying, oxygen content, and austenite grain size [10]. These factors will be discussed in more detail later.

The Fusion Zone

The solidification product of steel depends on the thermodynamics and kinetics, including phase development, diffusion, undercooling, fluid flow, and so on. There are different solidification modes at the solid-liquid boundary that are affected by temperature gradients, cooling rates, and growth rates in a complex way for alloy steels. For a heterogeneous melt the different morphologies are planar, cellular, columnar dendritic, and equiaxed dendritic. [10] These modes are schematically presented in Figure 2.5.

The different solidification morphologies and microstructure developments are determined by the extent of undercooling [17]. Undercooling, ΔT, is defined as how far the metal remains liquid below its equilibrium melting temperature, T_e. The driving force for solidification and growth increases with decreasing temperature, as the free energy ΔG is low at larger undercoolings and therefore the energy barrier for nucleation is low. At the equilibrium melting temperature, there are barely no sites for the nucleation of a solid phase. The atoms in front of the solid-liquid-interface are pushed further from the boundary as the solidification gradually begins. The alloy composition changes at the solidification front, and a local solidification temperature exists where the solid and liquid in contact are in equilibrium. In a heterogeneous melt, undercooling arises from the compositional effects and is therefore called constitutional undercooling. In these conditions, the undercooling is usually only a few degrees due to the inclusions and interface that act as nucleation

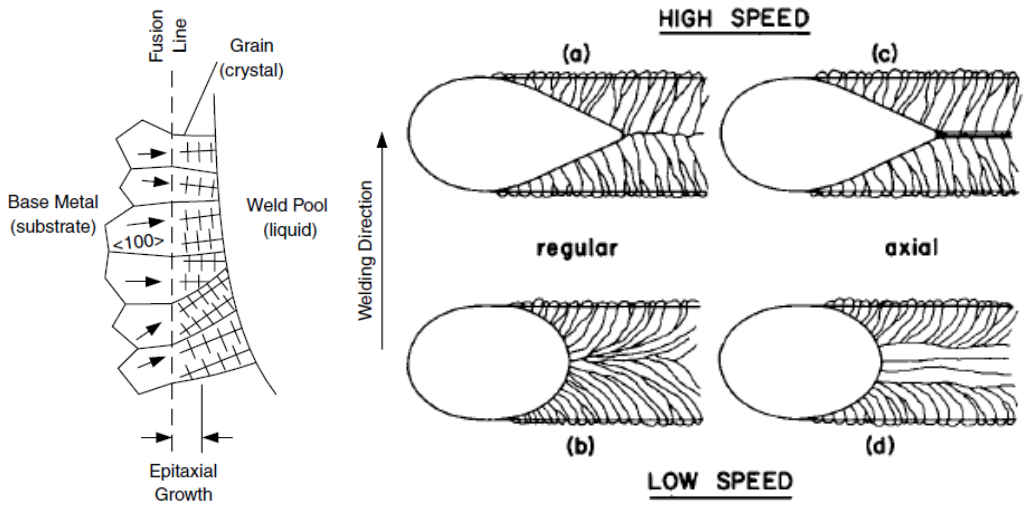

Figure 2.6. *On the left: Epitaxial growth near the fusion line and weld pool. On the right: Effect of travel speed on the weld pool shape and the columnar grain growth. Axial grains may initiate in the middle of the fusion zone and the speed of the weld pool affects the width of the region of the axial grains. [10]*

sites and dendritic morphology is promoted. However, at too large undercoolings, the diffusivity is decreased so much that the atoms are immobilised at the solidification front, stopping the solid formation. [6] During slow cooling, large undercoolings suppress the heterogeneous nucleation by kinetic control, and at rapid cooling rates the solid growth is restrained [17].

During welding, the heat source moves continuously, and therefore the extreme temperature gradient is changing direction and the growing columnar crystals follow the heat flow retaining the preferred $\langle 100 \rangle$ directions. This gives a characteristic shape for the columns in a weld bead with a centre line at the middle of the molten pool. The so-called epitaxial growth is shown in Figures 2.5 and 2.6. The shape of the weld pool is dependent on the welding travel speed, with increasing speed changing from elliptical to a teardrop shape. Due to the effect of a steep temperature gradient and hence the weld pool shape, the solidification and crystal growth behaviour can be controlled. The teardrop-shaped weld pool maintains a constant thermal gradient from the centre line to the boundary of the base material. The crystals need not to change the growth directions as at slower speeds, and the preferred orientation is retained throughout the solidified weld bead. For example in submerged arc welding, the teardrop-shaped weld pool is achieved. [6] The travel speed effect is shown in the Figure 2.6. The axial grains, that can grow in the middle of the fusion zone perpendicular to the trailing pool boundary, have been seen in e.g. aluminium alloys and austenitic stainless steels [10].

The whole solidification process begins with nucleation at a suitable site where the liquid wets the substrate. At complete wetting, the solid-liquid contact angle θ is zero and the energy barrier ΔG is at minimum. Hence, the crystal can nucleate without overcoming any energy barrier required for nucleation with very little undercooling. The solid base material at the fusion boundary serves as a substrate for the melted weld metal in nucle-

ation. Since the liquid metal is in bordering contact with the solid grains, and the filler and the base metal have similar compositions, the wetting is nearly complete. In the fusion welding of thick steel plates, the base material drops the temperature of the melt very effectively. [6, 10] The solidification of an alloy is not homogeneous nor under equilibrium conditions. The contact between the filler metal and the base material will initiate mixing of the metals and dilution of the filler material. Although the dilution is not significant, the composition of the melt is changed, the presumably oxidised base material surface is removed, and the melt cools down. [6]

The two major regions, the fusion zone and the HAZ, are divided by a fusion line. At this boundary between solid and molten metals, the solidification begins from the hot parent plate surface and grows epitaxially as columnar δ-ferrite since the existing crystallographic orientation of the solid is not altered [10]. The forming grains are anisotropic as they continue growing into the liquid in the direction of heat flow, which is perpendicular to the pool boundary. In body-centred cubic (bcc) and face-centred cubic (fcc) metal crystal structures, the grains with $\langle 100 \rangle$ directions parallel to the heat flow direction grow fastest and suppress the growth of less favourably oriented grains. [7] Therefore, the width of the columns increase with the distance from the fusion line. For low-carbon steel, the solidification starts by the formation of δ-ferrite followed by solid-state transformation to austenite and reverting back to ferrite on continued cooling. The low alloying concentration does not change the crystal structure from that of pure iron. [10]

The austenite nucleates at the ferrite grain boundary and grows into a columnar structure [7]. In the steel solid-state phase transformations during cooling, the austenite microstructure determines the resulting grain structure and has a high importance in heating, cooling, and solidification. The increasing austenite grain size results in a smaller amount of grain boundary nucleation sites, and therefore, hardenability increases with coarser grains. With columnar grains, the smaller amount of grain junctions increases hardenability compared to the equiaxed grains of wrought alloy [7]. However, since the nucleating grains inherit the orientation of the parent phase, it also means that the base material determines the grain size of the solidifying melt. Because the base material is under severe thermal loading, the parent grains become coarser and the weld microstructure has relatively large grains. Ferrite can also nucleate within the austenite grains at inclusions and dislocations, forming plate-like precipitates at larger undercoolings. With fine austenite grains, ferrite growth from grain boundaries pushes carbon to diffuse in the interior of the grains, reducing undercooling and complicating the nucleation. However, with coarser austenite grains, it takes more time to reject carbon and to diffuse into the interior of the grain, which increases the probability of intragranular precipitates to nucleate. [6]

When the weld metal cools from the liquid phase to atmospheric temperature, it obtains a primary or as-deposited microstructure. The main types are grain boundary ferrite, Widmanstätten ferrite, and acicular ferrite. Other cooling products such as martensite and retained austenite may be found in the microstructure as microphases in very small

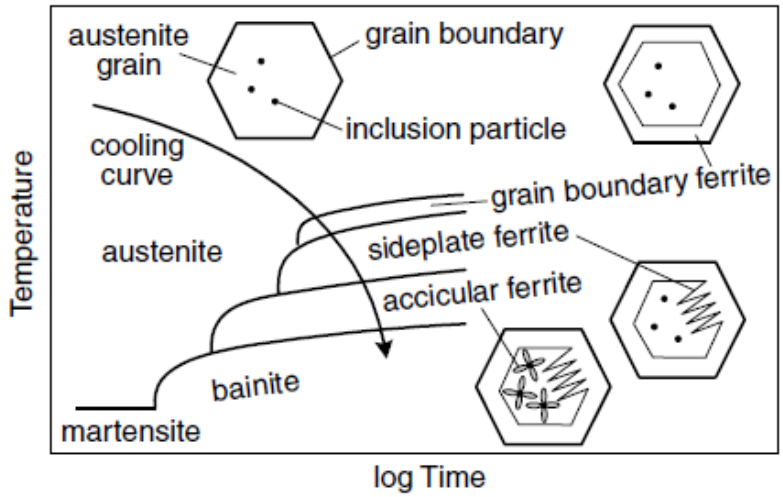

Figure 2.7. *Schematic continuous cooling transformation diagram for weld metal of low-carbon low-alloy steel. [10, p.232 Fig.9.21]*

amounts. In well designed continuous cooling transformation of the weld metal, bainite is unlikely to form while acicular ferrite nucleates fast on the surface of non-metallic inclusions in a heterogeneous alloy steel. When welding a thick steel plate, several passes are welded, which creates a complicated sequence of thermal cycles and weld deposits. Therefore, only a part of each weld bead layer has a fully primary microstructure, since the following structures affect the previous layer and the high temperature heat treatment. These regions are called secondary or reheated microstructures. [7] In the reheated area, the ferrite takes partly a new form due to carbon partitioning. The resulting microstructure is called polygonal ferrite, since it has no regular shape but appears as large light-coloured regions in an optical microscope.

The first phase to form from an austenite grain below Ae_3 equilibrium temperature during cooling is grain boundary ferrite (α), which nucleates at columnar austenite grain boundaries and grows inward the grain [7]. This ferrite is also called allotriomorphic ferrite, since it does not have a regular shape indicating its internal crystal structure. The grain boundaries are generally efficient diffusion paths, and therefore the thickness of the grain boundary ferrite is controlled by the diffusion of carbon in the austenite. Considering isothermal transformation, the ferrite thickening rate decreases parabolically with time as the diffusion path increases with thickness. Alloying elements such as manganese stabilises austenite leading to smaller fraction of primary grain boundary ferrite [7]. As the distance for carbon diffusion increases, the undercooling increases as does the driving force for the transformation. Therefore, as the weld cools below 600°C, the temperature becomes too low for carbon to diffuse sufficiently and the growth of α-ferrite stops. The growth of ferrite therefore continues by non-diffusional transformation by growing Widmanstätten side-plate ferrite. [7] However, welding does not occur under isothermal conditions but the cooling rate and thus the ferrite formation are more complex. The development of the low-alloy steel weld metal microstructure is shown on a CCT-diagram in Figure 2.7.

When the grain boundary ferrite grows, the carbon moves ahead of the interface and gradually slows down the growth. At lower temperatures, in the case of Widmanstätten, carbon and iron do not diffuse but carbon undergoes partitioning and is accommodated at the sides of the growing plates. [7] Therefore, the tips of the Widmanstätten plates always confront fresh austenite and the growth rate is constant, since carbon diffusion does not limit the growth rate. Although the Widmanstätten growth rate is large for a typical weld metal, at even lower temperatures the competitive formation of acicular ferrite begins. The difference between these is that Widmanstätten grows at austenite grain boundaries while acicular ferrite nucleates at non-metallic inclusions. Therefore, the more there are inclusions compared to austenite grain nucleation sites, the larger fraction of acicular ferrite forms. For example, small austenite grains favour Widmanstätten formation and reduced oxide content decreases the content of acicular ferrite [7]. At lower temperatures, the acicular ferrite grows faster and has a randomly oriented shape of short needles, also described as a basket-weave structure. In low-carbon steel welds, acicular ferrite is found in the microstructure predominately. [10]

Considering a continuous cooling transformation diagram, the weld cooling time from 800 to 500 °C determines whether the microstructure contains predominately side-plate ferrite, acicular ferrite, or bainite, and what the fraction of grain boundary ferrite is. With increasing steel alloying, the CCT curve is shifted to longer times and lower temperatures, which means that there is more time for e.g. acicular ferrite to form and less rapid cooling is required. Also with increasing austenite grain size and hence reducing grain boundary area, it takes a longer time for ferrite to nucleate and a shift in the CCT curve is noticed. [10] On the other hand, increased oxygen content increases the amount of inclusions which, however, are small in size, which causes grain boundary pinning and hence inhibits grain growth. Therefore, the small grains have a large total boundary area, which favours the grain boundary ferrite. [18] Larger inclusions favour acicular ferrite formation, and therefore there is an optimum oxygen content (200-350 ppm) of the weld metal to predominately form acicular ferrite [19]. As mentioned before, acicular ferrite is desirable in welding due to its good toughness properties [20].

Below ca. 500°C, most austenite has been transformed and the remaining fraction is enriched in carbon. This leads to a phase transformation, at rapid cooling to martensite, or at slower cooling to degenerated pearlite and even retained austenite may be left. Due to their small volume fractions, they are called microphases and act as brittle inclusions in the weld. [7]

The Heat-Affected Zone

The region on the other side of the fusion boundary remains solid throughout the welding but is affected by the severe heating and cooling cycles that cause changes in its microstructure and mechanical properties. This region is therefore called heat-affected zone. The effect of the peak temperature and the heating rate on the microstructure de-

creases with distance from the fusion boundary [7]. However, the cooling rate can be defined as the time of cooling from 800 to 500 °C, Δt_{8-5}, which defines the temperature range for the austenite to decompose by solid-state transformations. This time period and the peak temperature are the most important parameters together with the interpass temperature that affects the HAZ formation. All the above parameters are proportional to the heat input.

Since the heat diffuses over a distance in the HAZ, the closest regions are subjected to more pronounced heat cycles. The HAZ can be divided into different microstructural zones due to the degree of heat-induced transformations. The highest-temperature regions are subjected to the austenite transformation temperature which starts from $Ac_1 \approx 800°$C and continues up to $Ac_3 \approx 950°$C. The closest zone to the fusion boundary is subjected to the highest temperatures, and the heating during welding exceeds Ac_3 with peak temperatures reaching temperatures above 1200°C. At such high temperatures, austenite is annealed and the driving force for grain growth is high, hence it effectively coarsens the grains. The region is thus called coarse-grained region. With increasing distance from the fusion boundary, the peak temperature decreases to only above the upper critical temperature Ac_3, and the grain size is refined abruptly. Accordingly, this region is called fine-grained region. The distinction is important since the mechanical properties differ largely between the fine- and coarse-grained regions. The next region reaches temperatures above the austenite starting temperature Ac_1, and therefore contain only partially refined grains. The furthest region is a tempered microstructure where the temperature does not exceed the Ac_1 temperature. [7]

Previously in the introduction of molten weld cooling transformations, the microstructure formation was described in terms of ferrite formation following the kinetic behaviour with undercooling. As the temperature drops, the diffusion rate decreases while the driving force for the transformation increases. The transformation during heating is different from this because both the diffusion rate and the driving force increase with temperature. Due to this, the grains closest to the fusion boundary transform fully to austenite approximately 100 °C above Ac_3, and when a very high peak temperature is approached, the grain coarsening is very rapid and effective. [7] For example in work-hardened metals, the hardening is caused by increased internal stresses and high energy is stored in the microstructure. When the temperature is increased, the driving force for energy release also increases, the stresses are freed, and the microstructure recrystallises. [10] Therefore, the transformation rate, as well as the extent of recrystallisation, increases with temperature. In microalloyed steels, the grain boundary pinning elements are dissolved before the grains begin to grow. However, the grain growth during annealing is exponential so that the grains grow extremely rapidly above the start temperature.

The mechanical properties of the coarse-grained region are important to take into account during welding design, since they differ from the properties of the base material. The large grain size increases hardenability together with carbon and all microalloying elements that dissolve in austenite. Due to the carbon supersaturated austenite, marten-

site forms easily, which accommodates the hydrogen introduced during welding, causing embrittlement in the hard microstructure. [7] A possible fracture occurs in a cold state when the structure is fully cooled and is therefore called cold cracking. Additionally, the mechanical strength of the cold-worked steel plate is significantly reduced due to recrystallisation [10]. The coarse-grained region is therefore, in many cases, highly critical and the temperature effect should be controlled to minimise the amount of grain growth and the width of the coarse-grained region in the heat-affected zone. The second region in the microstructure is less critical and more desired. The fine-grained austenite decomposes to small ferritic grains during cooling and retains 20-40μm grain size [7]. Due to the short diffusion time, the resulting microstructure is not homogeneous [10]. This structure has better toughness properties than the large-grained zone.

Further away from the regions transforming fully to austenite is a partially austenitic region, where the carbon concentration and its solubility in austenite are higher at lower temperatures. Thus, in these regions the hardenability is higher. With overly rapid cooling, the austenite grains transform partially to martensite and the rest of the austenite is retained at lower temperatures. The local martensitic grains are defined as local brittle zones surrounded by softer tempered ferritic grains. At even further regions from the fusion boundary, ferrite does not transform to austenite. However, ferrite grains are tempered, which may cause carbon partitioning and cementite formation. The possible cementite precipitates may act as local brittle zones. [7] Furthermore, in a multi-run deposit, the fusion zone is partially replaced by the new HAZ of a subsequent weld bead, and the columnar grains obtain a new reheated microstructure [14]. Since the reheating refines the coarse-grained HAZ, it should improve the mechanical properties of the weld [10].

2.3.2 Irradiation and Thermal Ageing on Reactor Pressure Vessel Weld Metal

The normal operating environment for an RPV is severe with elevated temperature, high pressure, and neutron irradiation in the core region. As described earlier, the base material and the weld metal are designed for high performance over a long lifetime, and the mechanical properties must meet very high demands. There are two main criticality factors, which affect the mechanical and physical properties of the material during operation, i.e., the neutron irradiation and thermal ageing induced embrittlement.

Thermal ageing has been shown to be dependent on the chemical composition and thermo-mechanical processing of the base material, in addition to the ageing time and temperature. For example, materials that do not receive a post-weld heat treatment have shown significant increase in the ductile-to-brittle transition temperature (DBTT), whereas the metals after the post-weld heat treatment show milder shifts in DBTT towards higher temperatures. This increase means lower resistance to brittle fracture. Therefore, know-

ing the behaviour and DBTT of the RPV materials is essential. An increase in the tensile strength and a decrease in the elongation have also been observed. The thermal ageing embrittlement stabilises after a certain time at an elevated temperature, which is seen for example as unchanged mechanical properties in prolonged ageing at higher temperatures. [21, 22] Some of the most important processes that lead to embrittlement in the RPV weld metal during service at elevated temperatures are phosphorus segregation to grain boundaries, resulting in intergranular fracture, and impurity and alloying element migration to dislocations in the same manner as in strain ageing [23]. The susceptibility to phosphorus embrittlement is relatively high in the coarse-grained HAZ compared to the fine-grained HAZ [21]. Furthermore, in the weld metal the alloying elements molybdenum and manganese suppress the solubility of phosphorus in α-ferrite and therefore may have an impact on the segregation at grain boundaries [24]. In the latest studies, atom probe tomography (APT) analyses have confirmed the presence of clusters with elements such as phosphorus, nickel, manganese, molybdenum, and copper at the grain boundaries, which cause hardening and thus promote embrittlement [25, 26].

The neutron irradiation is known to have additional types of effects on the RPV steel: lattice damages and dislocation clusters, clusters of specific elements such as copper, nickel and manganese, and impurity segregations, especially phosphorus. The first two cause an increase in the yield strength due to reducing dislocation mobility. [27] The neutron irradiation induces vacancies which further promote the formation of copper-rich clusters and precipitates which cause hardening [28]. As mentioned with the thermal ageing effects, phosphorus increases the DBTT but does not affect the yield strength, although the phosphorus content may have an impact on the fracture mode [29]. The general view is that neutron irradiation does not produce new additional micro-crack initiation sites compared to the initial material state because the radiation defects are so small that their effect on fracture initiation is considered to be negligible. There are, however, indirect mechanisms how the radiation affects the cleavage crack initiation. The radiation defects can decrease the strength of the primary initiators, the radiation defects may increase the driving force for micro-crack initiation, or the probability of dislocation pile-ups near the micro-crack initiators can be increased [30].

The changes in the RPV properties due to irradiation are monitored using surveillance programs, where specimens are subjected to higher dose rates than the pressure vessel, i.e., closer to the core. These specimens are then tested with regular intervals and the data is used to assess the properties of the pressure vessel. As the time to reach a specific dose is shorter than that for the RPV, the possible effect of thermal embrittlement is smaller.

3 BRITTLE FRACTURE MECHANISMS

In steels, an overload fracture can be divided into two modes, ductile or brittle. The brittle failure can additionally be either transgranular cleavage fracture or intergranular fracture. The division between a ductile and a brittle failure is made based on the amount of material's resistance to plastic deformation [31]. Ductile metals experience significant plastic deformation with high energy absorption prior to failure. Brittle metals, on the other hand, show none or very little plastic deformation with low energy absorption. The fracture mode is dependent on the surrounding conditions and, virtually, in all cases of failure, external stress is involved. Generally, ductility in steels is a function of temperature, strain rate, and stress state. A fracture begins with a crack initiation and continues by crack propagation, which furthermore determines the fracture mechanism. In a ductile fracture, the crack propagation is relatively slow and extended by plastic deformation and detention to cracking, and further the crack propagation is arrested. However, the brittle fracture, especially the transgranular cleavage fracture, can be extremely rapid and experiences no resistance to deformation. [31] Once a crack has initiated, it propagates spontaneously without an increase in loading. Due to its spontaneous nature, the cleavage fracture occurs catastrophically and is essentially an undesired fracture mode. Therefore, the brittle fracture of the RPV materials must be hindered for all possible circumstances. Cleavage fracture initiation occurs below the theoretical strength.

There are three modes for crack surface displacement that occurs during the material failure, as two new surfaces are produced. Mode I is the most common and called the opening mode, as it occurs under a tensile stress. Mode II occurs under an in-plane shear stress and is called the sliding mode. Mode III is the tearing mode, as it occurs under an out-of-plane shear stress. These modes are presented in Figure 3.1. Mode I is mostly used in the brittle fracture characterisation and is the most common primary fracture mode. This chapter introduces the laws of brittle fracture and its characterisation methods.

3.1 Fracture of Steels

The reactor pressure vessel in question consists of plates and forgings made of a low-alloy steel with a bainitic microstructure. Bainite consists of ferrite and cementite phases. The weld metal, on the other hand, has a ferritic microstructure. Ferrite has a body-centred cubic crystal structure up to 48 slip systems, along which it has the ability to

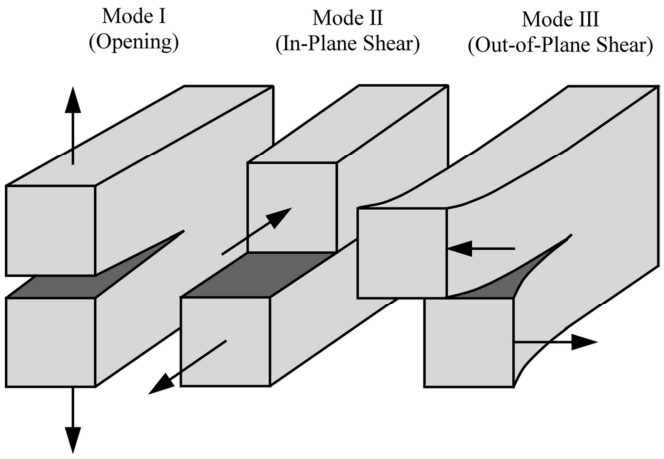

Figure 3.1. *The three failure modes presented schematically [32, p.43 Fig.2.14]*

experience plastic deformation. The dislocation mobility is relatively easy along the slip planes at the room temperature and above, and ferrite thus shows high ductility. [33] Under tensile loading, a tough material absorbs energy and the cross-section deforms until the load becomes high enough to reduce the cross-section to so much that the specimen fails. If a ductile specimen contains one or more micro-cracks, the cross-section of the sample is effectively reduced when the tensile stress is increased. However, below room temperature, the deformation is restrained and ferrite becomes brittle. The energy absorption is significantly lower and the failure occurs suddenly at much lower stresses than the theoretical tensile strength of the material. Furthermore, the failure mechanisms of crystalline materials are strongly related to surrounding conditions, especially the temperature. In certain conditions, where normally ductile metals become brittle and fracture occurs without preceding plastic deformation and necking, fracture occurs along grain boundaries or certain crystal planes [16]. The latter is called a cleavage fracture. Metals with a body-centred cubic crystal structure, such as low-alloy steels, are the most prone to cleavage fracture at low temperatures. In Subsection 3.1.2, the temperature effect is described in more details.

At room temperature, the basic ferritic crystal structure contains equiaxed grains and thus acts ductile by providing high dislocation mobility and multiplication [33]. In practice, the heterogeneous microstructure of e.g. RPV materials contain local structures that have a more complex crystal structure. These may lack sufficient dislocation systems to provide plastic deformation, and therefore they can be brittle under external loading. Due to these local sites in the microstructure, such materials are the weakest links in the system and, if there is a sufficient amount of them or they are accumulated in a small area, the whole metal may act in a brittle manner under certain circumstances [16]. For example, large carbide clusters are undesirable in ferritic steels. Cleavage fracture in known as a failure mechanism with little preceding plastic deformation, involving certain crystallographic planes of high atom density [7]. The $\{100\}$ planes are introduced as the easiest slip

planes for α-iron although they are not the most densely packed crystallographic planes. In contrast, γ-iron or austenite has a close-packed face-centred cubic crystal structure and therefore is not prone to cleavage fracture [28]. The cleavage crack in ferritic steels propagates along the $\{100\}_\alpha$ planes nearly at the speed of sound [16]. However, theoretically the most favoured slip planes for cleavage fracture in bcc metals are $\{100\}$, $\{110\}$ and $\{111\}$ planes of which the surface energy is the lowest for the $\{110\}$ and second lowest for the $\{100\}$ planes [34]. The fracture is not only based on the energy required to create new surfaces but it also involves dislocation emission and twinning. These are much more complex processes for the $\{110\}$ and $\{111\}$ planes which gives reason for the $\{100\}$ plane to be the most brittle planes [35].

In polycrystalline metals, the fracture is more complex and involves several fracture mechanisms and range of grain orientations [36]. It has been shown that the brittleness is greatly increased when the cleavage planes of ferrite are aligned along a macroscopic plane and easy crack propagation with very little resistance. Such sites can be found in the coarse-grained heat-affected zones of a weld joint with similarly oriented grains, the effect being called texture embrittlement [7].

Since the brittle fracture occurs abruptly, it is important to know when such a failure can occur, but also the reasons for its initiation. Generally, sufficient factors for the cleavage fracture initiation are low temperature, sharp edges and cuts at the surface, and high load and loading speed [16]. The cleavage crack nucleation usually occurs at grain boundary triple points, twins, or secondary particles such as inclusions or carbides. These factors have a significant effect on the bcc iron due to the Peierls-Nabarro force. The Peierls-Nabarro stress is described as the stress required for the dislocation movement and plastic deformation in an otherwise defect-free lattice, and it differs between the crystal types and materials. The Peierls force is fundamentally due to the binding forces between the atoms. The effect of Peierls stress on dislocation mobility was later modified by Nabarro, and therefore it is usually called the Peierls-Nabarro stress. Metals with a bcc structure have much higher temperature-sensitivity than the fcc metals, which do not show such a change from ductile to brittle mode relative to the temperature, i.e., transition behaviour. In ferritic steels, the Peierls-Nabarro stress increases readily with decreasing temperature. This is shown as a steep rise in the yield strength at low temperatures, promoting premature fracture in the structure [28]. The reason for this may be that with rapid deformation the dislocations pile up and nucleate cracks, when the interstitial atoms such as carbon cause the emergence of a sharp yield point. The alloy steels include also secondary phases, where the crack nucleation is relatively easy at the grain boundary phases or phase structures with sharp edges. In ferritic steels, the crack initiation is typically due to a second phase particle [32]. The secondary phase structures may cause initiation of micro-cracks, which further grow into a cleavage or intergranular fracture. Furthermore, the grain size affects the transition behaviour since with smaller grain sizes a smaller number of dislocations pile up or coalesce at the grain boundaries. Therefore, the local stress concentration at the grain boundary is smaller and the chance for crack nucleation is reduced. [7]

3.1.1 Griffith Crack Theory

The theorem of brittle fracture was first introduced by Griffith in 1920 [37]. It describes the relationship between stress and crack initiation when the crack growth becomes energetically favourable. The equation characterises a decrease in the potential energy within a stressed plate and an increase in the surface energy when new surfaces are produced by separation at a crack to retain the energy balance within the plate. Griffith described the potential energy change and the surface energy term using the theorem by Inglis [38] which included an infinitely large plate with an elliptical crack. The stress concentration at the crack tip could be computed with a decrease in the potential energy by the term $(\pi {\sigma_a}^2 c^2 t)/E$, and therefore the change in the potential energy at the crack initiation is given as

$$U - U_0 = -\frac{\pi {\sigma_a}^2 c^2 t}{E} + 4ct\gamma_s \tag{3.1}$$

where U is the potential energy of the bulk with a crack, U_0 is the potential energy of the bulk without a crack, σ_a is the applied stress, c is half of a crack length, t is thickness, E is the elastic modulus, and γ_s is the specific surface energy [28].

The first term on the right side of the equation is negative, since it represents the released strain energy, U_e, when sufficient loading, σ, is applied for a crack to propagate. The crack opening creates two new surfaces, each with a surface energy $U_s = 2c\gamma_s$, which is added as the second term in the equation. The surface energy has the unit of energy per unit area. According to the theorem of Griffith, if an increase in the surface energy is less than a decrease in the strain energy, the crack will propagate [7]. Therefore, the equation is presented for the boundary state equilibrium at which the crack length changes and the energy difference is zero, i.e.,

$$\frac{dU}{dc} = \frac{d(U_e + U_s)}{dc} = 0 \tag{3.2}$$

The elastic energy can further be expressed as a release rate G, i.e., the rate of energy change with crack extension, or as fracture stress σ_f. Since the total energy curve as a function of crack length is a negative parabola, the highest point corresponds to the critical crack length. Greater lengths than that mean a lowered, favourable energy state and hence fast fracture. This also defines the stress where energy just above the threshold is released, less energy is required for new surface formation, and the fracture propagates, which is further given as

$$\sigma_f = \sqrt{\frac{2E\gamma_s}{\pi c}} \tag{3.3}$$

The crack length, c, is inversely proportional to the stress, which means that as the crack length grows, less external stress is required for the crack propagation. However, in metallic materials, plastic deformation at the crack tip should be taken into account at the crack initiation and propagation front which complicates crack propagation and increases the required stress. Therefore, a term for plastic work energy, or fracture energy γ_p, is

added in the equation, and the required stress according to the Griffith criterion is then given as

$$\sigma_f = \sqrt{\frac{2E\gamma_s - \gamma_p}{\pi c}} \tag{3.4}$$

It has been shown for ductile alloys [39] that the energy of plastic deformation is several orders of magnitude greater than the surface energy of the new interfaces. Since the maximum stress at the crack tip is much higher than the yield stress, the fracture occurs with the assistance of very small particles in the steel. Cleavage fracture initiates as a micro-crack and propagates into the matrix. The coalescence of micro-cracks in adjacent grains produces a macro-crack and further a failure.

The stress intensity factor at the crack tip is characterised by a parameter K. A critical value K_C corresponds to the situation when the propagation initiates and is given by the fracture stress and crack length, which can further be expressed under plane stress with the critical rate of energy release, G_C, as

$$K_C = \sigma_f \sqrt{\pi c} = \sqrt{EG_C} \tag{3.5}$$

In plane stress conditions, the fracture is assumed to occur in Mode I, and the fracture toughness is often expressed as K_{IC}. Hence, the critical value for the release rate of the strain energy in planar conditions is $G_{IC} = \gamma_p$ [7]. The energy release rate is analogous to the crack propagation rate, a higher value corresponding to easier crack propagation and therefore to brittle failure. Hence, G is also described as the crack driving force. Furthermore, the critical value of stress intensity is written with the release rate as

$$K_{IC} = \sqrt{\frac{EG_{IC}}{\pi(1-\nu^2)}} \tag{3.6}$$

where the ν is the Poisson's ratio. The K_{IC} term characterises the fracture toughness, as brittle fracture occurs when K_I reaches the critical value.

3.1.2 Ductile-to-Brittle Transition

Ferrite phase has a body-centred cubic crystal structure, which has a characteristic ability to change the mechanical properties of the material with temperature. Going from ductile plastic deformation to brittle fracture behaviour as a function of decreasing temperature is called the ductile-to-brittle transition [33]. The ductile-to-brittle transition temperature is therefore defined as the critical temperature where the failure mode changes. Above the transition temperature, the material acts in a ductile manner, and below the transition temperature the brittle fracture dominates but ductile fracture is also involved. On the other hand, metals such as austenitic stainless steels with a face-centred cubic crystal structure do not show such a clear transition in the mechanical properties and can be ductile down to cryogenic temperatures [7]. The ductile-to-brittle transition is characterised by a

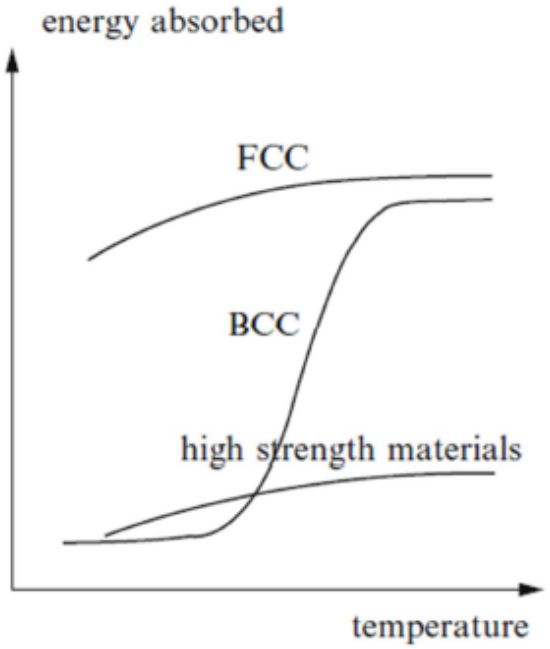

Figure 3.2. *Ductile-to-brittle transition curve for bcc, fcc, and high-strength materials [40].*

transition curve seen in Figure 3.2 for different types of metals. The transition curve for bcc metals demonstrates the upper and lower shelves, and between them is the steep decrease of energy describing the transition in the fracture behaviour.

Typically, the testing method for the determination of the transition temperature is the Charpy V-notch (CVN) impact toughness test, which is a dynamic test. In CVN testing, the impact toughness is measured quantitatively by the energy absorption. In case of the brittle fracture, the energy absorption is about half of that of the maximum ductile fracture. However, it has been proven [41] that the yield stress and energy absorption results are dependent on the testing method and the size and the shape of the notch, since the transition temperatures and the impact toughness results vary depending on the testing conditions. Therefore, the transition temperature is not a distinct material property, and the testing methods are standardised to obtain comparable results [16]. A more detailed description of the transition curve is presented in Section 3.2.1. The transition temperature is typically determined at the energies of 27/28 J, 41/42 J, and 68 J, depending on the conversion from the original unit to a metric equivalent. The reference points have been chosen to easier comparison of similar materials in different conditions. The value of 28 J indicates the part where the transition curve increases from the lower shelf and where brittle fracture mode dominates. The value of 41 J is more in the transition region of the DBTT curve, and 68 J is used more in the estimation of the ductile fracture regime. In this project, the reference transition temperature at 41 J is used.

The ductile fracture involves plastic deformation, which occurs by dislocation movement. The transition from ductile to brittle fracture is explained by the inability of screw dislocations to cross slip, i.e., by restricted dislocation movement. Hence, the dislocations

cannot overcome obstacles by cross slip and there is no dislocation multiplication which is required for continuous plastic deformation. The immobility of the screw dislocations is related to low-temperature segregation of impurity atoms at dislocation cores, forming asymmetries in dislocation stress fields due to solute atoms. [33] These have been described by the so called Cottrell atmospheres [42], where interstitial and substitutional atoms concentrate around screw dislocations and pin them with internal stresses in the lattice. At a low applied force, the solute atoms migrate with the dislocation and form a cloud which gives the material a sharp upper yield point. However, with a sufficiently high stress the dislocation can be separated from the solute atoms, and it becomes highly mobile, giving the material a lower yield point. If the specimen is unloaded and given time before reloading, the solute atoms migrate around the dislocations again forming atmospheres, thus making the yield point to appear. The phenomenon corresponds to the case of strain ageing. In addition to the inability of the screw dislocations to cross slip, there are other microstructural features affecting the transition. For example, the fine grain size decreases the DBTT, while the second-phase particles may cause premature cleavage fracture initiation [33]. Furthermore, as mentioned in Subsection 2.3.2, neutron irradiation and thermal ageing increase the transition temperature by shifting the curve towards higher temperatures and lowers the upper shelf ductile fracture toughness.

Furthermore, the alloy content and heat treatment of the steel can have a significant impact on the material's tendency to cleavage fracture. The effects are manifested in several ways, and with multiple impacts they may be difficult to distinguish. Pure ferrite acts ductile even at near cryogenic temperatures, but with increasing carbon and nitrogen content, the ductile-to-brittle transition temperature increases up to room temperature and above [7]. Already very small additions of carbon increase the transition temperature with tens of degrees, and for example 0.03 wt%C normalised steel without manganese additions gives a transition temperature of +80 °C [41]. This means that the steel is highly brittle already at room temperature, unless the carbon content is suppressed down to less than 0.01 wt%. However, with rapid cooling the transition temperature can be decreased down to -50 °C, since the formation of Cottrell atmospheres is prevented [16]. The effect of carbon content is mainly due to the formation of brittle second phases and their effect on the yield stress. Therefore, alloying that prevents the formation of carbides promotes the low-temperature transition. The effect of nitrogen is similar to that of carbon when it comes to the formation of dislocation atmospheres and dislocation pinning. The effect increases the yield point and therefore also the transition temperature, which is further promoted by strain ageing.

The transition temperature of steels is highly sensitive also to oxygen, which in small concentrations increases the DBTT. This, however, promotes fractures along the grain boundaries instead of cleavage fracture. In the alloy steels, oxygen appears in stable oxides and is not a hazard in moderate concentrations in the commercial steels. Additional elements such as manganese and silicon combine with oxygen and therefore have a decreasing effect on the transition temperature. Manganese strongly decreases the transition temperature by improving the fracture toughness more than the yield strength.

Manganese has a beneficial effect on the transition temperature up to 1.8 wt% concentrations [16], and it also combines with sulphur resulting in inclusions (MnS) that are typically harmless as single-phase particles [43]. Additionally, manganese combines with nitrogen, preventing nitrogen atmospheres around dislocations and therefore reducing ageing problems. Nickel has a similar effect as manganese up to 3 wt% concentrations. Aluminium additions lower the tendency to strain ageing and further to fracture by cleavage or along grain boundaries as it combines with both nitrogen and oxygen, preventing their detrimental effects [16]. Phosphorus is known for its undesirable effect as promoting brittle fracture, and during high-temperature thermal ageing, phosphorus precipitates at the grain boundaries and promotes the intergranular fracture. During steel processing, as much of phosphorus is removed as possible, since it appears as an impurity element in the metal.

As a conclusion, the alloy elements promoting strain ageing have the biggest impact on the increase of the transition temperature and the cleavage fracture. The increase in the transition temperature due to the strain ageing can be minimised by sufficient heat treatments such as annealing or normalising, yet avoiding excessive grain growth. In the welds, severe heating causes coarse grains, as described in Subsection 2.3.1, which may promote a local increase in the transition temperature compared to the base material. However, in the weld the solidification shrinkage may cause plastic deformation that promotes strain ageing and further an increase in the transition temperature [10]. The cleavage fracture in RPVs is always detrimental since it propagates rapidly through the construction, and the thermal ageing and irradiation affects the mechanical properties of the weld metal.

3.1.3 Brittle Fracture Initiation and Microstructure

So far, the characteristics of the brittle fracture mechanisms and the bcc metal failure modes have been introduced. In ferritic steels, the carbides, secondary particles such as precipitates, and other discontinuities make the metal microscopically inhomogeneous and act as cleavage micro-crack nucleation sites. The random location of the nucleation sites ahead the crack front is demonstrated by the variation of the fracture toughness, which is characterised by statistical methods. The test materials are typically assumed macroscopically homogeneous. However, a multipass weld includes heat-affected zones and reheated regions and the statistical methods are not applicable due to the indifferences between the base material and the weld microstructure. When comparing the results within a good quality weld, the microstructure can be assumed homogeneous. Furthermore, the local properties are in the following sections evaluated separately from the bulk.

The brittle fracture is initiated when K_I at the crack tip reaches K_{IC}. This occurs especially in the lower shelf and partly in the transition stage of the DBTT curve. The assumption of homogeneous material has enabled the description of an average stress

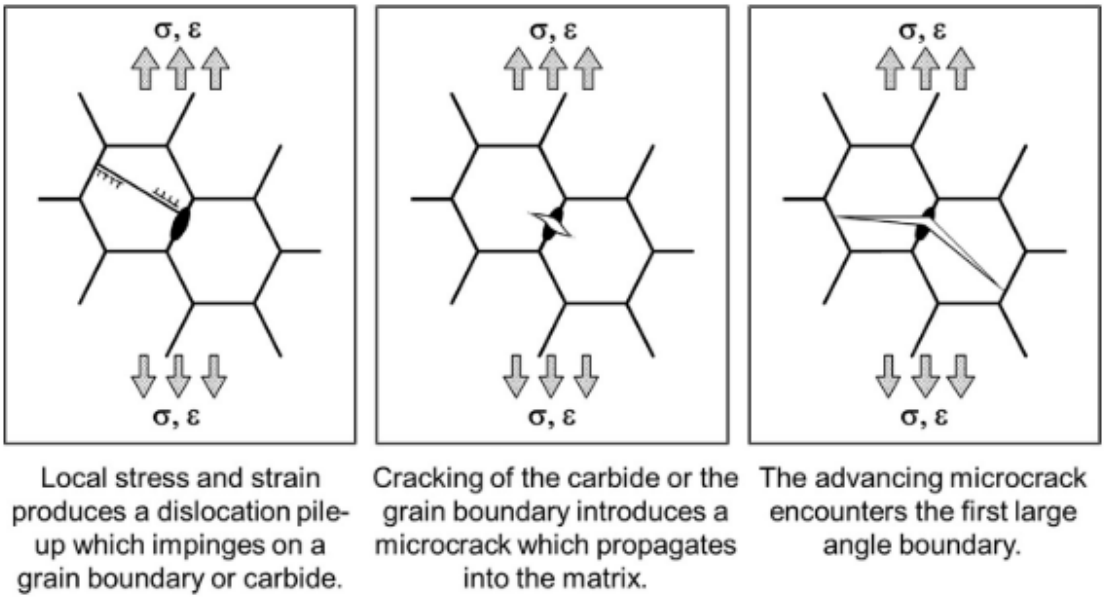

Figure 3.3. *Schematic presentation of a typical cleavage fracture initiation process [44, p.116 Fig.4.2].*

and strain analysis of a macroscopic plate sample, where the brittle fracture toughness is characterised by K_{IC}. [7] However, a true material contains grain boundaries, inclusions, segregations, and other discontinuities which distract the crack propagation. Therefore, microscopically the local fracture resistance of the material must be determined for the brittle cleavage fracture initiation. In the evaluation of the cleavage fracture, the probability of crack initiation is statistically analysed [44] . Primarily, the local failure is caused by stresses and strains at precipitates, inclusions, grain boundaries, etc., from which the crack develops to a dynamically propagating cleavage fracture. Typically, the stresses cause a dislocation pile-up locally at a grain boundary, where a micro-crack initiates and propagates into the matrix and further through the grain. The three-step-process is schematically described in Figure 3.3. At the lower shelf temperatures, the crack initiation is easy and the fracture toughness is controlled by the crack propagation. At the transition region and at higher temperatures, the fracture toughness is controlled by the initiation rather than the propagation, as the stress distribution becomes more moderate. [44]

A brittle cleavage fracture has always a primary initiation site, which continues with the characteristic river pattern seen in Figure 3.4. The river patterns are often followed in fractography to find the initial fracture site. The cleavage fracture initiates near the maximum stress location and propagates along the easiest crystal planes in all possible directions. The crack path kinks from one cleavage plane to another so that the fracture propagates easily forming a network of the crack path. However, due to the kinks some planes do not intersect, causing the linkage between the planes to fail by shear fracture. Larger linkages may even fail by ductile fracture. [44] The shear or ductile fracture induced by intersecting cleavage planes do not indicate the primary fracture mode and they are important to be

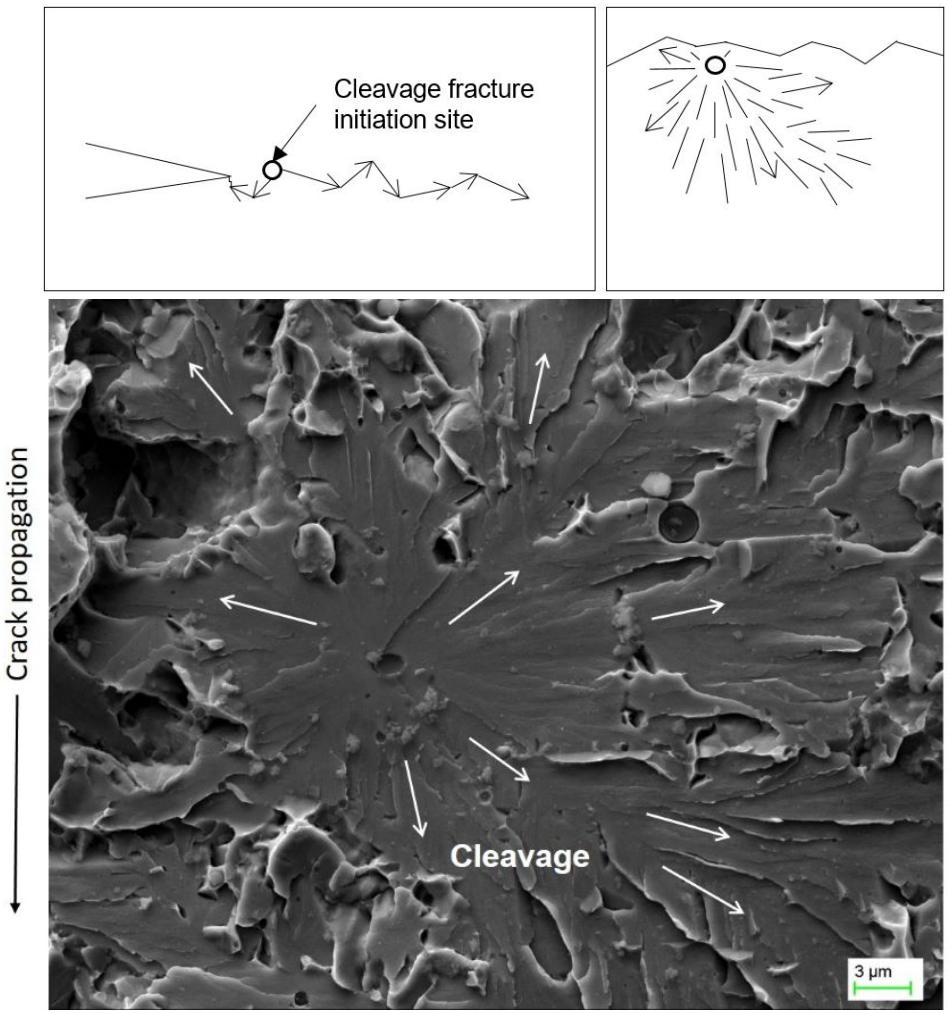

Figure 3.4. *Cleavage fracture initiation and propagation.*

recognised in the fractography.

A sharp micro-crack as a local discontinuity is always required ahead of the macroscopic crack, and the stress concentration should be sufficient to break the atomic bonds at the weakest link of the microstructure. The weakest link theory suggests that at least one initiation site is required for the failure to occur [45]. However, the general statistical model or the cumulative probability of initiator distribution is a complex function, but simplified if a sharp crack is assumed. Usually in the RPV steels, the initiation begins at a brittle local phase or some other second-phase particle [2]. If a stress is applied to a component and a particle or grain boundary fails but no cleavage fracture initiates, the micro-crack will blunt and form a void. The void is not able to initiate a fracture, the initiator distribution is not affected and the probability of fracture initiation becomes conditional. If the initiated cleavage crack at the particle or grain boundary propagates, the component fails. On the other hand, if the cleavage initiation is unable to propagate, the crack is arrested and does not lead to a failure. [44]

The brittle fracture initiation is the most critical process regarding the mechanical performance of a material, and the fracture probability is determined by using the weakest link

statistics. There are theories about the fracture toughness of metallic materials, and an important statistical approach was introduced by Weibull [46, 47, 48]. The Weibull analysis involves an idea of a probability of a flaw of certain size and orientation that causes a failure when a sufficient stress is applied. In a simple model, in case of a pre-existing crack, the crack that is largest and perpendicular to the tensile loading direction is the most probable crack to fail first. The phenomenon is based on the limiting factor assumption in the component of certain volume, where a defect causes a failure at the lowest applied stress. Therefore, according to the Weibull theory, the probability of failure can be expressed as a function of component volume given by

$$F = \int f(\sigma) dV \tag{3.7}$$

Expressing the failure by the survival probability, $S(V)$, i.e., the probability of no cleavage initiation, the probability function of failure, F, is then given by

$$F = 1 - \exp\Big\{ - V\Big(\frac{\sigma_a - \sigma_u}{\sigma_0}\Big)^m \Big\} \tag{3.8}$$

where the exponent function describes the survival probability, V is the volume of the component, σ_a is the applied stress and σ_u is the stress below which there is a zero probability of failure. Furthermore, σ_0 is the characteristic strength where the probability of failure is 63.2%, and m is the Weibull modulus that characterises the strength variability of the material. The Weibull modulus describes the homogeneity of the material and as m approaches ∞, the probability of failure becomes zero when $\sigma_a < \sigma_0$. In contrast, when m approaches zero, the probability approaches 1 and the failure occurs equally at any stress level. [28] As described in Equation 3.8, the fracture strength varies with the component volume as does the probability of survival.

From the Weibull theory of probabilistic approach on the brittle fracture, the Master Curve (MC) method has been further developed and standardised in ASTM E1921 [49]. It is applicable especially for bcc ferritic structural steels with the characteristic transition temperature. The fracture toughness is described by scatter, specimen size, and temperature in the transition region as well as on the lower shelf. The statistical analyses often require a large number of specimens and a large population of results to be reliable. With the Master Curve method, the material's brittle fracture toughness can be determined with a small specimen size and a smaller population. The method involves a theoretical determination of the scatter of fracture toughness, the specimen size effect, and an empirically found temperature dependence [44]. Thus, the brittle fracture toughness can be characterised with the transition temperature T_0. The Master Curve is plotted as a function of cumulative fracture toughness K_0 for the transition temperature $T - T_0$. The principle is described in Figure 3.5. The temperature T_0 corresponds to a 25 mm thick specimen with mean fracture toughness of 100 MPa$\sqrt{\text{m}}$, and the dependence of K_0 is based on the best fit to a number of large data sets. The theoretical part of the cleavage fracture

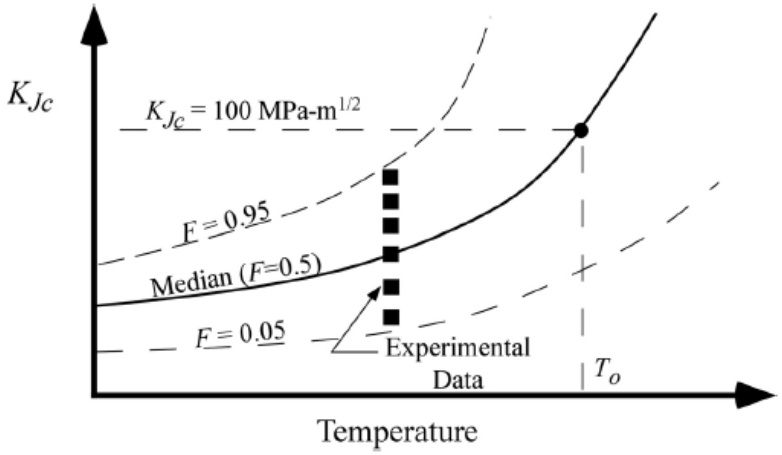

Figure 3.5. *Principle of the Master Curve method with indication of the transition temperature T_0 [32, p.340 Fig.7.39].*

model can be presented as follows:

$$P_f = 1 - \exp\Big\{ - \frac{B}{B_0} \times \Big(\frac{K_I - K_{min}}{K_0 - K_{min}}\Big)^4 \Big\} \tag{3.9}$$

where B is the crack front length, i.e., the specimen thickness, B_0 is the normalising thickness of 25 mm, K_I is the stress intensity factor, K_{min} the lower limiting fracture toughness, and K_0 corresponds to the cumulative failure probability of 63.2% (compare to the Weibull theory and the σ_0 in Equation 3.8) [50]. With the empirically obtained temperature dependence, the fracture toughness data covers the temperature range from -109°C to +51°C, and the temperature dependence of K_0 is exponential due to the assumption of cleavage fracture being thermally activated.

So far, only the fully brittle fracture initiation has been discussed. In the transition region and in the upper shelf of the ductile-to-brittle transition curve, the fracture involves plastic deformation by an elastic-plastic instability prior to the cleavage crack [44]. This is characterised by a stress intensity factor K_{Jc}, which is derived from the J-integral at the initiation site of a cleavage fracture, J_c. The J-integral is a mathematical expression that characterises the stress-strain field around the crack front under Mode I loading, i.e., plastic yielding during crack propagation. Previously in the section of the Griffith crack theory and equation 3.5, the energy release rate during the brittle crack initiation was introduced. The J_{IC}-integral equals to G_{IC} in a quasi-static loading at an elastic or elastic-plastic material and is therefore also connected to the crack propagation rate. The determination of the stress intensity at the onset of cleavage fracture in the upper shelf is given as

$$K_{Jc} = \sqrt{J_c \frac{E}{1 - \nu^2}} \tag{3.10}$$

where E is the Young's modulus of the material and ν is the Poisson's ratio. However, in this thesis the mechanical testing concentrates on the brittle fracture and on the lower transition region rather than the ductile fracture.

3.2 Characterisation of Brittle Fracture

The fracture of a material can be characterised using different methods qualitatively and quantitatively. In quantitative methods, the absorbed energy during fracture is measured by the Charpy-V impact toughness test. The energy absorption describes the fracture mode, as discussed in more detail in Subsection 3.1. In addition to the CVN testing, compact tension (C(T)) specimens, also of miniature size, can be used for determination of the fracture toughness and K_{IC}, uisng tests where the specimens are pin-loaded in tension [49]. Generally, the amount of plastic deformation can be determined by yielding and observed necking of the metal. Furthermore, the fracture surface appearance is evaluated by fractography, which is an effective tool in determining if the fracture occurred on the lower or the upper shelf or in the transition region of the ductile-to-brittle transition curve. Typically, stereo- and electron microscopy are used in the visual evaluation of the fracture surface. In electron microscopy, smaller details that are characteristic to the different fractures are found in the imaging. The grain boundary and screw dislocation fractures cause a mosaic-type fracture surface, which is easy to distinguish from the other fracture types. Ductile fractures, on the other hand, leave a more silky or veined surface with possible secondary particles in the dimples. In the cleavage fracture areas there are so-called river patterns, which combine and grow in the directions of propagation, making it possible to track back the initiation sites [16]. In this section, the main material characterisation methods are introduced regarding brittle fracture initiation in a steel weld microstructure.

3.2.1 Charpy-V Impact Toughness Test

The ductile-to-brittle transition temperature behaviour is characterised by the Charpy V-notch impact toughness testing. The experimental conditions have been developed such that the material's capacity for plastic deformation is suppressed [28]. Therefore, the CVN impact toughness testing uses low test temperatures, multi-axial stress state, and high strain rate in the fracture testing. However, by reducing the strain rate, the transition occurs at lower temperatures but still at the same lower shelf energy. The Charpy V-notch specimen in the standardised CVN test has a V-shaped notch as a pre-existing defect to obtain the multi-axial stress state concentration to promote the cleavage fracture in the impact loading. For materials with little intrinsic ability for plastic deformation, the notch increases the local stress state to a higher level and restrains the little plastic deformation capacity of the material, resulting in a brittle fracture.

In the Charpy V-notch impact toughness test, the absorbed energy during fracture is measured at various testing temperatures so that, as described earlier, the fracture energy is analogous to the fracture mode. The energy absorption is determined by the height that the pendulum reaches after breaking the specimen [28]. The fracture energy in the

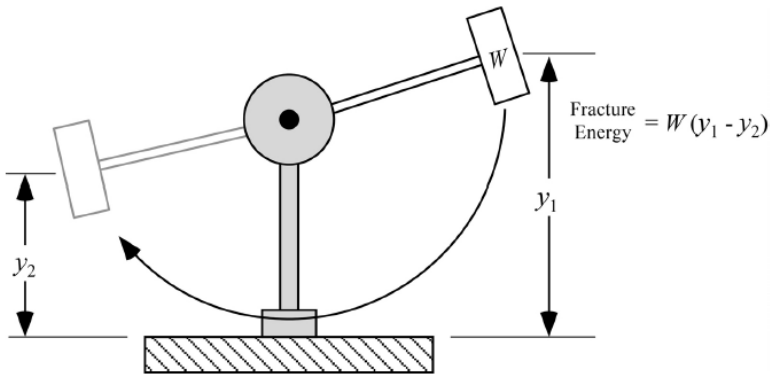

Figure 3.6. *Principle of the pendulum device used in the Charpy-V impact testing. The fracture energy is obtained from the weight of the cross-head and the height difference of the pendulum. [32, p.342 Fig.7.21].*

impact is given according to Figure 3.6 by

$$U_I = m_a g \Delta y = W(y_1 - y_2) \tag{3.11}$$

where m_a is the mass of the pendulum, g is the acceleration due to gravity, and Δy is the height change of the pendulum before and after an impact. The testing produces a transition curve characteristic to the method and material which as in Figure 3.2. The curve is presented with temperature on the x-axis and absorbed energy on the y-axis. The bcc steels show a characteristic transition curve with a sudden shift in energy absorption with temperature. At high temperatures, the curve has a plateau-shape and is called the upper shelf produced by ductile fracture. The absorbed energy decreases with temperature with a steep curve down to low-energy brittle fracture mode, appearing as the lower shelf. The steep curve between the upper and lower shelves describes the transition in the fracture behaviour. The data obtained from a CVN test can be fitted by a least squares function of a sigmoidal form, which is expressed by a hyperbolic tangent function (tanh) as

$$X = 0.5 X_{US} \left[1 + \tanh \frac{T - T_{50}}{C} \right] \tag{3.12}$$

where X_{US} is the upper shelf toughness in $X = f(T)$, T is temperature, and T_{50} and C are fitting parameters. The upper shelf value in the data analysis can be estimated based on the fully ductile fracture appearance, when the lower shelf value is assumed to be zero. The determination of the transition temperature has been used as a design tool for structural components to prevent the failure in the operating conditions. As mentioned earlier, the reference points on the transition curve are typically 28 J and 41 J, and the 28 J can be used for an estimation of the fracture toughness of the material.

In the CVN testing, the measured impact toughness consists always of both ductile and brittle fractures. Even the samples in the lower shelf of the transition curve show a small fraction of ductile fracture area in the edges of the specimen. Below the transition temperature in CVN testing, the fracture begins as ductile from the corner of the notch at high impact energy and multiaxial stress-state until a cleavage fracture initiates close to the

notch [16]. The fracture propagates as cleavage and possibly along the grain boundaries. The propagation of the brittle fracture is typically stopped by the ductile fracture at the end of the fracture surface. The propagation stopped by the higher-energy fracture mode is called crack arrest. When the CVN specimens are tested above the transition temperature, the dominating fracture mode is ductile, and the cleavage fracture may initiate only locally.

3.2.2 Hardness and Toughness

In the characterisation of the basic material properties the hardness is often measured. As a testing method, it is relatively simple and inexpensive, almost non-destructive, and comparable to strength and further to toughness. Hardness by definition is the material's resistance to scratching and abrasion, while toughness is resistance to fracture and propagation of a crack. Together they characterise the strength of the material, and they are inversely proportional to each other, i.e., hard material is usually not ductile and very tough materials have usually low hardness. Furthermore, they both are basic material properties that measure different characteristics of the material. However, since the toughness tests of the material are highly dependent on the testing conditions and the specimen size and shape, hardness testing is applied to measure the true mechanical property of the material. Furthermore, in fracture mechanics, no linear correlation between hardness and toughness has been proven, although there are methods to estimate the fracture toughness from the hardness indentations. Typically, toughness varies between the regions of the weld due to differences in microstructural and compositional features [51]. The toughness of the weld metal and coarse-grained HAZ are often poorer to that of the base material, whereas the fine-grained HAZ has toughness close to that of the base material. Since the toughness measurements across the weld requires larger testing capacity, the hardness is measured instead.

In Vickers hardness testing, a diamond indenter is pressed into the surface of the specimen leaving a mark to be measured, as seen in Figure 3.7. When the indenter of a pyramid with a square base is lifted up and removed from the specimen, the diagonals of the square mark are measured. The area of the indentation is proportional to the hardness of the specimen and the load of the indenter. With the diagonals and load expressed in Newtons, the Vickers hardness is calculated by dividing the test force (kgf) by the surface area of the indentation (mm^2). The unit of the Vickers hardness is described in HV with the load equivalent in kilograms. With the diagonals d_1 and d_2 of the indentation that are measured and the nominal diamond intenter angle $\alpha = 136°$, the equation for the practical hardness determination is further given by

$$HV = 0.1891 \times \frac{F}{d^2} \tag{3.13}$$

where F is the loading force and d is the mean length of the two diagonals. According

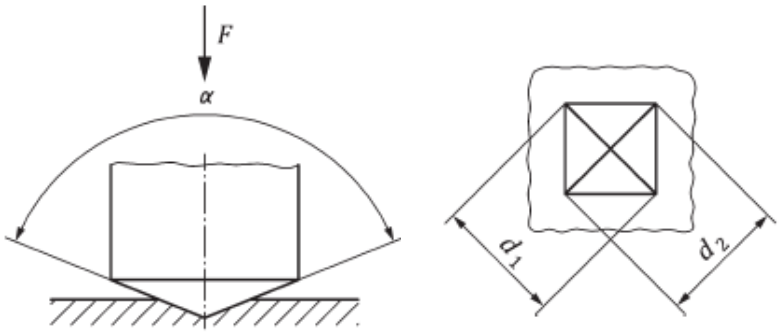

Figure 3.7. *Principle of the Vickers indentation with testing force and indenter geometry [52, Fig. 1]*

to the standard of Vickers hardness testing, the minimum distance between adjacent indentations must be at least three times the diagonal length and 2.5 times the diagonal length from the edge of the specimen [52].

There is a demonstrated correlation between hardness and strength, since they both describe the material's resistance to plastic deformation. A developed model expresses the HV data to correlate with the strength. Also strength and toughness are inversely proportional, and the fracture toughness and critical crack length can be calculated from the yield strength of the material. In an instrumented indentation method, the displacement of the surface can be measured relative to the load. As the indenter is removed from the surface of the specimen, the hardness and the elastic modulus can be determined. The elastic modulus quantifies the elastic recovery i.e., the material's resistance to elastic deformation. In the hardness testing, the indenter creates a triaxial stress state at the bottom, hence the extracted modulus is the plane strain modulus that can be expressed as $E/(1-\nu^2)$. [28, 53] Furthermore, such stress state appears in the multiaxial fracture toughness measurements, and the fracture stress in the plane strain conditions is relative to Equation 3.6 of the fracture toughness, i.e.,

$$\sigma_f = \sqrt{\frac{E\gamma_p}{\pi(1-\nu^2)c}} \tag{3.14}$$

Another method to evaluate the fracture toughness and hardness correlation is based on the crack opening [54]. The indentation in a hardness measurement may nucleate a crack at the corner of the indentation, which then correlates with fracture toughness. If the crack is at the surface of the specimen as a radial crack, i.e., a Palmqvist crack, it can have a linear relationship with the indentation load and the sum of the crack lengths starting from the Vickers indentation. Another possible crack to nucleate is the median crack that propagates from the bottom of the diamond indentation. For the median cracks it has been proposed that the linear relationship is between indentation size and indentation load.

4 MATERIALS AND EXPERIMENTAL METHODS

Mechanical and microstructural characterisation of Barsebäck 2 RPV involves several mechanical testing methods and microscopy evaluation techniques. The variety of methods is relevant in describing the properties of the weld metal from the nanoscale to the macroscale. The fracture toughness testing of a pressure vessel steel generally consists of determination of the T_0 temperature, impact toughness testing, tensile testing, and constraint testing. The main microstructural characterisation methods and the used mechanical testing methods are introduced and discussed in this Chapter. Since the project is part of commissioning the new laboratory infrastructure at VTT Centre for Nuclear Safety, the non-radioactive specimens are partly handled and treated as radioactive. Furthermore, some of the experiments are completed inside the hot cells where the equipment are installed.

4.1 Materials and Welding

The material under investigation is from a decommissioned nuclear power plant, Barsebäck Unit 2 boiling water reactor, which was in operation between 1977 and 2005 with the estimated effective full-power years of nearly 23 at 288°C. A cylinder shaped specimen is drilled from the head of the reactor pressure vessel with a special drilling tool called trepan. Four trepan specimens, numbered from 1 to 4, are cut originally from the RPV head so that the weld is in the middle. The specimens have nominal dimensions of ∅193 mm times the wall thickness of 70+3 mm. The investigations in this thesis are made on trepans 2 and 3, so that the Charpy V-notch specimens are from both of the trepans, and the microstructure characterisation is made on the cut-outs from the trepan 3. The cladding on the inner wall surface, made from stainless steel, is removed by milling to remove the radioactive surface contamination caused by the operation of the unit. The trepans are then sliced according to Figure 4.1 by a GF AgieCharmilles CUT 200 electric discharge machine (EDM) into different samples, which are further used in e.g. hardness and Charpy-V impact toughness testing. The use of EDM enables high-quality specimen preparation. The weld is used as effectively as possible to achieve as much results as possible, and also to have spare material for possible future investigations. The same test procedure will be implemented for the radioactive material removed from the belt line weld, i.e., the core region. Its active state limits the testing operations and smaller specimens are desired due to effective use of material and smaller dose per specimen.

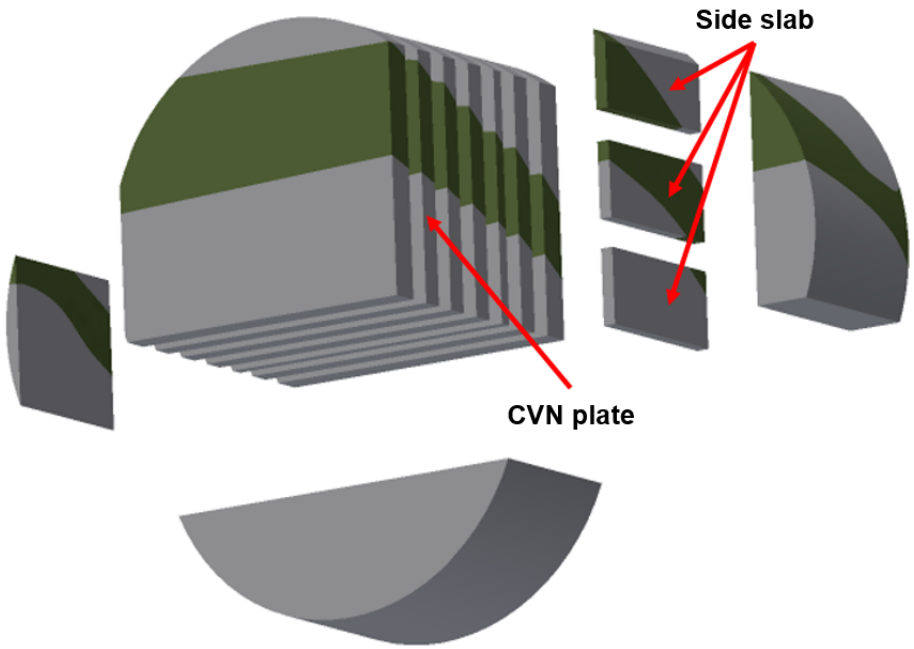

Figure 4.1. *All major cuts of trepan 3 are shown, including the plate where all the CVN specimens are cut and the side slab that is cut into three pieces. The weld is seen as darker colour in the middle.*

The reactor pressure vessel is built of a standard bainitic pressure vessel steels, which have a composition of low-alloyed steel with manganese and molybdenum additions. The head is a forging SA 508 Class 2 and the vessel is a plate metal SA 533 Grade B Class 1. The weld joint is made using two high-Ni weld filler materials, i.e., Phoenix-Union S3NiMo in the SAW and Oerlicon Tenacito 65 in the MMA weld. The base material plates have been quenched and tempered at 620°C, and the weld has been under post-weld heat treatment at 250°C for 16 hours. The RPV steel is designed to withstand severe deterioration under the service conditions for decades. The head of the RPV is subjected to thermal ageing, yet not to neutron irradiation, and therefore the investigated material is non-radioactive.

The experimental investigation concentrates on the weld joint of the RPV. The welding metal is high in nickel and manganese with a chemical composition given in Table 4.1. Additional chemical analyses have been determined by optical emission spectroscopy (OES) at Eurofins Expert Services Oy during the BRUTE project and are shown in the Appendix A. The first page gives the composition of the weld and the base material in English rewritten from the original certificate seen on the following pages. The analysis was done for eight locations of the weld through the wall thickness, and on three locations on the plate base material.

The RPV head weld is made by using submerged arc welding and, in this specific case also, manual metal arc welding methods. The weld is a multipass weld with several weld beads and characteristic microstructures of heat-affected zone and multiple reheated regions. The welding parameters have a great impact on the quality of the weld, grain size,

Table 4.1. *Chemical composition of the weld metal according to the material specification [55]. The second and third row show the composition of the two filler materials according to the OES analysis.*

	C	Mn	Si	Ni	Cr	Mo	S	P	Cu	Al	Co	Sn
Original	0.084	1.53	0.22	1.47	0.13	0.44	0.004	0.011	0.064	0.005	0.008	0.006
SAW	0.057	1.43	0.15	1.48	0.03	0.41	0.007	0.008	0.060	0.024	0.020	
MMA	0.037	1.38	0.25	1.22	0.03	0.37	0.007	0.007	0.004	0.002	0.018	

bead size, and heat-affected zone. Excessive heat input may cause severe thermal damage in the base material, and the welding speed determines e.g. the grain orientation. The welding parameters for this particular weld are obtained from the technical specification [4]. The SAW weld was completed with a current of 600 A, voltage of 30 V, and welding speed of 550 mm/min by a 4 mm filler metal. The component was pre-heated to 175°C, which was also the working temperature. The MMA weld filler wire-diameters were 4 and 6 mm, for which the used currents were 140-180 A and 260-310 A, respectively. However, for the manual weld no welding speed is documented.

4.2 Hardness

The Vickers hardness measurements are performed according to standard SFS-EN ISO 6507-1:2018 [52]. A Struers DuraScan-80 hardness measurement device is installed inside the hot cell in the laboratory where the equipment is used and operated from outside the cell remotely. The test machine is connected to a computer and on a program the testing can be automatised. The set-up and hardness matrix is programmed on the computer for each specimen. Additionally, the conditions inside the hot cell are controlled. The indentations are made on a 3 mm $\times$ 3 mm matrix over the full area of the plate sample, hence 200-300 data points per plate are obtained. During the testing, the computer evaluates every indentation automatically based on the contrast differences between the indentation and the polished surface. Lastly, the operator shall verify the correct measurements for each indentation. The hardness is measured with different loads, i.e., HV10, HV1, and HV0.3, and the typical sizes of the indentations are 0.3 mm, 0.1 mm and 0.05 mm, respectively. The larger indentations give more a general hardness value of the material, while the smaller indentations are more localised and give a better estimation of the hardness in a certain microstructure. Especially in a multipass weld, where there is a complex microstructure, it is important to know in which part of the weld microstructure the indentation is located.

The hardness is measured through the wall thickness along the weld using the loads of 10 kgf and 1 kgf. The hardness profile over the weld is evaluated. To compare the weld microstructure features, a load of 300 gf is used. The macrohardness of HV10 is measured to estimate the differences between the inner and outer side of the weld and to evaluate the effects of manufacturing or operation. The plate is cut from a trepan, which

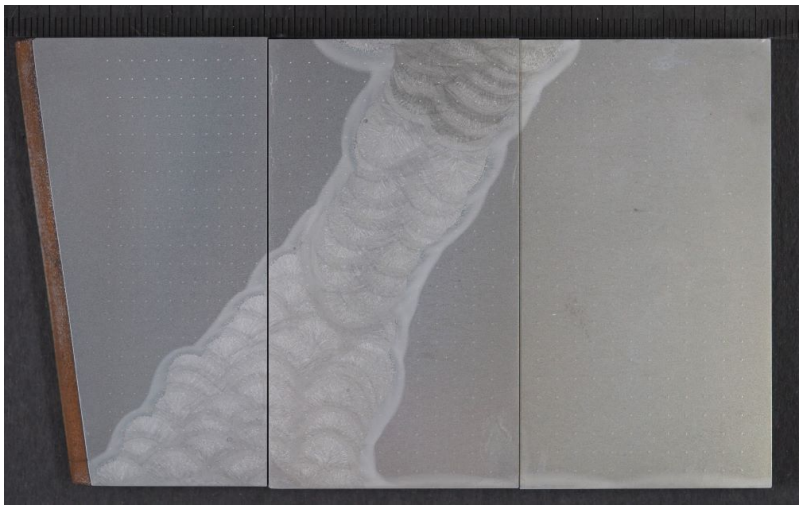

Figure 4.2. *The trepan 3 side slab showing the weld location after macrohardness measurements. The inner surface is at the bottom and the outer at the top of the image.*

is then divided into three parts using the EDM. The hardness matrices are then made for these plates. The weld runs through the plates diagonally, as seen in Figure 4.2. On one plate, the hardness of HV1 is measured in lines from the base material over the HAZ to the weld, which will additionally give a profile of hardness through the weld microstructure into the base material.

After the measurements, the plates are lightly ground and polished to remove the large indentation marks to prevent uneven etching. The samples are etched with 3% Nital solution (HNO_3 + ethanol) and washed in ethanol to correlate the weld features with the indentations. Reprography images are then taken for documentation and hardness results evaluation by an Olympus OM-D E-M1 Mark II camera with M.Zuiko 25mm F1:28 Pro objective. With the option of bracketing, the resolution is larger from the surface to the bottom of the indentations, as the camera takes several images on a small depth range.

The cross-section samples in microhardness evaluation are measured with test load of 300 gf on a small area at the brittle fracture area. This specific part of the weld is measured to obtain local data at a still finer level, i.e., 100 μm scale, about possible clusters, segregations, and phase structures. The sampled area is smaller and a hardness matrix with 100 data points per sample is used.

4.3 Light Optical Microscopy

A highly important microscopy technique in metallography is light optical microscopy (LOM) due to its relatively simple use and applicability to general characterisation of microstructural features by macro- and microimaging. Magnifications from 5x to 50x are typically utilised, and most phases and grain structures can be observed at magnifications of 100x. Therefore, optical microscopy is often the first tool used in the basic characterisation. [56] After the general evaluation, electron microscopy can be used for more detailed

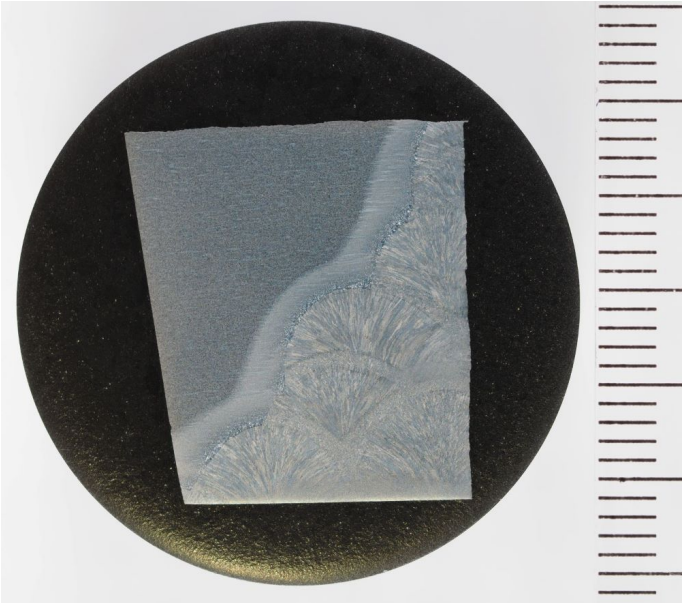

Figure 4.3. *A specimen for general metallographic evaluation of the investigated weld. The sample is a corner cut from trepan 3 next to the inner surface of the trepan. The scale on the right edge has a line spacing of 1 mm.*

evaluation of inclusions and precipitates. In microstructure evaluation and fractography, the sample preparation and etching are critically important to obtain reliable results.

The equipment used is Zeiss Axio Observer 7 inverted optical microscope and it is installed inside the laboratory's hot cell. Equipment operation and photography is remotely controlled from outside using a computer with ZEN 2 Core software. The microscope is also suitable for topography imaging with its 3D multi focus software that combines images on the z-axis.

4.3.1 General Characterisation

The cut-out sample is mounted, ground, and polished and then etched with Nital to reveal the microstructural features. Different objective lenses are used for the evaluation of the weld, including 5x, 10x, 20x, 50x, and 100x. The exact magnification is different in the imaging due to apertures and intermediate magnifications. The characterisation includes imaging of all different regions of the weld microstructure such as the fine- and the coarse-grain regions of the heat affected zone, the fusion line and the weld beads with reheated regions. The characterisation is done for both the inner and outer sides of the RPV wall since the inner side is welded with the SAW and the outer side with the MMA method. Additionally, the metal phases and grain size can be determined. The LOM evaluation in this project is mainly used for the weld metallography and evaluation of the phase and weld structure where the fracture has initiated.

In the general characterisation, two corner pieces of trepan 3 side slab are investigated, as one is next to the inner surface from the SAW weld and one is next to the outer surface

from the MMA weld area. The pieces are mounted in electrically conductive Struers PolyFast hot mounting resin using Struers Citopress-20. The mounted specimens are then ground with Struers LaboForce-100 with grit 220, 500, 1200 and 2400 SiC papers and continued with polishing by 3 μm, 1 μm and 1/4μm diamond suspension on polishing cloths Struers MD/DP-Mol (3 μm) and MD/DP-Nap (1 and 1/4 μm). The samples are then washed in ethanol with an ultrasonic washer for several minutes, dried, and stored in a desiccator, if not immediately etched and investigated. An evaluated sample from the inner wall is shown in Figure 4.3.

4.3.2 Cross-section Evaluation

Cross-sections from the Charpy-V specimens are cut by EDM after the fractography has been performed using scanning electron microscopy (SEM) and the initiation sites identified. The cross-sections are cut as close to the fracture sites as possible, mounted, ground and polished to mirror finish until 1/4 μm. The removed thickness is measured to get as close to the initiation site as possible. The samples are then etched for an optical microscopy evaluation. After imaging the samples are polished again for the SEM imaging. An elemental analysis is done using energy dispersive X-ray spectrometer (EDS). The initiation site imaging on optical microscope must be done first, since the EDS causes carbon contamination on the evaluated location, and therefore the surface does not erode in the etching. The aim of the cross-section evaluation is to determine in which microstructural part and phase of the weld the fracture has initiated, i.e., the weld bead, reheated region or an interface, or whether there are inclusions or some other inhomogeneties in the region. These results are then compared with the results from the mechanical testing to improve the understanding of factors affecting the brittle fracture initiation. The evaluation location cannot be obtained at a very high accuracy, but it should be within maximum of 0.1 mm from the primary initiation site.

4.4 Scanning Electron Microscopy

In conjunction with LOM, scanning electron microscopy is often utilised due to its large variety of magnifications and exceptional resolution range [57]. In principle, a beam of incident electrons are generated in a column above the sample chamber. The electron beam is produced usually by a tungsten filament, tungsten field emission tip, or a Schottky emitter, and the energy of the incident electrons can be on a range of 100 eV to 30 keV. The beam is focused by a series of electromagnetic lenses in the column and directed by scanning columns at the end of the column. The imaging is obtained by scanning the incident electron beam across the sample surface and the emitted electrons are detected. The intensity of the emitted electrons determines the brightness of the displayed image. Different signals are generated from material under the electron beam and detectors collect the spectrum for further analysis. Typically, secondary electrons and backscattered

electrons are detected for different imaging purpose. Due to higher spatial resolution, the secondary electron imaging is mostly used in the fractography. Furthermore, the depth of field is advantageous for higher lateral resolution and the images formed on computer are rather easy to interpret. For qualitative and quantitative chemical analysis, an energy dispersive X-ray spectrometer is attached to the SEM to conduct chemical analysis of the investigated area. Due to these benefits, SEM evaluation is used to carry out fractographic evaluation and detailed microstructural characterisation.

The SEM used in the VTT CNS laboratory is a field emission gun (FEG) Zeiss Crossbeam 540. For the chemical composition, the EDS analysis is conducted with an EDAX Octane Plus EDS connected to the SEM.

4.4.1 Fractography of Charpy-V Specimens

The Charpy-V impact toughness specimens are tested according to the standard SFS-EN ISO-148-1:2016 [58]. The tests are performed in the VTT CNS laboratory by Zwick RKP450 instrumented pendulum with automatic temperature control and feeding system. The pendulum has a 2 mm striker with the nominal impact energy of 300 J, and instrumented strain gauges to record the force versus time signal that can be transformed into an estimated displacement of the specimen. The test equipment is calibrated and the frictional loss was measured during each strike, giving consistently approximately 1.0-1.3 J energy loss value. The standard specimen shown on the left in Figure 4.4 has dimensions of 55 mm $\times$ 10 mm $\times$ 10 mm with a V-notch in the middle of the long edge. The notch has an angle of 45°, depth of 2 mm, and root radius of 0.25 mm. The specimens are measured before testing with a dimensional measurement system OGP CNC Flash 200 MS. The specimen is fed from the condition chamber on the pendulum supports so that the notch is aligned by 0.5 mm in the middle of the symmetry-plane between the supports. The specimen is struck by the striker on the opposite side of the notch. The transition temperature reference points of 28 J, 41 J and 68 J are determined.

The initial test temperature was chosen based on the reference data, and following temperatures were affected by the development of the transition curve. The samples are cooled in a tempering chamber for 30 minutes by using liquid nitrogen. At the moment of testing, the sample is transferred to the test position, and no more than 5 seconds shall pass between the specimen being outside the tempering unit and then impacted by the striker. After the failure, the samples are collected and the fracture surfaces are visually evaluated according to the ISO-148 or ASTM E23 standard [59]. On the right of Figure 4.4 is schematically shown the justification for the percentage of fracture appearance that is done for the specimen from the fracture surfaces. The differences between the ductile and brittle fractures are not always clearly distinguished visually, yet the quantitative results are used following the standard.

After the fracture appearance evaluation, the specimens are taken to SEM investigation.

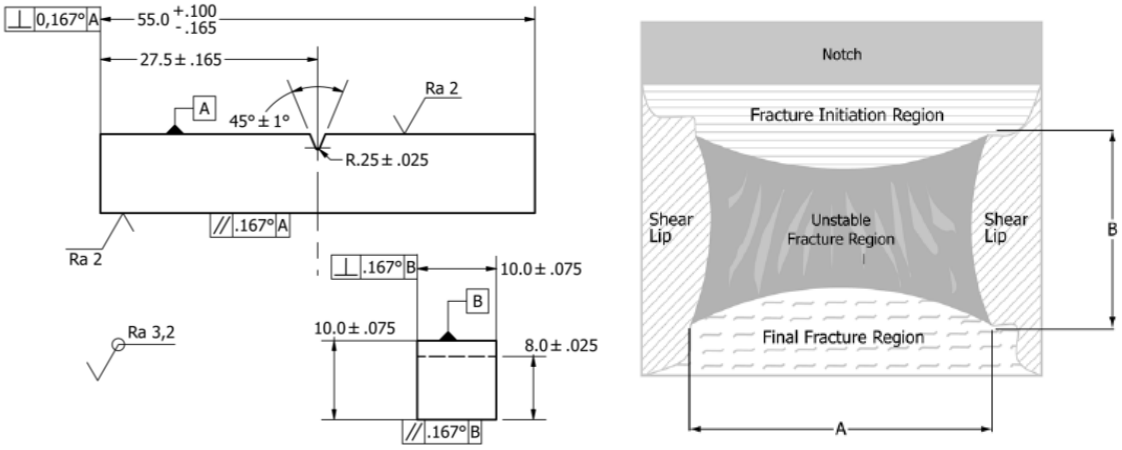

Figure 4.4. *On the left shows standard Charpy V-notch specimen with dimensional requirements. On the right is schematic guide for the determination of the percentage of fracture appearance. The shear and final fracture regions are usually ductile fracture areas, while the unstable fracture region refers to brittle cleavage fracture [59].*

The specimens are attached to a sample holder with both fracture surfaces exposed to the SEM observation. The fracture surfaces are analysed using SEM. The aim is to find the primary initiation site of the fracture from which the images are taken at several different magnifications, ranging from 50x to 5000x. The distances from the primary initiation site to the V-notch and the nearest side surface are also measured. After the determination and imaging of the primary initiation site, the EDS analysis is performed to obtain an elemental analysis of the possible initiation features and its surroundings. The specimen is contained in an air-tight place such as a desiccator to prevent excessive oxidation before the SEM observation.

4.4.2 Secondary Particle Determination

The secondary particles are determined by SEM and EDS using Genesis software. They are mostly inclusions such as alloy sulphide particles in the base material and oxide inclusions in the weld. The scope of the analysis is to determine the size, geometry and distribution of inclusions in the investigated weld metal. For the size distribution, an automated feature-sizing analysis is used, and the automatic recognition is based on image brightness. Additionally, the elemental analysis is performed with Genesis Chem at the centre of each particle. The used magnification is 1500x which covers the area of 72 μm $\times$ 57 μm per field. The resolution is 2048 px, making a pixel size of 35 nm, and the smallest detectable inclusion size is 2 px, i.e., 70 nm. This is considered sufficient for the relevant inclusions. [60] The precipitate particles are expected to be present as well, but these particles are very small and therefore are not suitable for identification using the same methods than the inclusions. Secondary particles are often found also on the fracture surfaces in the bottom of ductile fracture dimples.

5 RESULTS

The results of the experiments are introduced in this Chapter. The outcomes are explained along with the descriptions of the practices used in the experiments and analyses. In the general characterisation, two samples from the inner and outer wall sides are investigated and reported separately. In the Charpy V-notch impact toughness testing, there are in total nine specimens that are all analysed in a similar manner. However, to ease the reading of the results, not all the data of all the specimens are given but, a comprehensive summary is provided by presenting the results of two specimens tested at different temperatures, i.e., from different parts of the transition curve.

5.1 Macrohardness

In the beginning of the project, the weld metal characterisation was started with general analysis of the mechanical properties by measuring the macrohardness of the weld through the wall thickness from the inner side to the outer side. The side slab cut-off from trepan 3 was divided into three smaller sections, 3S1, 3S2, and 3S3, as seen in Figure 4.1 and then ground, polished, and measured using a 10 kgf load. The hardness matrices for plates 3S1 and 3S2 included 276 data points with a 3 mm $\times$ 3 mm spacing between the indentations. The plate 3S3 is different in shape, and therefore the hardness matrix included 299 data points with 3 mm $\times$ 2 mm spacing. The mean diameter of the indentations is of a magnitude of 0.3 mm.

For the analysis of the HV10 measurements, the length of the middle section of the weld, being inclined in the trepan, was measured as shown by the arrow in Figure 5.1, giving the length of 85.2 mm. The data points over the length of the arrow were collected from the inner wall to the outer wall, and a hardness profile shown on the left of Figure 5.2 was obtained. Further, the indentations were divided into as-welded and reheated microstructures, as seen on the right of Figure 5.2. The first results from the inner wall up to approximately 12 mm are lower due to the thermal effect from a stainless steel cladding process. The surface cladding has been removed from the trepan to reduce the activity of the trepans due to the contamination of the surface. The results without the thermally affected zone have an average of 210 HV10 with the variation of 5 HV10, which is typical for the weld microstructure in question. A total of 60 indentations was included in the evaluation through the weld thickness, of which 9 indentations were affected by the cladding. However, the overall hardness does not show a clear trend between the inner

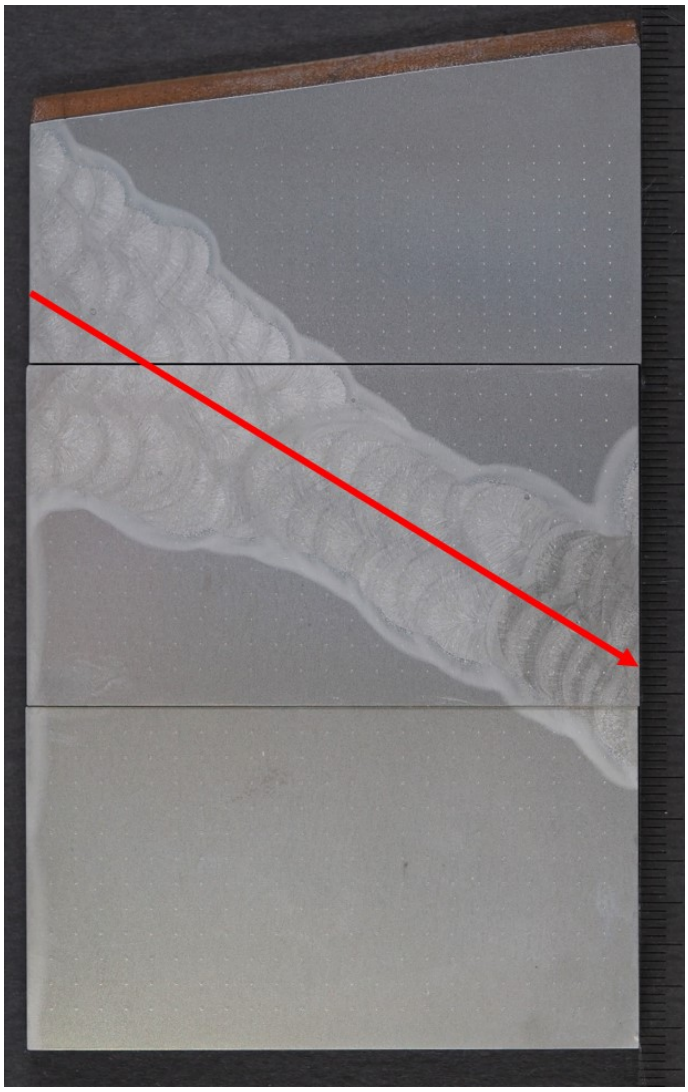

Figure 5.1. *HV10 profile direction through the weld build-up thickness from the inner wall to the outer wall. The plates from bottom to top are numbered as 3S1, 3S2, and 3S3. The scale on the right edge has a line spacing of 1 mm.*

and outer walls of the weld.

The hardness distribution over the heat-affected zone, starting from the base material to HAZ to the weld metal, was analysed. The data points from the middle section of the wall thickness were collected, and the following curves are seen in Figure 5.3. There are two curves, one for the plate base material (plate BM) and one for the forging base material (forging BM). Furthermore, the hardnesses of the microstructural features in the weld are divided into as-welded and reheated regions. The fusion line between the weld and HAZ is demonstrated by the vertical line located at the zero distance.

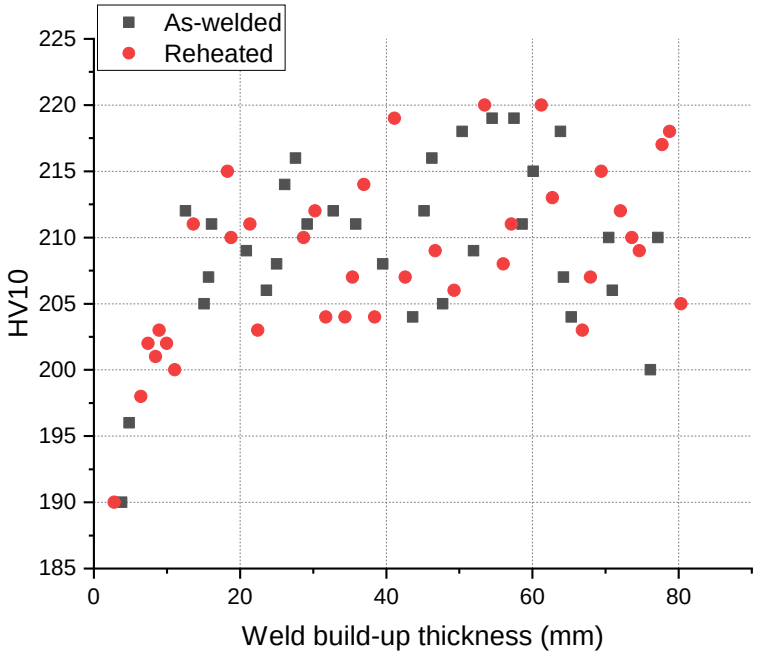

Figure 5.2. *HV10 results through the wall thickness in the cross-section investigated separately for the as-welded and reheated regions in the weld. The weld build-up thickness is measured from the inner wall to the outer wall.*

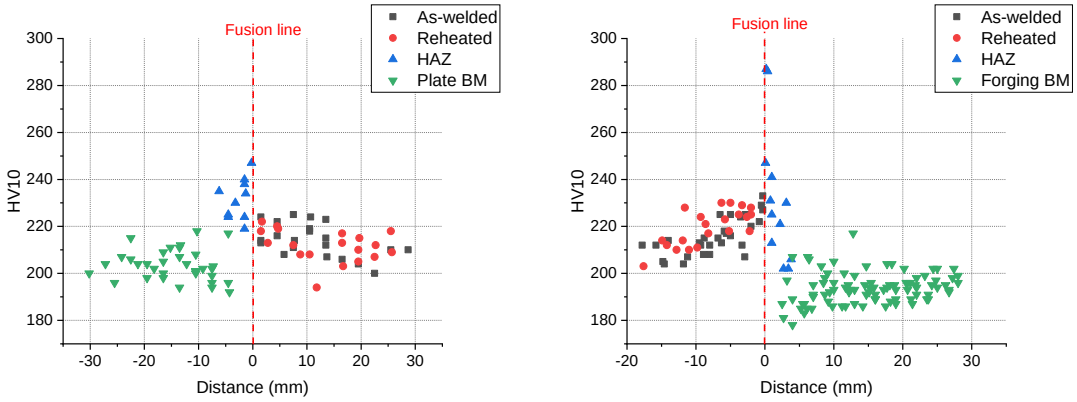

Figure 5.3. *HV10 results over the weld. On the left is the hardness profile from the plate base material to the HAZ and to the weld. On the right is the profile from the weld to the HAZ and to the forging base material. The fusion line is set at the zero distance.*

After the hardness measurements on a 10 kgf load, the macrohardness with a 1 kgf load were measured over the HAZ to obtain more information about the local differences in hardness between the base material, the heat-affected zone, and the as-welded and reheated regions. The average size of an HV1 indentation is approximately 0.1 mm. The indentation rows were programmed to align between the indentations from HV10 measurements on the 3S2 and 3S3 side slabs to obtain measurements from both base materials. In the 3S2 plate side the row spacing is 3 mm, while in the 3S3 forging the row spacing is 2 mm. The indentation spacing is 0.5 mm for both cases. Since one corner of

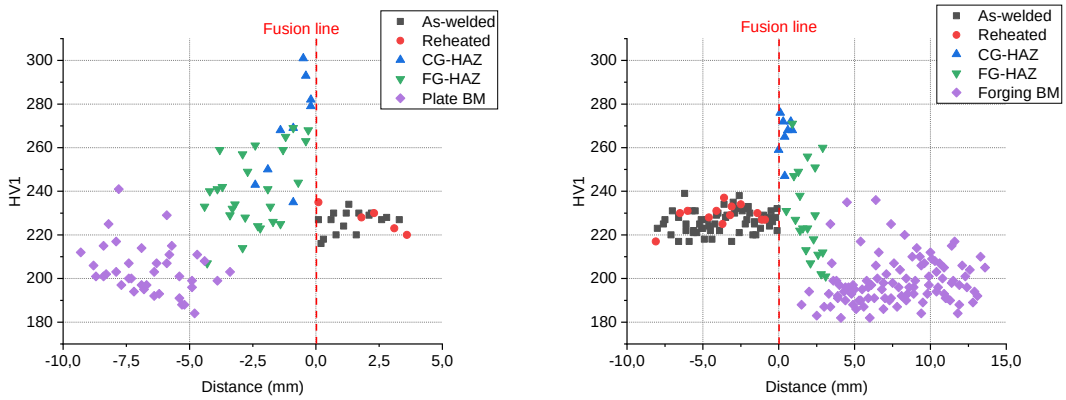

Figure 5.4. *HV1 results with the fusion line at zero distance. On the left is the hardness profile from the plate base material to the HAZ and to the weld. On the right is the profile from the weld to the HAZ and to the forging. Observe the different length of the measurements across the fusion line compared to the HV10 measurements.*

Table 5.1. *HV10 and HV1 macrohardness results by the weld regions.*

	HV10			HV1		
Region	Average	Max	Min	Average	Max	Min
Forging BM	194±7	217	178	198±11	236	182
Plate BM	210±7	218	192	204±12	241	184
Weld metal	215±8	233	194	227±5	239	216
Forging HAZ	233±28	287	202	240±24	276	201
Plate HAZ	232±9	247	219	248±22	301	207

the 3S2 slab had been cut for microstructure characterisation, the last row is incomplete and a total of 94 instead of 100 data points are obtained. On the other hand, in the 3S3 slab there are in total 201 HV1 data points. The first 100 indentations are in the base material due to the wrong estimation of the HAZ location before etching the surface. The remaining 101 indentations are better located in the weld and in the HAZ, and all the data has been included in the hardness profile. The HV1 results are plotted in Figure 5.4 similar to the HV10 over-the-weld profile analysis.

Both hardness profile curves, HV10 and HV1, show a similar trend in hardness where the highest hardness is at the coarse-grained heat-affected zone located right next to the fusion boundary. The statistics of the macrohardness results are tabulated in Table 5.1. In the plate base material, a few of the HV1 results of the HAZ are higher than in the forging as the maximum data point reaches 301 HV1, while the maximum in the forging is 276 HV1. Generally, the average HV1 values of the forging and the plate HAZ are similar, and the large deviation is due to the microstructure of the coarse-grained HAZ. The hardness decreases within the HAZ rapidly by the distance from the fusion line to the base material. In the HV10 measurements further into the base material, the hardness of the forging base material is ca. 11 HV10 lower than the average weld hardness, and the plate base material only ca. 5 HV10 softer than the weld. Additionally, there is a

ca. 16 HV10 difference between the averages of the forging and plate materials when the deviation for both is $\pm$7 HV10. However, in the HV1 measurements, no difference between the hardnesses of the base materials is seen. Therefore, the variation within the base material is normal and a large number of data gives a statistically valid result of similar level of hardness. The variation is further discussed with correlation to the microstructure, as the few data points at the higher level of hardness may be due to segregation lines and hardened microstructures.

The weld hardness shows a slight decreasing trend with the distance from the fusion line. However, no clear difference is seen in the hardness between the as-welded and reheated regions in the weld, which shows that the weld is generally homogeneous. In the HV1 curves, the indentations are focused at more distinct microstructural details, and for example the fine- and coarse-grained HAZ are separated by the higher hardness of the coarse-grained HAZ. The hardness of the weld metal is further discussed in Section 5.3, where HV0.3 hardness is measured from the cross-section samples and the indentations are focused at even more distinctively in the different weld microstructures.

5.2 Microscopy

The microstructure of a multipass weld is a complex structure with separated regions. The as-welded microstructure is the initial solidified weld, and the region that has been under one or multiple thermal cycles is referred to as reheated or twice or more reheated region. The weld bead structure with the as-welded and the reheated regions can be recognised due to their distinct shape and grain structure. The multipass weld structure of the whole weld joint is depicted e.g. in Figure 5.1, which characterises a good quality weld made with SAW and MMA methods. In this Section, the results of the microscopy characterisation are presented. The first evaluation was made using an optical microscope to obtain a general characterisation of the weld microstructure. The further microscopy results are from the fracture surface investigation using a scanning electron microscope.

5.2.1 Microstructure

The weld microstructure characterisation was first done for the corner cut from the side slab 3S3, which is from the inner side of the RPV wall and welded with the submerged arc welding method. The macrographs of the mounted and etched sample is shown on the left of Figure 5.5. The microstructure characterisation was later done similarly for the corner cut from the outer side of the RPV wall seen on the right of Figure 5.5. The outer side seemed to have etched differently as it appeared darker compared to the rest of the weld. It was revealed that the outer side was welded with the manual metal arc welding technique which has different heat input than the submerged arc welding, and the filler

metal was slightly different in the chemical composition as well, explaining the different etching behaviour.

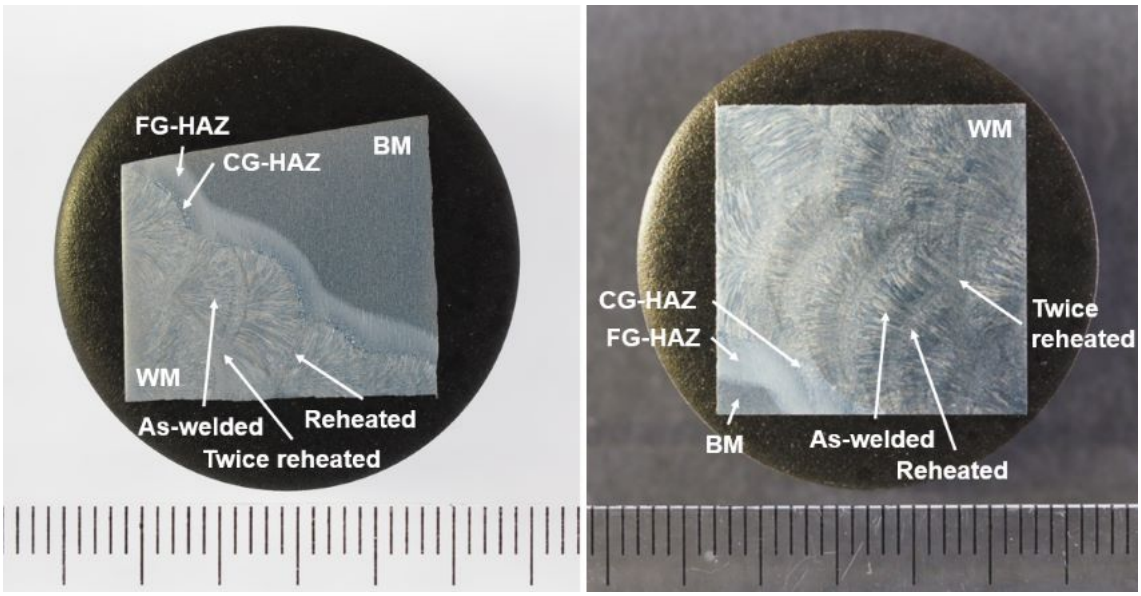

Figure 5.5. *Specimens used in the weld microstructure characterisation of the inner side (SAW) and the outer side (MMA) of the RPV wall. The scale on the bottom has a line spacing of 1 mm.*

In Figure 5.5 of the etched samples, the main microstructural features are pointed out. The base material in the left side image is the forging and in the right side image the plate. The weld metal consists of as-welded, reheated and twice or more reheated regions. Between the base material and the weld material is the heat-affected zone, which can be divided into coarse-grained and fine-grained microstructures. The height of the weld beads are approximately 1 mm smaller in the MMA weld than in the SAW specimen due to the different welding parameters. The approximate weld bead heights are roughly 3 mm in the MMA and 4 mm in the SAW welds.

Microstructure of the Inner Wall Side

The microstructure of the forging base material is bainitic, as shown in Figure 5.6. The upper bainite forms at higher temperatures and the lower bainite at lower temperatures at moderate cooling rates. Their microstructures are distinguished by the carbon segregation. In the upper bainite and at the higher temperatures, the carbon diffusivity is higher and it precipitates in lines in larger laths, whereas the rest of the grain is without carbon and appears lighter in colour. In the lower bainite and at the lower temperatures the carbon diffusivity is lower, and therefore the carbon forms smaller needle-like precipitates throughout the grain. Hence, the lower bainite appears darker than the upper bainite in the optical micrographs. Single ferrite grains appear as light-coloured grains with distinct boundaries in the microstructure. The dominating phase in the forging is the upper bainite.

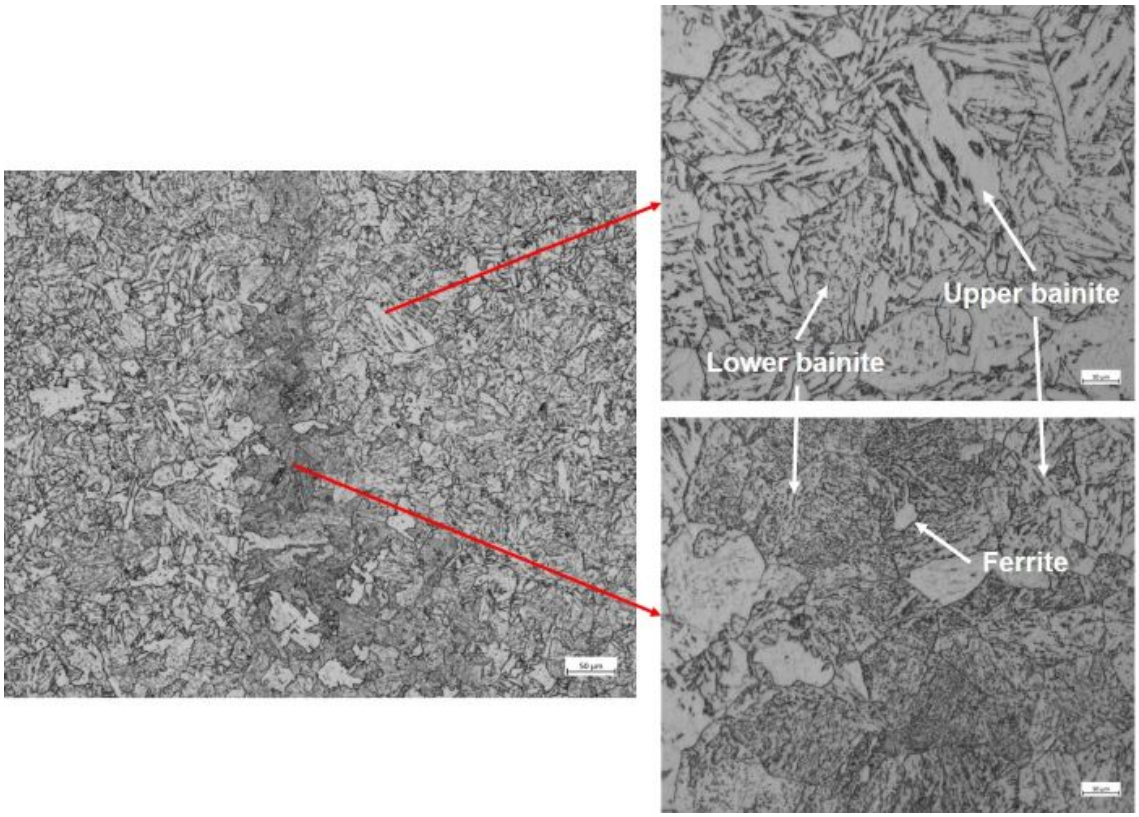

Figure 5.6. *Bainitic forging base material. The ghost line is shown in the micrograph on the left. In the two figures on the right, the microstructures of the typical base material and the ghost line are shown at a higher magnification.*

In Figure 5.6, a so-called ghost line appears as a dark line in the base material. Ghost line is a segregation that forms during manufacturing of the forging, where the chemical composition differs locally from the surrounding material [61]. Typical for this segregation is to contain more for example carbon and manganese, which provide favourable conditions for the lower bainite to form. The ghost lines in the investigated forging are relatively weak. The hardenability is higher in the ghost lines, and therefore also martensite grains may appear. Due to the phase structure and changes in the chemical composition, the hardness is typically higher in the segregated areas than in the typical base material.

The heat affected zone between the base material and the weld metal is shown in Figure 5.7. The boundary between the HAZ and the base material is not a distinct line dividing the two regions in the microstructure. Minor grain growth is observed at the boundary, hence this region is also referred to as a partially austenitised and tempered region [7]. However, from the HAZ boundary towards the weld, the major microstructural regions are the fine-grained and coarse-grained heat affected zones. The thermal effect is smaller at further away from the fusion boundary, and the cooling rate is slow due to the lower thermal gradient. The phase structure is not significantly affected, as the fine-grained HAZ normally contains a mixture of upper and lower bainite. The fine-grained HAZ is shown in Figure 5.8. At austenitisation temperatures, carbon diffuses from the lighter areas to the darker areas, as more light-coloured ferrite grains are observed in the fine-

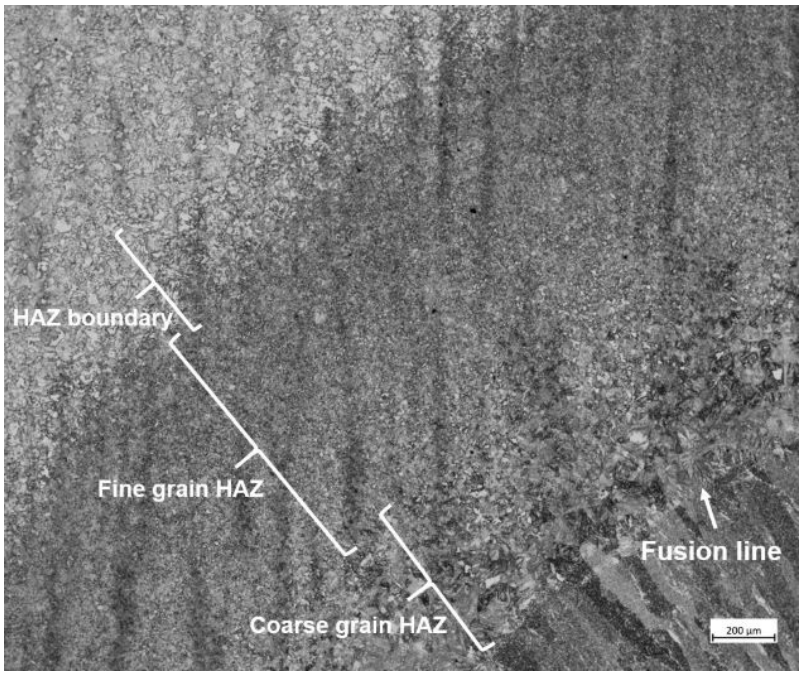

Figure 5.7. *The heat-affected zone regions in the forging base material.*

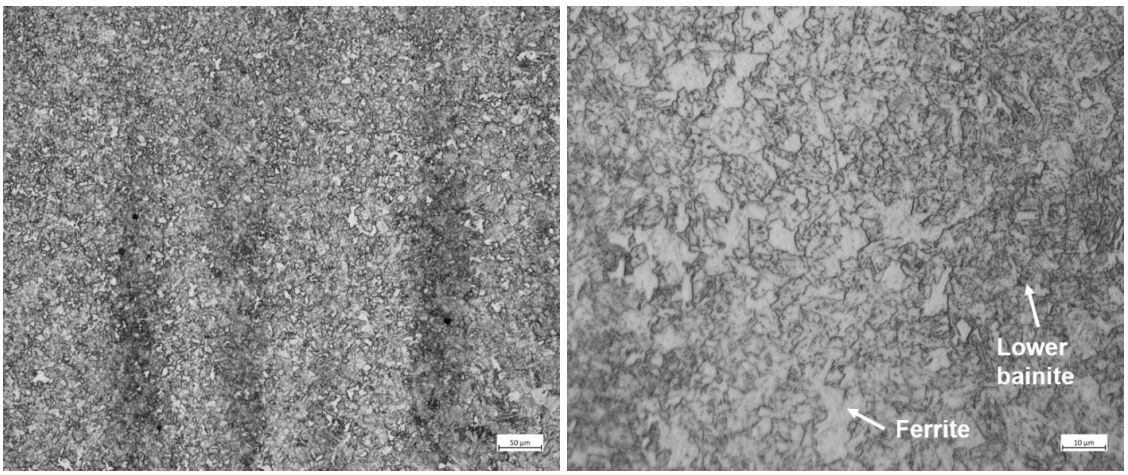

Figure 5.8. *Fine-grained heat-affected zone microstructure. The ghost lines appear in the left hand side image in the forging base material.*

grained HAZ than in the base material. Otherwise the microstructure is dark-coloured, indicating the presence of lower bainite. The ghost lines remain in the microstructure since the temperature is not sufficiently high to significantly change the grain size or chemical composition. In these areas a small amount of martensite is observed due to the quenching at cooling. Also, the variation in the grain size indicates partial recrystallisation.

Closer to the fusion zone and the weld metal is the coarse-grained HAZ, which is present only along the weld bead. The high thermal input causes recrystallisation and thus grain coarsening due to the temperature reaching the full austenitisation region. Since the temperature is so high, the thermal gradient is large and the cooling rate is relatively fast. Due to the high diffusivity of carbon and its escape from the ferrite, the hardenability

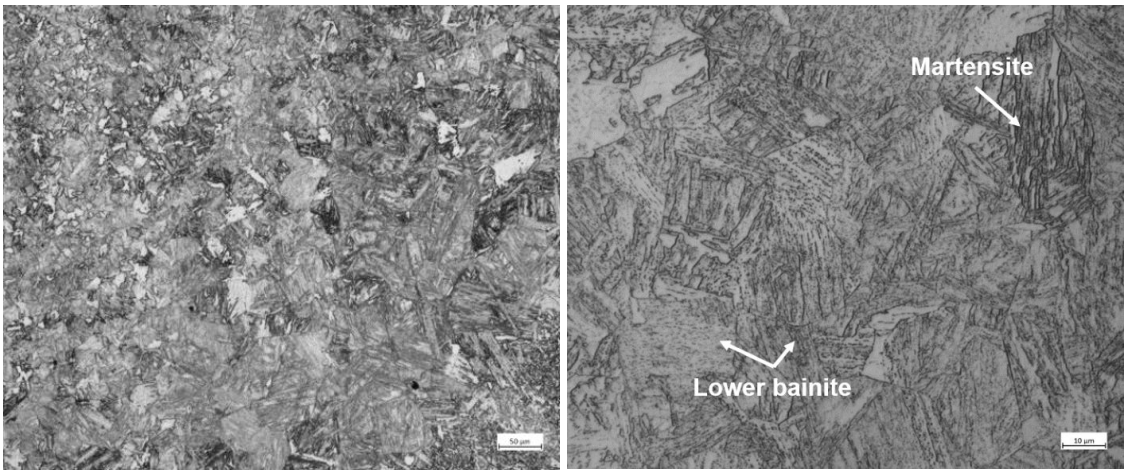

Figure 5.9. *Coarse-grained heat-affected zone microstructure.*

increases, and therefore the resulting microstructure is a multiphase structure of dominating lower bainite and some martensite, which is seen in Figure 5.9. Martensite has the typical features of long and fine laths, and is thus easily distinguished from the upper bainite.

At the fusion boundary, the austenite grains in HAZ act as parent grains for the weld metal to grow epitaxially towards the centre line of the weld pool. The columnar grains begin to grow at the most favourably oriented parent grains. In Figure 5.10, the parent austenite grain is visible in the coarse-grained HAZ, although the structure inside the grain has developed during cooling. The phase transformation at the fusion boundary changes the HAZ bainite into the acicular ferrite in the weld solidification structure. Acicular ferrite has a particular small basket-weave structure. At the grain boundaries, the pre-eutectoid grain boundary ferrite is observed as lighter areas, although its amount is relatively small. Although the grain boundary ferrite nucleates first at the austenite grain surfaces, the alloying elements, such as manganese, promote the growth of acicular ferrite over the grain boundary ferrite [62]. The growth of acicular ferrite is rapid also due to the sufficient amount of non-metallic inclusions, such as oxides. Furthermore, small amount of Widmanstätten ferrite is seen in the microstructure, but only locally.

Typically the coarse-grained HAZ is between the fine-grained HAZ and the fusion boundary in the outermost weld bead, as seen in Figure 5.10. However, due to the uneven thermal impact in the multipass weld bead structure, the coarse-grained region may be nearly negligible, and locally the fine-grained HAZ is observed as in Figure 5.11. The adjacent weld beads have refined the microstructure of the coarse-grained HAZ and similarly it has affected the as-welded microstructure to form the reheated microstructure. The boundary area between the reheated and as-welded microstructures can be called a partially reheated microstructure.

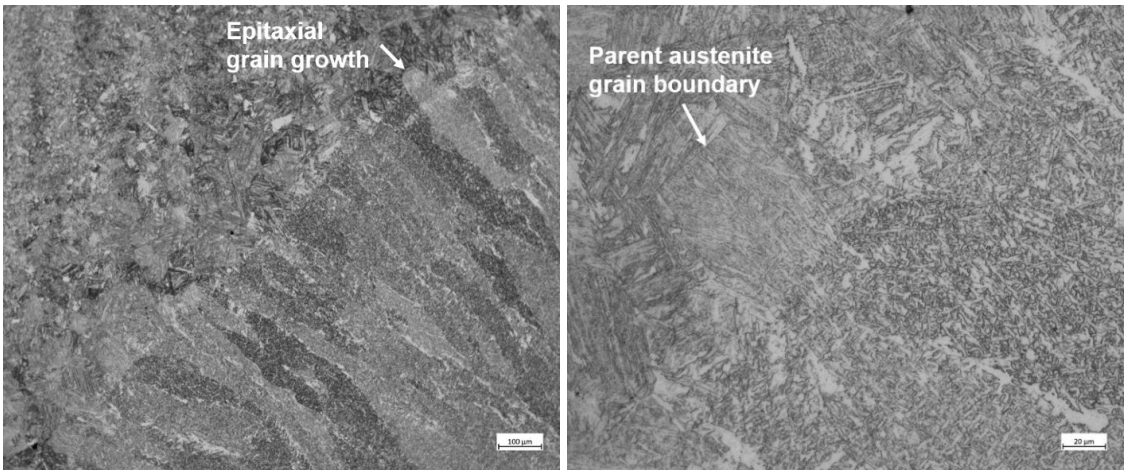

Figure 5.10. *Fusion boundary between the weld metal and the HAZ with epitaxial grain growth. In the CG-HAZ, the parent austenite grain is visible.*

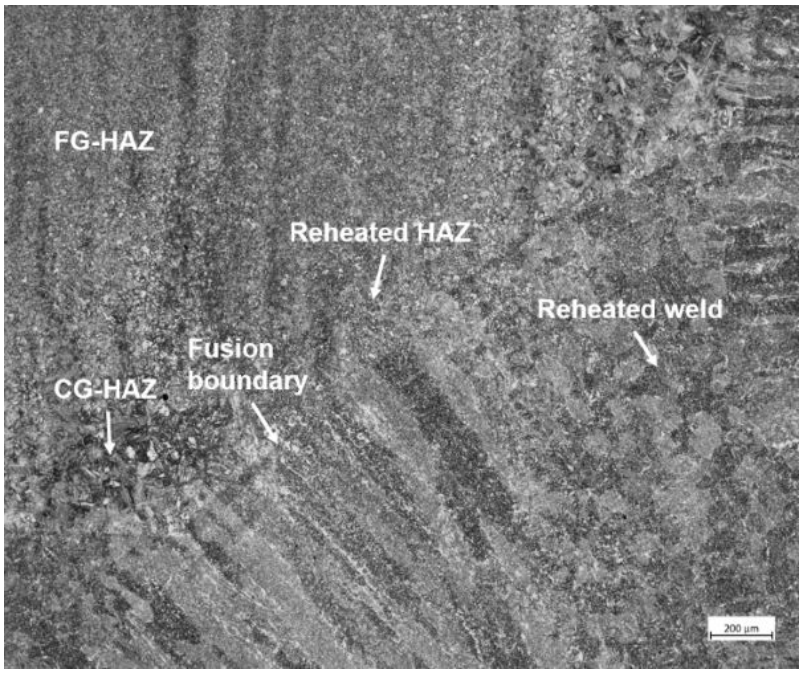

Figure 5.11. *Fusion line of the outer weld beads with reheated regions.*

In the multipass weld, the microstructure is complex including the as-welded microstructure and the welded regions under one or more thermal cycles. The as-welded microstructure near the fusion line has an unaffected columnar grain structure showing the grains growing towards the weld pool centre line, as seen in Figure 5.12 a. At a higher magnification it is seen that the microstructure is dominated by acicular ferrite with small amounts of grain boundary ferrite between the columnar grains. In a good quality weld, more than 70% of acicular ferrite in the microstructure is desired due to its high toughness and ability to prevent the unfavourable effect of the grain boundary ferrite or the Widmanstätten side plates. This is true with a clear margin in the weld in question. The grain boundary ferrite is relatively easily detected as a long and narrow phase along the grain boundaries. The light-coloured ferrite is distinguishable from the small acicular

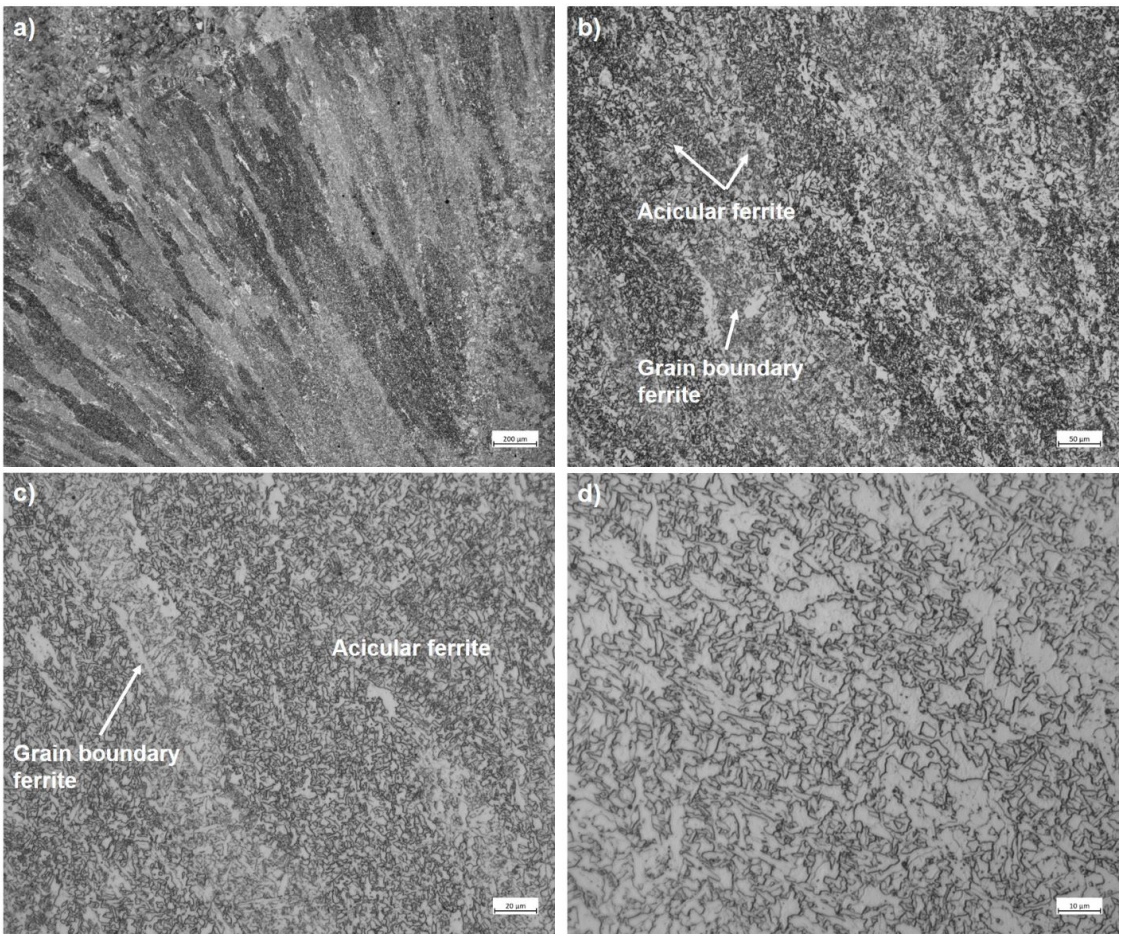

Figure 5.12. *Outer side of the weld bead with typical columnar grains and microstructure at different magnifications.*

ferrite containing multiple randomly oriented short needles. The microstructure is seen in Figure 5.12. Furthermore, the larger lines and colour differences in the microstructure of the acicular ferrite indicate differences in the orientations and strains within the weld bead.

Closer to the next weld bead in the as-welded microstructure, partial changes in the grain structure are seen due to the high heat input by the new weld, as shown in Figure 5.11. After welding a layer, a new one is welded on top of it, which changes the typical as-welded microstructure and further may change the mechanical properties. The reheated microstructure aligns with the fan-shaped weld bead as the new weld solidifies on top of the previous layer. The reheated region changes the columnar grain structure of the weld bead, and the microstructure of the acicular ferrite and grain boundary ferrite changes as seen in Figure 5.13. Hence, polygonal ferrite is observed as large light-coloured islands in the microstructure without a particular shape, and the amount of acicular ferrite decreases. Therefore, in the micrographs it can be relatively easily separated from the acicular ferrite but not as easily from the grain boundary ferrite. Due to the high heat effect, the driving force for carbon to diffuse out from the polygonal ferrite and carbon partitioning is relatively high. The polygonal ferrite has sufficient toughness properties,

and is therefore acceptable and also typical in the weld microstructure. The reheated microstructures in the middle of the weld joint are more thermally affected than those on the sides. In the multipass weld, a twice reheated microstructure has been exposed to two or more weld beads at different thermal cycles. The level of heat effect is seen for example in the amount of polygonal ferrite and carbon partitioning.

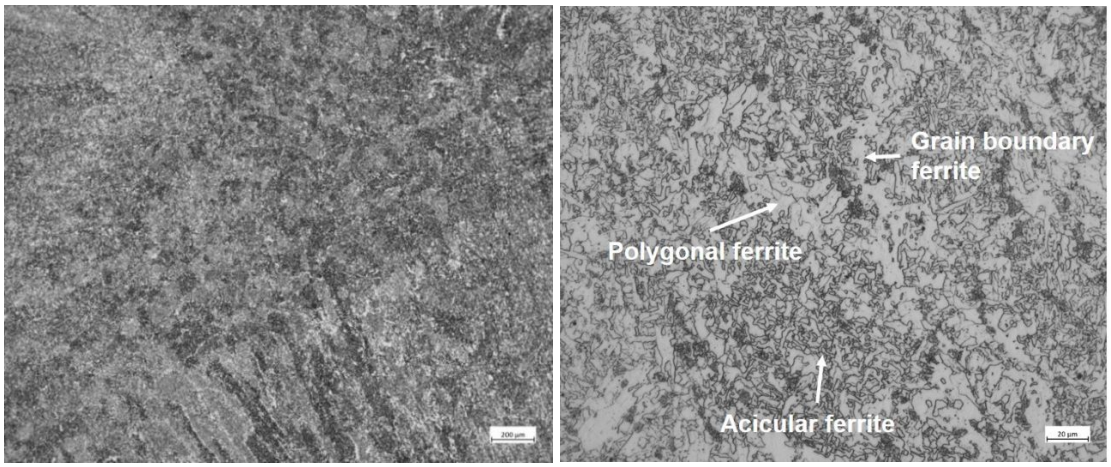

Figure 5.13. *Reheated microstructure with a boundary to the as-welded region in the image on the left. The ferritic microstructure is shown in the image on the right.*

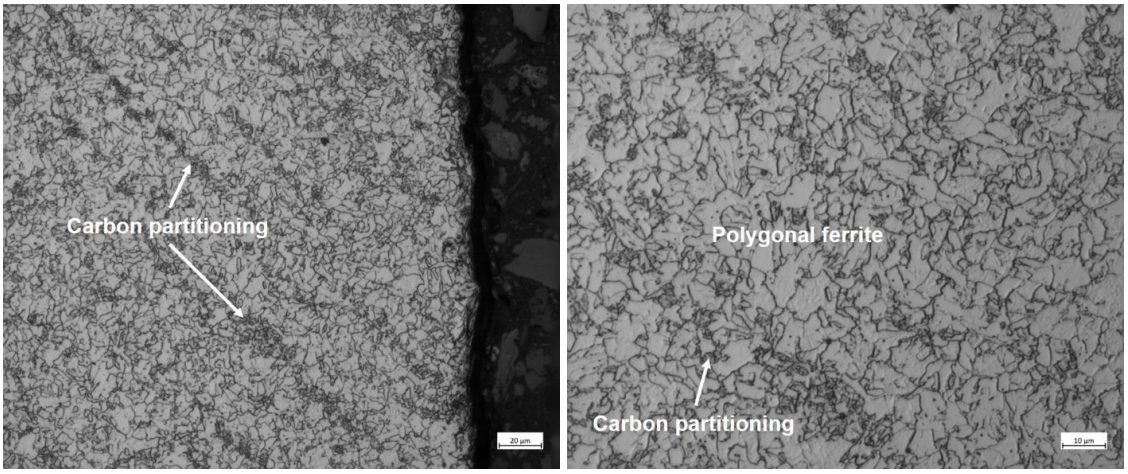

Figure 5.14. *Cladding heat-affected zone in the weld metal with a polygonal ferrite microstructure.*

On the inner wall side of the trepan, the cladding has caused the formation of a fine-grained heat-affected zone, and the microstructure in the weld resembles that of the weld bead reheated region. The microstructure is dominated by polygonal ferrite, and strong carbon partitioning is seen as darker lines in Figure 5.14. A similar thermal effect is seen in both the weld HAZ and the weld bead microstructure. Based on the microstructure, it can be assumed that the cladding does not have a negative effect on the weld metal.

Microstructure of the Outer Wall Side

So far, the microstructure characterisation and micrographs have been from the inner wall side containing the weld made by the submerged arc welding. Up to approximately 16 mm from the outer wall surface, the weld is made by the manual metal arc welding method, which has shown small differences in the chemical composition. The darker colour in the macroscale motivated to characterise the microstructure also for this side of the weld. The MMA welded part has, compared to that of the SAW weld, chemical composition with less carbon, nickel, molybdenum, copper, cobalt and aluminium, and more silicon and vanadium, as seen from the measurements 7 and 8 in Appendix A. The corner cut of the outer wall side specimen included a piece of the plate base material, whereas the inner wall side had the forging base material. In the plate base material, the microstructure is mixed upper and lower bainite similar to the forging, and the ghost lines are clearly seen in Figures 5.15 a and c.

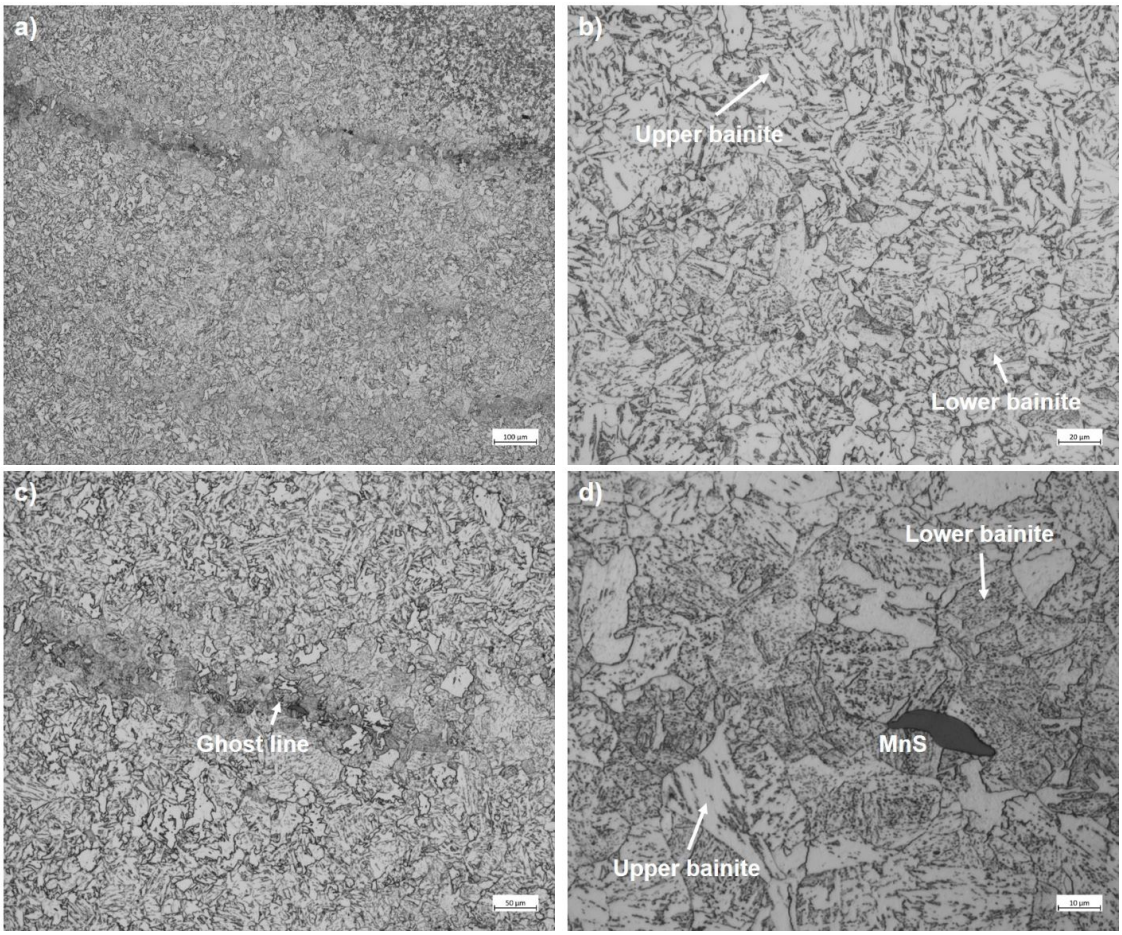

Figure 5.15. *Images a) and b) show the plate base material on the outer wall side with a MMA weld and typical bainitic microstructure. Images c) and d) show the ghost line microstructure and the manganese sulphide particle.*

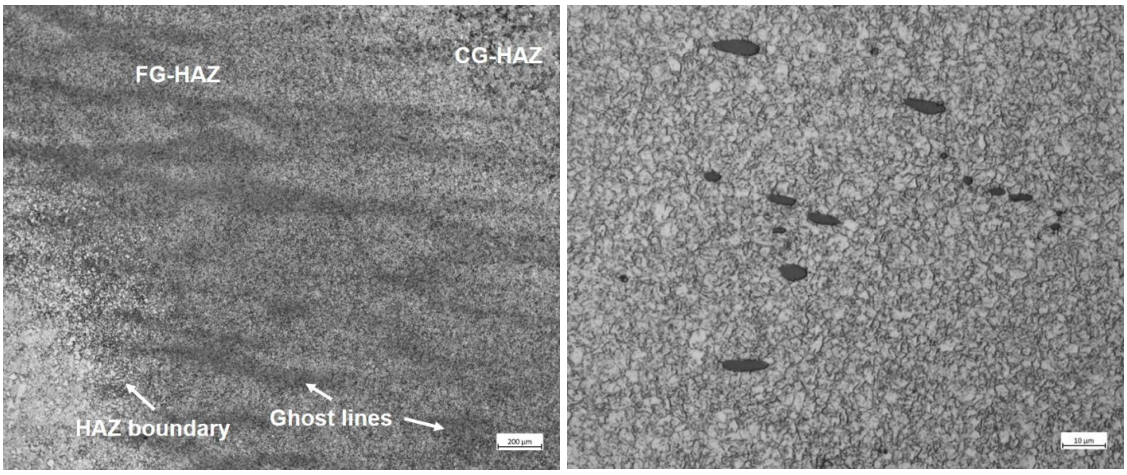

Figure 5.16. *Fine-grained HAZ in the plate base material. In image on the right is the fine-grained HAZ with manganese sulphide (MnS) particles in the ghost line.*

Ghost lines are not usually found in the plate metal, but in this case they may be explained by the large thickness. However, the ghost lines in the investigated material are relatively weak due to high-purity material. In these ghost lines, carbon and some other alloying elements such as manganese are segregated to a certain location [61], where, due to increased hardenability, lower bainite dominates. Additionally, relatively large manganese sulphide particles are found which typically form at high-temperature austenite grain boundaries as manganese lowers the solubility of sulphur in iron [7]. These normally round particles have deformed during rolling in the metal processing.

The fine-grained HAZ in the plate base material does not differ much from that in the forging base material, as seen in Figure 5.16. There are again very strong ghost lines that remain from the base material, as the grain size and grain structure are not significantly changed by the heat effect. The microstructure is a mixture of upper and lower bainite, however, in the ghost line several manganese sulphide particles were also found. In some parts the fine-grained HAZ is adjacent to the fusion line and is mixed with the reheated region from the weld beads. However, there are regions with a clear coarse-grained HAZ, where the microstructure is significantly coarser than in the surrounding HAZ and in the SAW weld. The coarse microstructure is seen in Figure 5.17, which is a mixture of lower bainite and martensite. The larger amount of martensite on the outer wall side is due to the manual metal arc welding process parameters and different heat input on the material. The heat input in MMA welding is smaller, hence the cooling rate is faster and therefore martensite formation is more probable. Additionally, large ferritic laths are seen in the microstructure.

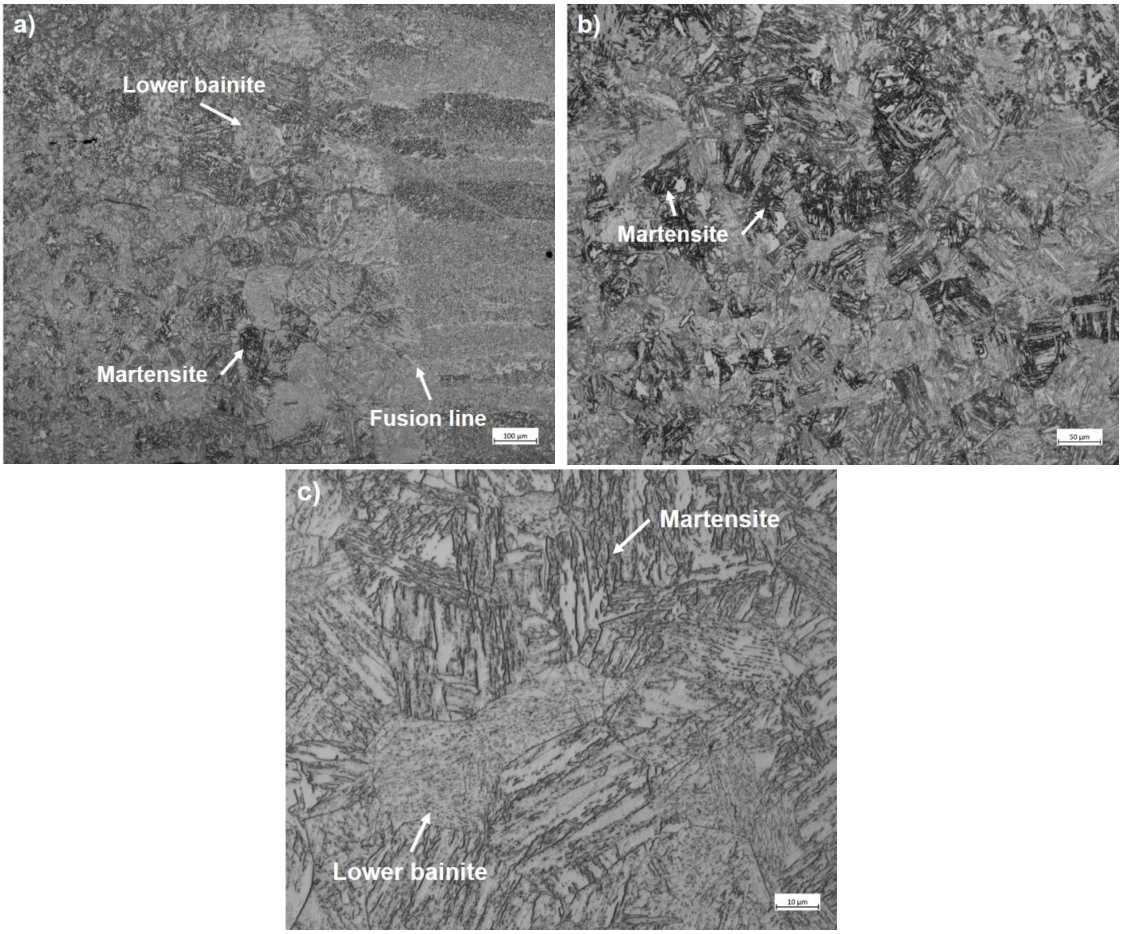

Figure 5.17. *Coarse-grained HAZ microstructure and fusion line with epitaxial grain growth inwards the weld.*

In the as-welded microstructure, the basic features are similar to the weld made by the SAW method. Acicular ferrite dominates in the columnar grains and the light-coloured grain boundary ferrite is seen between the long grains. The microstructure is shown in Figure 5.18. In the MMA weld, the acicular ferrite may be slightly finer than in the SAW weld, and more grain boundary ferrite is seen in the microstructure. Due to the differences in the chemical composition of the weld metal, small alloy carbides are found in the microstructure and the few square-like particles found are assumed to be titanium carbides. Although there is less carbon in the weld metal compared to the SAW weld, the carbide precipitates may be due to the electrode coating and different heat input in the welding. In addition to the titanium carbides, there are generally more second-phase particles in the MMA welded microstructure than in the SAW weld.

The reheated microstructure is dominated by polygonal ferrite, as seen in Figure 5.19. The assumed titanium carbides and inclusions are well seen in the reheated microstructure as dark small spots. The reheated microstructure is more light-coloured due to either less etching and contrast in the imaging or smaller carbon concentration. However, only small amount of acicular ferrite is found, and the grain boundary ferrite is relatively difficult to separate from the large polygonal ferrite. The reheated microstructure in Figure

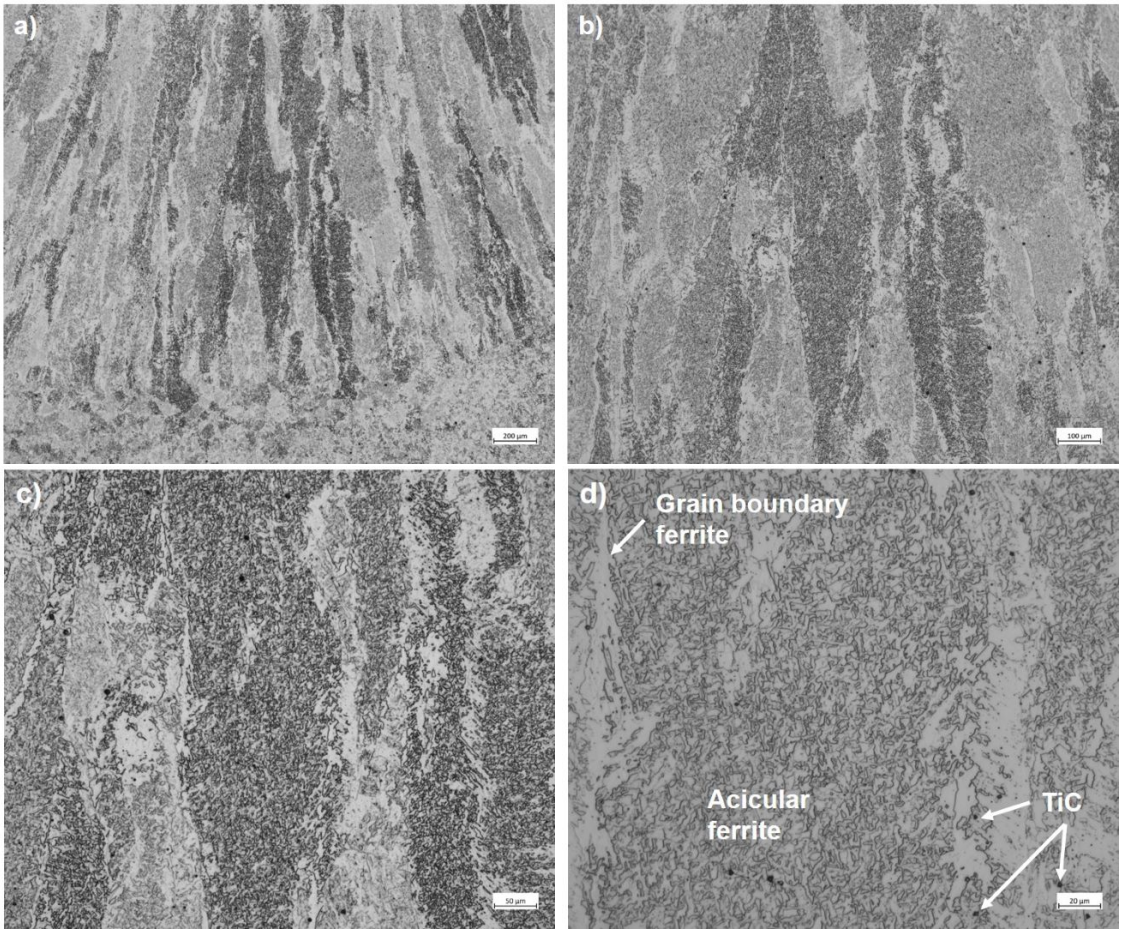

Figure 5.18. *Darker-coloured weld bead microstructure at different magnifications. In the a) the bottom shows also reheated microstructure, and in the d) the titanium carbide (TiC) particles are seen as indicated by the arrows.*

5.19 is located in the middle of the weld joint. Therefore, it has been subjected to several thermal cycles that have refined the grain structure and caused a significant change in the microstructure.

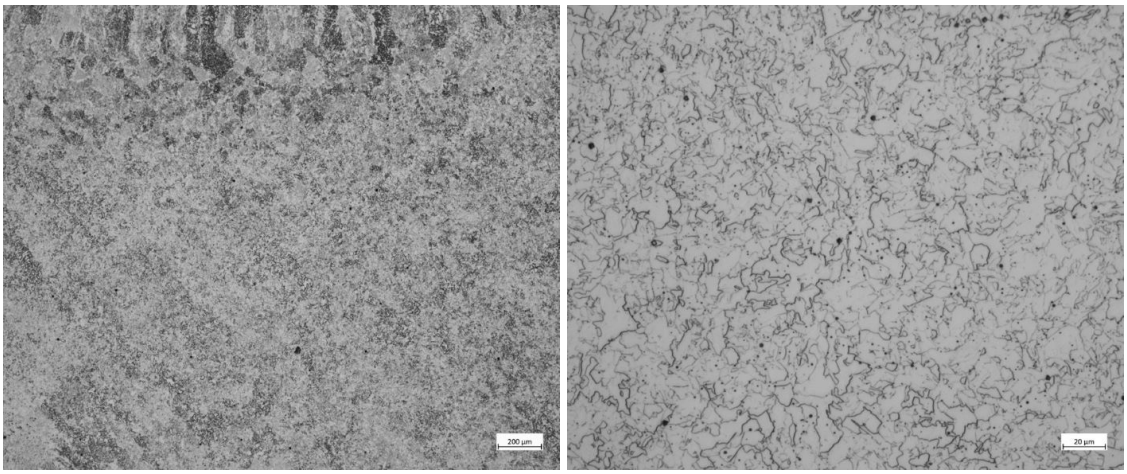

Figure 5.19. *Reheated microstructure after several thermal cycles and showing the inclusions at two different magnifications.*

According to the general characterisation of the microstructures, it can be concluded that the weld is of good quality in both parts, the inner and outer wall sides welded by the SAW and the MMA methods, respectively. Small differences were observed, but the overall phase structure is similar. The dominating acicular ferrite in the as-welded microstructure improves the mechanical properties of the weld, and the growth of grain boundary ferrite or Widmanstätten side plates are moderate. Additionally, small amounts of local martensite grains in the HAZ are surrounded by tougher bainite. Presumably, the long operating time and elevated temperature have thermally affected the martensite phase so that it is even less problematic in the microstructure compared to the beginning of the operation.

5.2.2 Fractography

In this Subsection, the results from the Charpy V-notch impact toughness tests are presented and the fracture surfaces are examined. In total nine CVN specimens, listed in Table 5.2, are from the lower shelf and the lower part of the transition curve, which were included in the investigation. The transition curve seen in Figure 5.20 shows the impact toughness results obtained by testing altogether 23 weld metal specimens in the BRUTE project. The transition curve includes 11 specimens from trepan 2 and 13 from trepan 3, all from one-quarter (1/4) depth of the trepan thickness such that they represent the same material in the same state.

Table 5.2. *Brittle fracture CVN specimens from the impact toughness tests. The columns show the specimen code, testing temperature, and impact toughness energy. The specimens are ordered according to the impact toughness energy.*

Specimen	Testing temperature (°C)	Impact toughness energy (J)
CVN 8	–79.2	41.9
CVN 11	–99.7	27.3
CVN 2B11	–79.4	27.0
CVN 12	–119.3	16.5
CVN 10	–99.6	12.8
CVN 2B5	–119.5	10.6
CVN 2B10	–119.3	9.4
CVN 9	–119.3	5.0
CVN 2B7	–119.5	4.6

The obtained transition temperatures are T_{28J} = -85 °C, T_{41J} = -75 °C, and T_{68J} = -60 °C, with uncertainty estimated to be $\pm$5 °C. The nine specimens included in the brittle fracture characterisation were those below the transition temperature T_{41J} = -75 °C and for which the primary initiation fracture site could be found. The chosen data points are

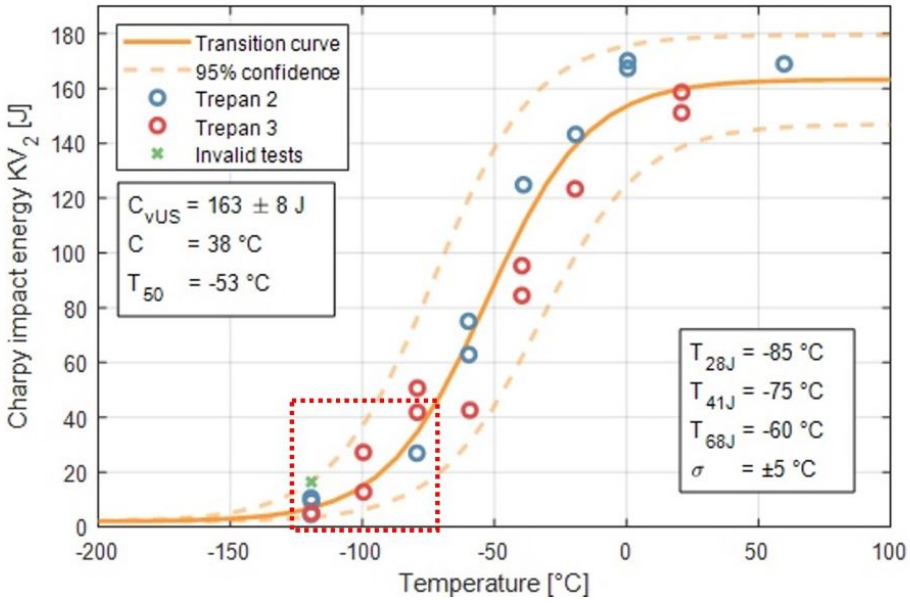

Figure 5.20. *Transition curve of all tested impact toughness specimens in the BRUTE project. The studied brittle fracture specimens are inside the red square.*

within the dashed box in Figure 5.20. The data point seen in the transition curve outside the box with the same test temperature as the specimen CVN 8 is from a sample for which multiple initiation sites could be found but the primary site could not be identified with certainty, which is the reason that it is not included in the further investigations.

After the impact toughness testing, the fracture appearances were examined visually and then microscopically. The selected nine specimens were treated similarly, however, in this Subsection only the results of two specimens from different parts of the transition curve are presented as representative examples. The specimen CVN 8 is from the lower part of the transition region and the specimen CVN 2B5 is from the lower shelf. In the fractography, the primary initiation sites were first traced using SEM, after which the chemical composition was analysed using EDS at the initiation location to obtain information about the possible particles, segregations, or special characteristics of the weld metal. The distance from the V-notch and the side surface was also measured, and the cross-section microstructures then evaluated.

Specimen CVN 8

Specimen CVN 8 was cut from trepan 3 and tested at the temperature of -79.2 °C, giving impact toughness energy of 41.9 J. The impact toughness is at the lower part of the transition curve region and below the determined temperature of brittle fracture. The primary initiation site was at a 4.143 mm distance from the side surface and 1.080 mm from the V-notch. The fracture surface was photographed after the testing, as seen in Figure 5.21, and the appearance was evaluated. The primary initiation site on both

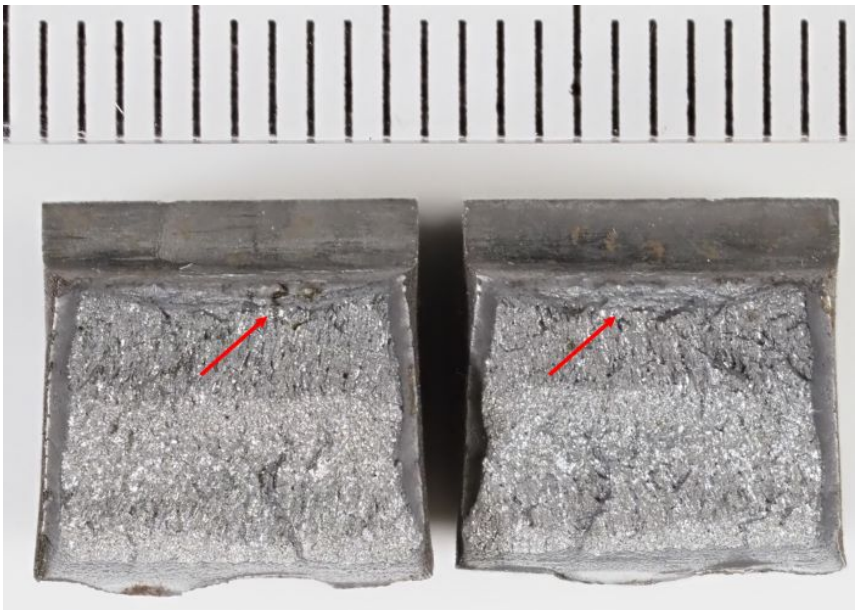

Figure 5.21. *Reprography images of the fracture appearance in specimen CVN 8. The primary initiation site is pointed out by arrows in the image. The scale on the top has a line spacing of 1 mm.*

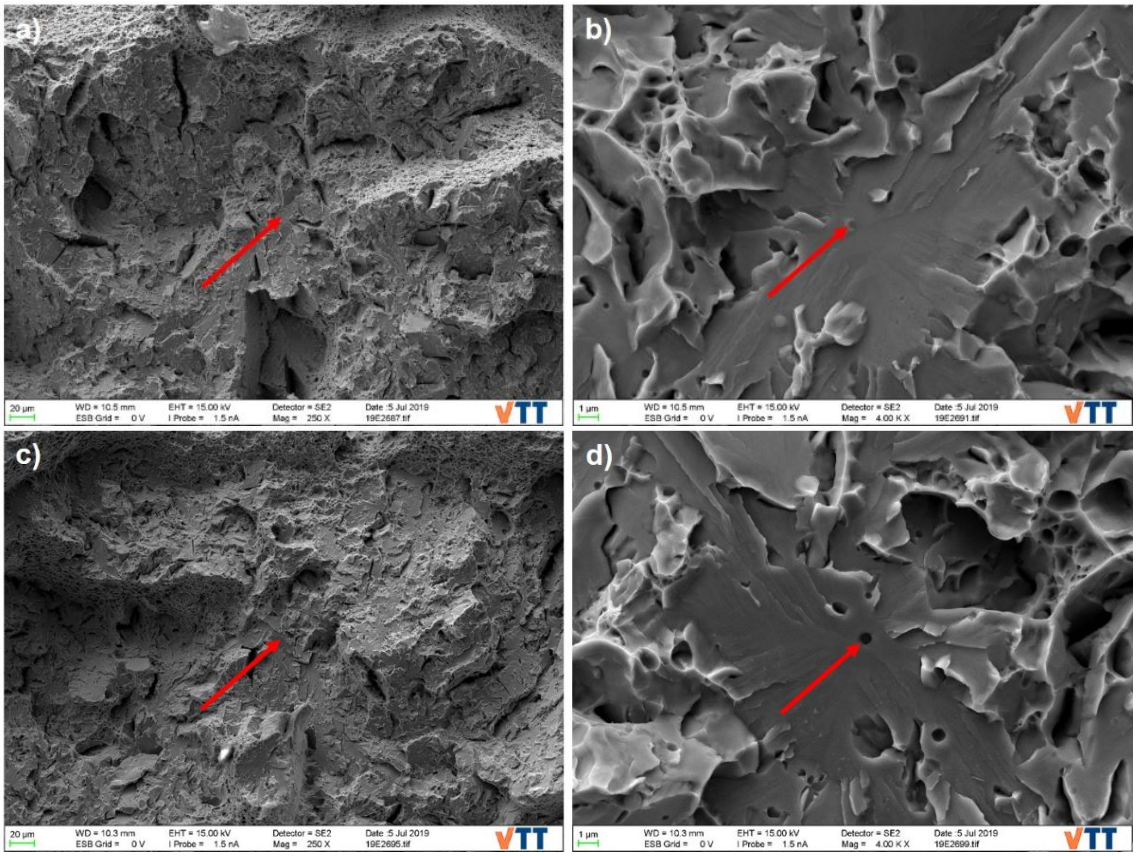

Figure 5.22. *Primary initiation site in the halves of specimen CVN 8 for both (A and B) halves of the specimen.*

halves in the SEM analysis is shown in the micrographs in Figure 5.22. The specimens were investigated in the same orientations as shown in the macrographs in Figure 5.21,

i.e., the notch is always upwards in the images.

From the SEM images, the fracture mode could be determined, showing also that the majority of the surface in the brittle areas failed by cleavage fracture. Between the cleavage fracture areas, some plastic deformation due to local ductile fracture was found interrupting the cleavage crack propagation and making the ligament between the fracture planes to fail by shear [44]. The propagation paths are seen as river patterns typical for the cleavage fracture as they begin from the brittle fracture initiation site. The dimple-like surface of the ductile fracture is seen in the surroundings of the primary initiation site in Figure 5.22. However, the overall fracture mode allows the cleavage fracture to propagate further and initiate secondary fractures. The initiation area was examined using the EDS analysis on both specimen halves. The point analysis with semi-quantitative chemical compositions of the two points per fracture surface is seen in Figure 5.23, and the results of the mapping analysis are in Figures 5.24 and 5.25.

Element	Wt. %
O K	1.0
Al K	0.1
Si K	0.2
Mo L	0.0
S K	0.2
Ti K	0.1
Cr K	0.2
Mn K	1.2
Fe K	95.5
Ni K	1.4
Cu K	0.2

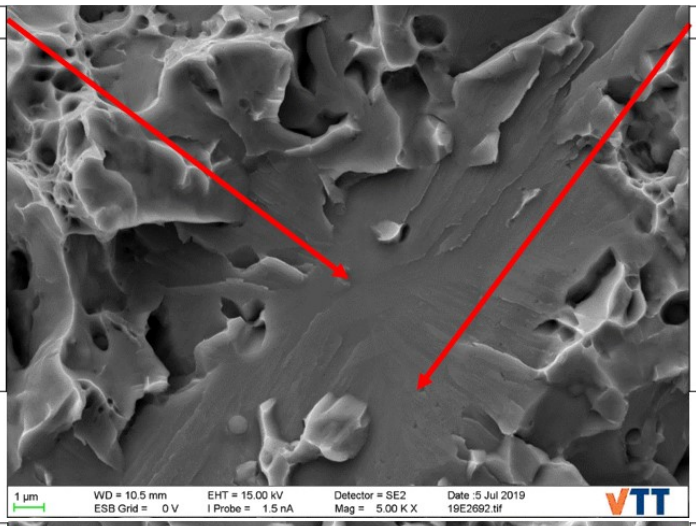

Element	Wt. %
O K	0.0
Al K	0.1
Si K	0.2
Mo L	0.3
S K	0.0
Ti K	0.1
Cr K	0.2
Mn K	1.3
Fe K	96.1
Ni K	1.5
Cu K	0.3

Element	Wt. %
O K	7.4
Mg K	0.1
Al K	5.0
Si K	3.0
Mo L	0.0
S K	0.3
Ti K	0.4
Cr K	0.3
Mn K	12.4
Fe K	70.4
Ni K	0.8
Cu K	0.0

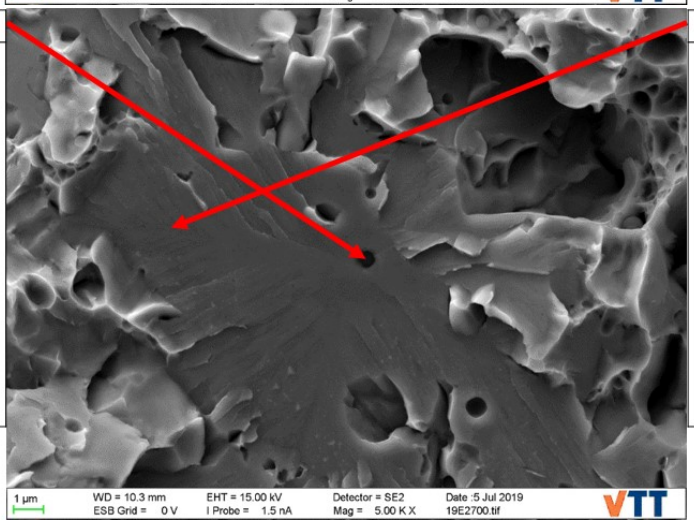

Element	Wt. %
O K	0.0
Mg K	0.0
Al K	0.1
Si K	0.2
Mo L	0.3
S K	0.0
Ti K	0.1
Cr K	0.2
Mn K	1.3
Fe K	96.0
Ni K	1.5
Cu K	0.4

Figure 5.23. *Semi-quantitative chemical compositions (wt%) obtained by EDS point analysis of specimen CVN 8, half A on top and half B on bottom. On the left is shown the composition of the primary initiation site and on the right the composition of the surrounding matrix.*

Only on the specimen half B, a particle is seen at the primary initiation site. The semi-quantitative chemical composition obtained of the particle using EDS shows that the particle is rich in manganese, aluminium, silicon, oxygen, sulphur, and titanium. The elemental mapping analysis supports the point analysis result as the concentration of the detected elements appear brighter at the particle location on the side B. In Figures 5.24 and 5.25 the EDS maps are given for oxygen, aluminium, silicon, manganese, iron, and nickel. The initiating particle appears to be the largest in the region.

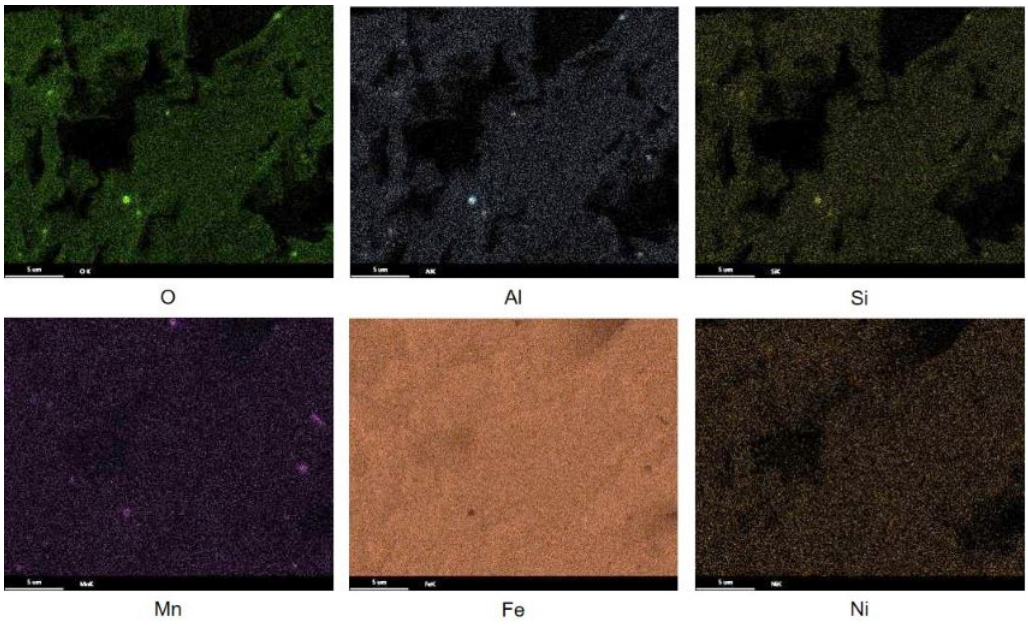

Figure 5.24. *EDS mapping analysis of the specimen CVN 8 A initiation site.*

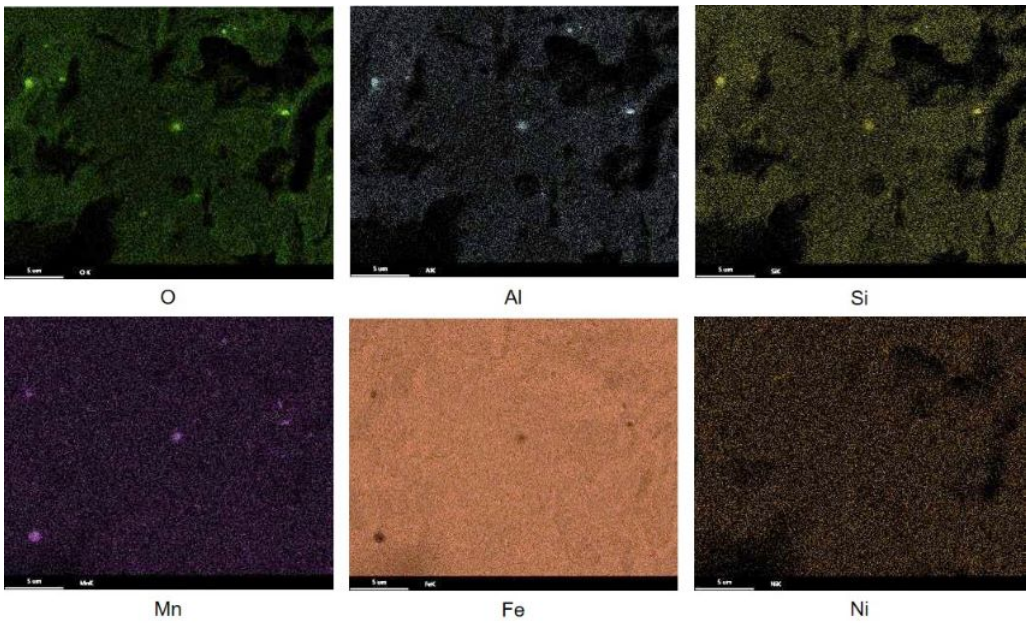

Figure 5.25. *EDS mapping analysis of the specimen CVN 8 B initiation site.*

The cross-sections were prepared from the other half of the specimen as close as possible to the initiation site, and the microstructure of the primary initiation area was examined

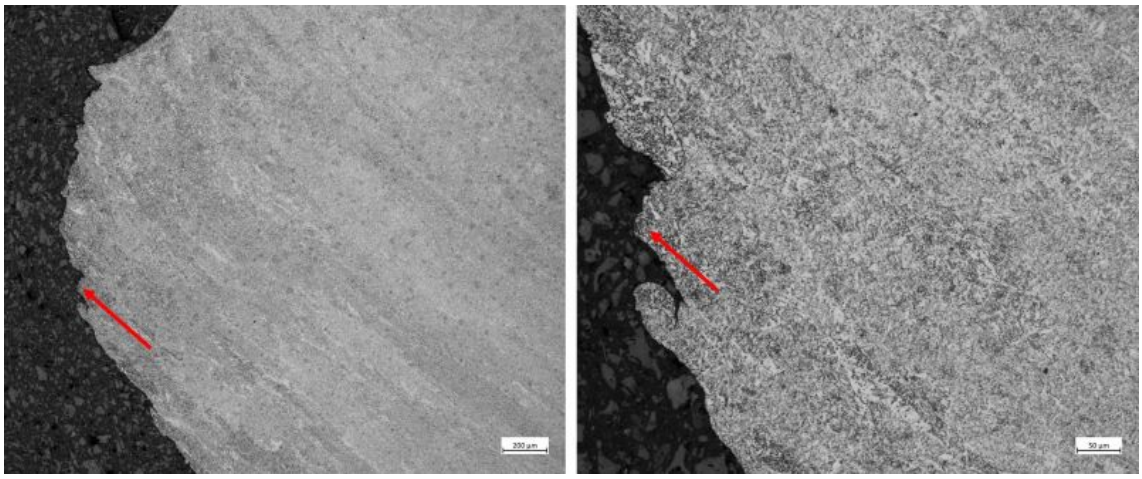

Figure 5.26. *Microstructure of the cross-section specimen CVN 8. The arrows point to the approximate location of the primary initiation site on the fracture surface.*

using the light optical microscope, as shown in Figure 5.26. In the area surrounding the V-notch, the microstructure in all the specimens is as-welded, as the columnar grains of the weld bead can be detected in the etched sample. Hence, the initiation site is in the as-welded microstructure. The corresponding location of the V-notch in the microstructure is simply due to the location of the cut from the trepan and the weld, and the V-notch is always in the middle of the specimen. Since the cross-section is not accurately at the initiation site, the actual location in the as-welded metal cannot be determined with certainty whether the fracture initiates in acicular ferrite or in grain boundary ferrite.

The initiation area was examined using EDS mapping similar to the fracture surface. However, no significant changes in the chemical composition or abnormal microstructural features were found.

Specimen CVN 2B5

Specimen CVN 2B5 was cut from trepan 2 and tested at the temperature of -119.5 °C, giving the impact toughness energy of 10.6 J, which is well in the brittle fracture region and on the lower shelf of the transition curve. The primary initiation site is at the distance of 3.353 mm from the side surface and 0.912 mm from the V-notch. The fracture initiation location on the fracture surface is indicated by the red arrow in the macrographs in Figure 5.27. The SEM images of the primary initiation site in the two halves are shown in Figure 5.28. As the impact toughness energy is so low, the cleavage fracture dominates and larger brittle fracture areas are found on the fracture surface. The river patters can be followed to the primary initiation site, which is identified by the large area of the river patterns and the appearance of the crack propagation directions. Less ductile fracture surface is seen between the cleavage fractures areas in the specimen at the lower shelf than in the specimen from the lower part of the transition curve, i.e., in specimen CVN8.

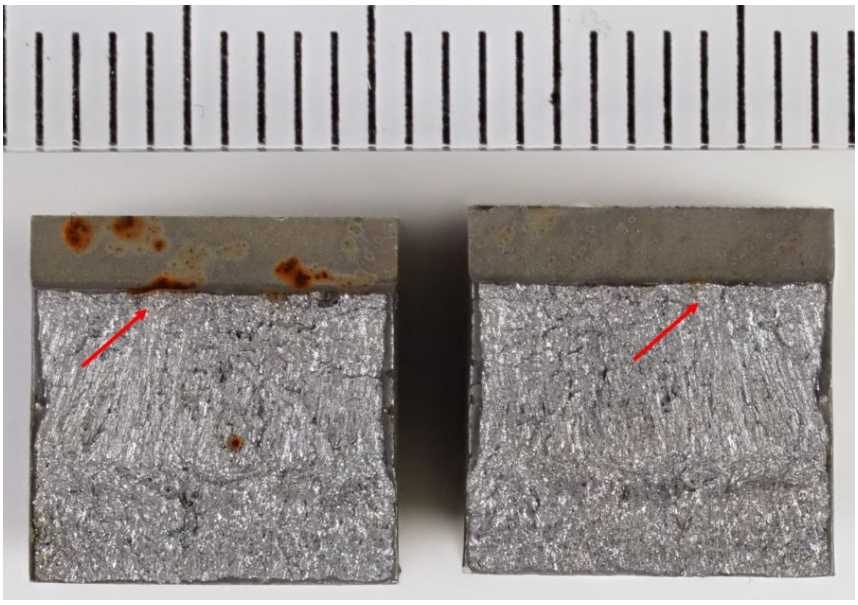

Figure 5.27. *Reprography images of the fracture appearance of specimen CVN 2B5. The primary initiation site is pointed out by arrows in the image. The scale on the top has a line spacing of 1 mm.*

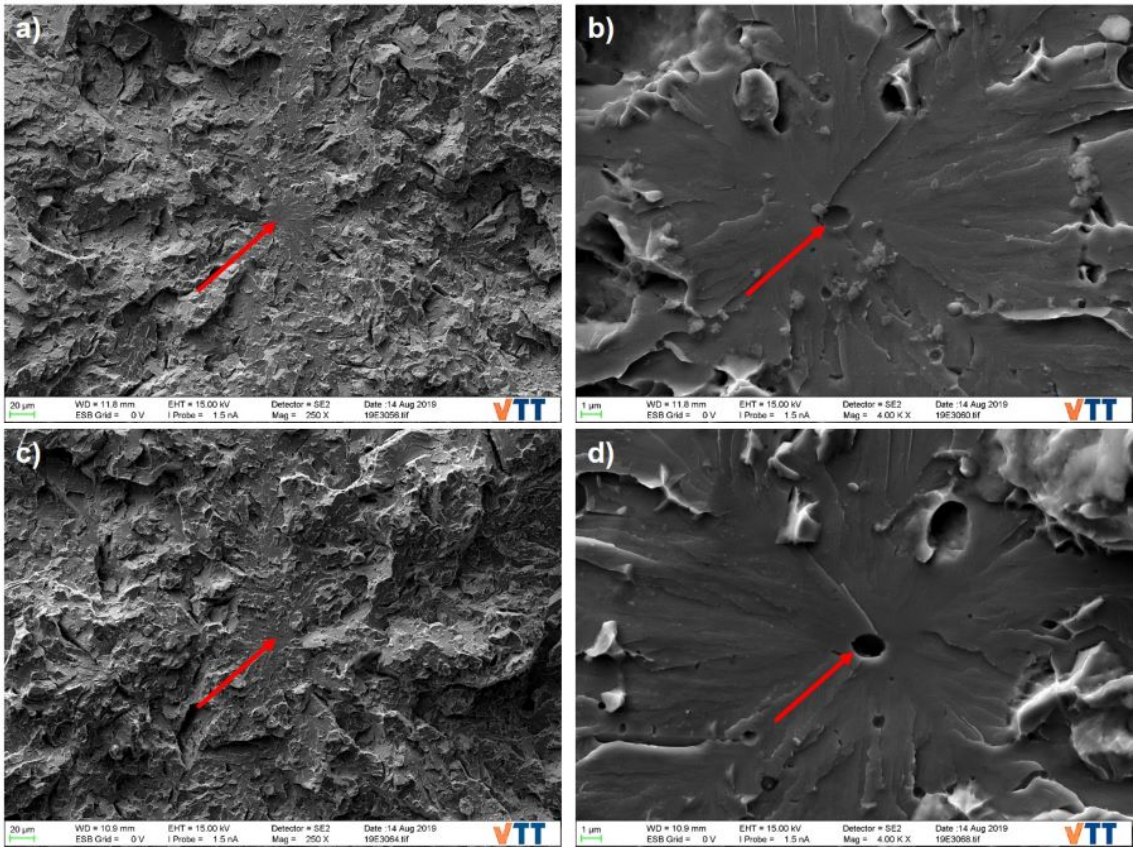

Figure 5.28. *Primary initiation site of specimen CVN 2B5 for both (A and B) halves of the specimen.*

The EDS point analysis with a semi-quantitative chemical composition is given in Figure 5.29 for the selected points, one corresponding to the initiation site and the other to its the surroundings. The EDS elemental maps of both specimen halves are shown in Figures 5.30 and 5.31.

Element	Wt. %
O K	26.1
Mg K	0.4
Al K	13.8
Si K	8.4
Mo L	0.0
S K	0.6
Ti K	0.8
Cr K	0.2
Mn K	23.9
Fe K	25.4
Ni K	0.4
Cu K	0.0

Element	Wt. %
O K	0.0
Mg K	0.0
Al K	0.0
Si K	0.2
Mo L	0.3
S K	0.0
Ti K	0.1
Cr K	0.1
Mn K	1.5
Fe K	95.8
Ni K	1.7
Cu K	0.2

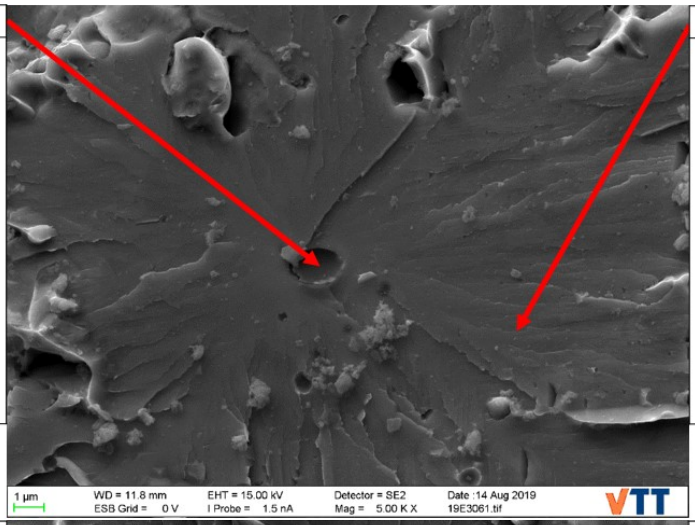

Element	Wt. %
O K	19.3
Mg K	0.4
Al K	11.2
Si K	6.6
Mo L	0.0
S K	0.4
Ti K	0.8
Cr K	0.3
Mn K	19.4
Fe K	40.6
Ni K	0.6
Cu K	0.4

Element	Wt. %
O K	0.0
Mg K	0.0
Al K	0.0
Si K	0.3
Mo L	0.5
S K	0.0
Ti K	0.4
Cr K	0.4
Mn K	1.6
Fe K	94.4
Ni K	1.8
Cu K	0.5

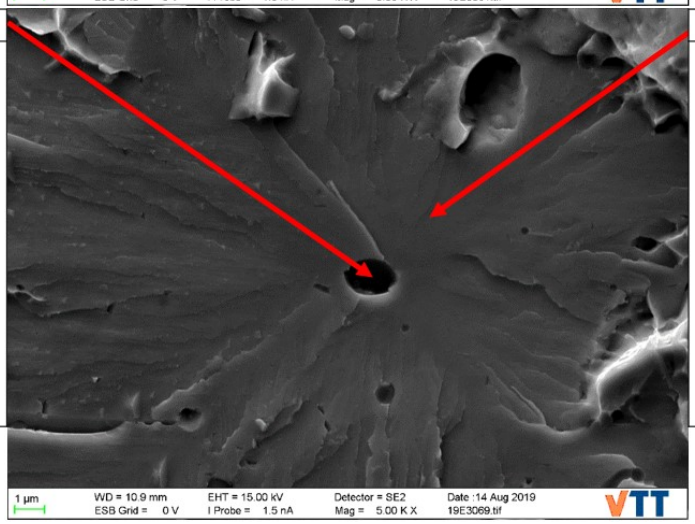

Figure 5.29. *Semi-quantitative chemical compositions (wt%) obtained by EDS point analysis of specimen CVN 2B5, half A on top and half B on bottom. On the left is shown the composition of the primary initiation site and on the right the composition of the surrounding matrix.*

The location of the particle at the primary initiation site is seen on both sides of the specimen, and remains of its elements are also found from both surfaces. The semi-quantitative chemical composition was determined for the particle, revealing that it is rich in manganese, aluminium, silicon, sulphur, oxygen, titanium, and magnesium. The EDS mapping analysis verifies the results of the point analysis. As in specimen CVN 8, the initiating particle appears to be the largest in the region.

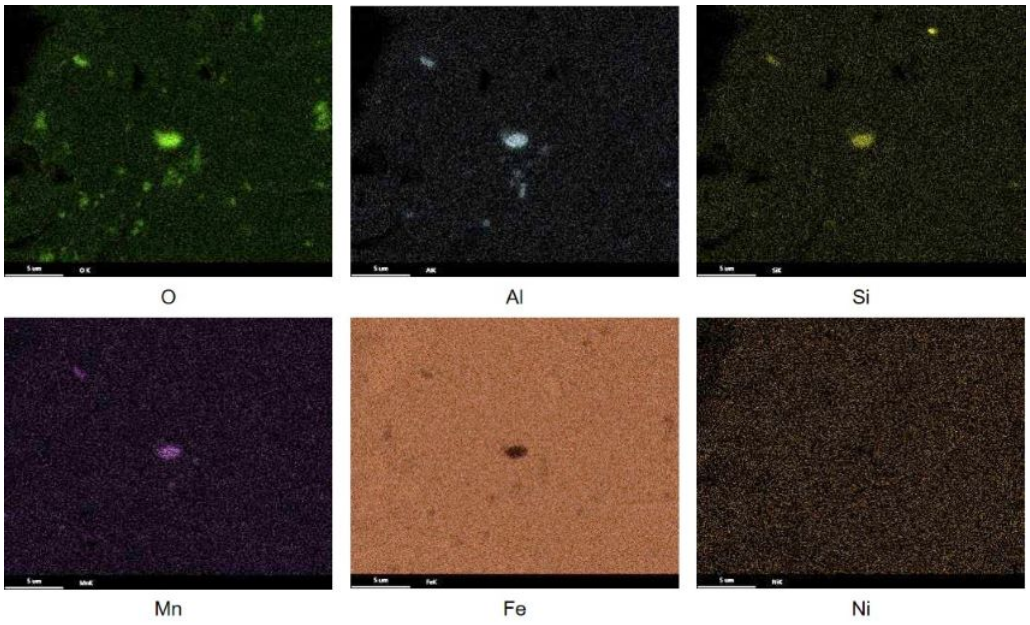

Figure 5.30. *EDS mapping analysis of the specimen CVN 2B5 A initiation site.*

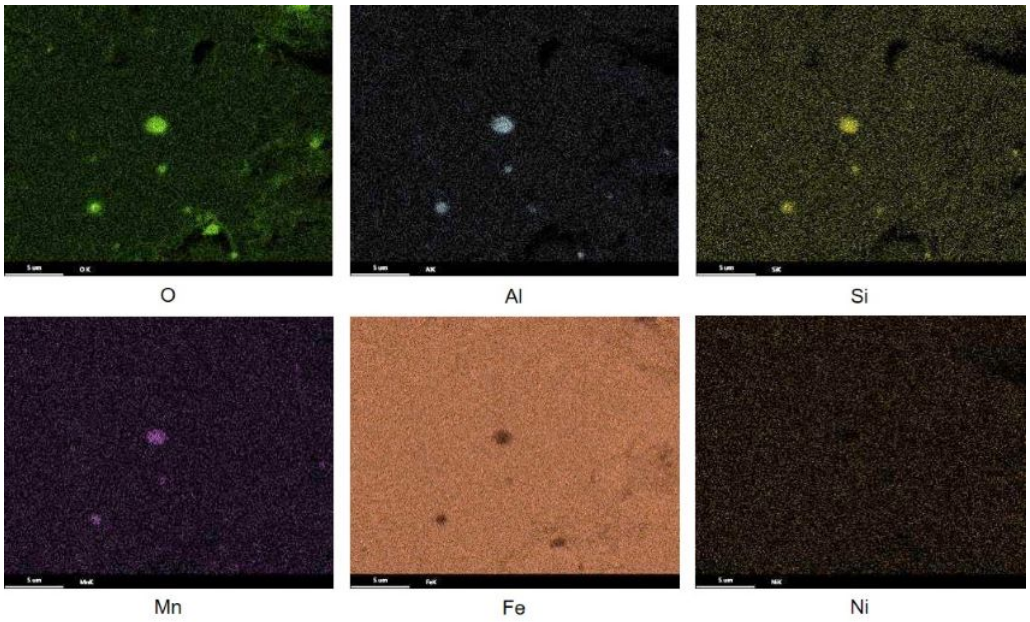

Figure 5.31. *EDS mapping analysis of the specimen CVN 2B5 B initiation site.*

The light optical micrographs of the cross-section close to the fracture initiation site were prepared. The microstructure of the fracture area is shown in Figure 5.32, where the initiation site is pointed out with a red arrow. The image on the left shows a larger area near the V-notch where the microstructure changes from reheated to as-welded, and the actual primary initiation site is located at the as-welded microstructure. In the higher magnification in the figure on right, the as-welded microstructure is clearer.

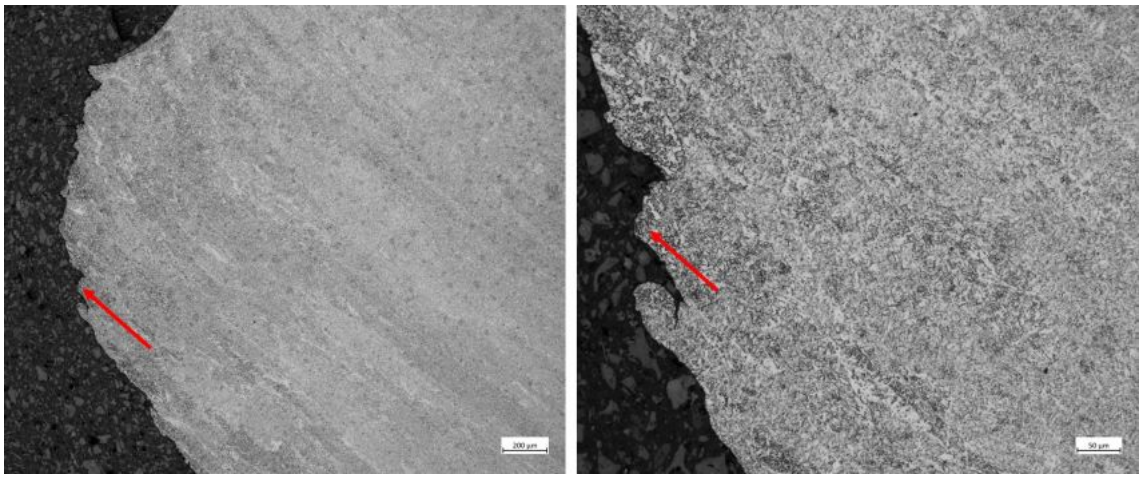

Figure 5.32. *Microstructure of the cross-section specimen CVN 2B5. The arrows point to the approximate location of the primary initiation site on the fracture surface.*

The EDS mapping for the cross-section microstructure and initiation site did not show any unusual features in the chemical composition.

5.2.3 Secondary Particles

The analysis of secondary particles was limited to inclusions within the weld metal. The inclusions were analysed separately in the as-welded and reheated regions. The inclusions were detected automatically by setting thersholds to the image brightness histogram [60]. Examples of an analysed field of the as-welded and reheated regions are seen in Figures 5.33 and 5.34. In the left hand side SEM image the dots have darker pixels than thresholds and therefore are identified as inclusions. On the right side the recognised inclusions are shown in red colour. In the analysis, also the geometry of the inclusions was analysed including aspect ratio, area, and diameter.

In Table 5.3, the average results are compared between the as-welded and reheated microstructures. It is evident that there is approximately 1.5 times more inclusions in the as-welded region than in the reheated region, according to the inclusion density parts per mm^2. Additionally, the average size is slightly smaller in the as-welded region with 0.288 μm versus 0.325 μm in reheated region. For the as-welded region, there are in total 1339 inclusions within eight fields and in the reheated region there are 960 inclusions within nine fields. The average amount of inclusions per field are 167 and 107 parts for the as-welded and reheated regions, respectively. However, statistically, the most probable inclusion size for the as-welded region is 0.23 μm and 0.27 μm for that in the reheated region. Furthermore, the aspect ratio of all measured particles is close to one indicating that the inclusions are mostly roundish. Additional details of the size distribution are given in the Appendix B.

The elemental analysis was performed during the particle recognition from the centroid

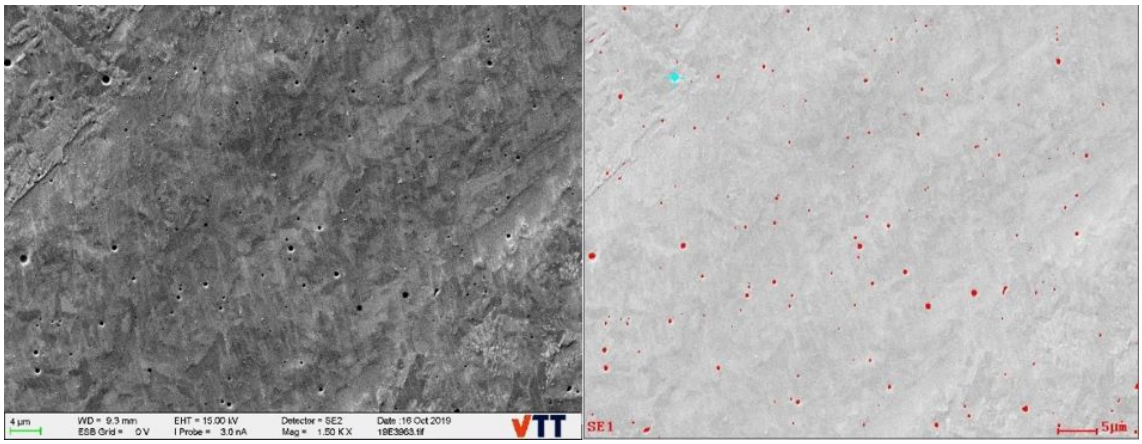

Figure 5.33. *A field from the as-welded region [60]. On the left is a SEM image and the right shows the inclusions in red colour.*

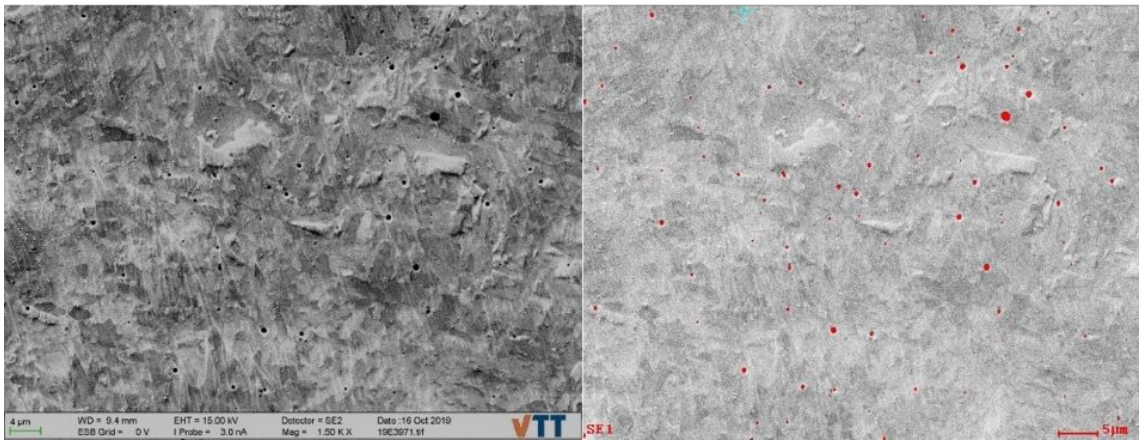

Figure 5.34. *A field from the reheated region [60]. The left is a SEM image and the right shows the inclusions in red colour.*

Table 5.3. *Inclusion size distributions per microstructure. Analysis of as-welded region included 8 areas and reheated region 9 areas.*

Region	Avg.Diam. (μm)	Counts per field	Density (Part mm^{-2})
As-welded	0.288	167	40805
Reheated	0.325	107	25995

of the particles. The EDS spectrum of all the inclusions in the as-welded and reheated regions give similar chemical compositions for the inclusions in both microstructures. The main elements detected were iron, manganese, and oxygen with smaller fractions of aluminium, silicon, and sulphur. The high peak of iron in the spectrum signals is due to the signals collected from the matrix. The average chemical compositions are listed in Table 5.4. Trace elements such as carbon, sodium, phosphorus, calcium, and titanium, with weak peaks in the spectrum were observed, however, excluded from the element list since the main elements have been confirmed in the previous EDS analyses.

Table 5.4. *Average composition of an inclusion from elemental analysis for as-welded and reheated regions.*

Element	As-welded wt%	Reheated wt%
Fe	85.13	80.85
Mn	6.13	7.87
Al	2.96	4.33
Si	1.81	1.78
O	3.42	4.45
S	0.55	0.72

Concluding the chemical composition, iron, manganese, aluminium, and silicon are capable of forming sulphides and oxides [43]. The size of an oxide particle increases with the oxygen concentration. On the other hand, manganese and iron form sulphides and are present in the microstructure. However, the amount of sulphide particles is an order of magnitude lower than the amount of the pure oxide inclusions. Hence, the inclusions in the investigated weld metal are mainly complex iron-manganese-aluminium oxides, and there are inclusions that contain silicon and are free of silicon. In those inclusions without silicon, the manganese and aluminium concentrations are ca. 40 wt% and ca. 30 wt%, respectively.

5.3 Microhardness

After the microscopical characterisation, the cross-section specimens were polished again for microhardness measurements. A hardness matrix with 100 data points seen in Figure 5.35, containing 20 indentations every 0.3 mm in five rows on a spacing of 0.5 mm. The first row started at 2 mm below the V-notch. The hardness matrix was obtained on every tested specimen. The microhardness measurements were aimed to obtain the microhardness of the different microstructural regions. The specimens included in the microhardness measurements were CVN 9, 10, 11, 2B5, 2B7, 2B10, and 2B11. All specimens were measured in a similar manner.

After the measurements, the specimen surface was carefully etched and the indentation area was observed using an optical microscope. The different microstructural features could be identified and connected to the obtained microhardness values. An example of the microstructure and hardness measurements is seen in Figure 5.35, where the coloured lines follow the weld beads and the thermal cycle effects on the microstructure. Since the fracture surface locates in the middle of the weld joint, the metal has been subjected to multiple thermal cycles. In the microhardness evaluation, the microstructure is divided into as-welded, partially reheated, (once) reheated and twice reheated microstructures. The microhardness matrices of the seven samples and in total 700 data

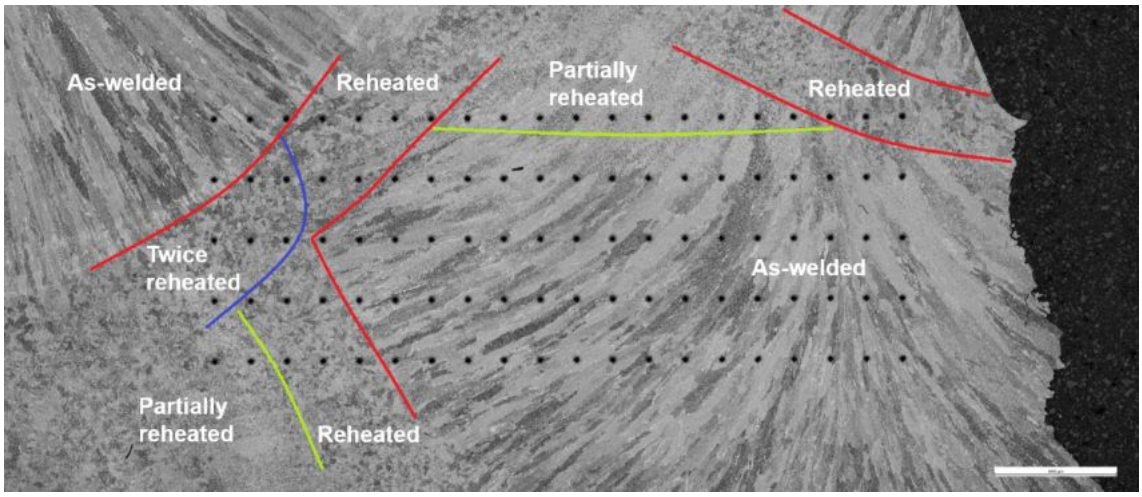

Figure 5.35. *Microhardness measurements on the cross-section specimen CVN 2B10. The microstructural features are separated in the figure for further analysis.*

Table 5.5. *Microhardness HV0.3 results of all the specimens based on the microstructural features.*

Microstructure	Average HV0.3
As-welded	214±8
Partially reheated	210±6
Reheated	216±8
Twice reheated	218±10
All	215±8

points were accordingly divided and summarised. The results are shown in Table 5.5.

The microhardness results are typical for the weld metal and no significant differences in the hardnesses is seen between the microstructural regions. Although the hardness of the partially reheated region appears the lowest on average, it is still within the variation of the other regions. In principle, the hardness of the partially reheated region can be slightly lower due to thermal softening. However, the twice reheated region has the highest hardness after multiple thermal cycles, which may be due to carbon diffusion. Still, there are no differences in the hardness between the as-welded and reheated microstructures, as was earlier concluded in conjunction of the macrohardness measurements presented in Section 5.1. Comparing to the baseline data available, where the average microhardness of the weld is 208 HV0.3, no indications of significant effect from RPV operation is observed [63].

6 DISCUSSION

The main objective of this thesis is to investigate the effect of the weld microstructure on the brittle fracture behaviour in the decommissioned Barsebäck 2 boiling water reactor pressure vessel weld metal after 23 years of effective operation. Two paths in characterising the causes of the weld embrittlement were used in the work that are connected, i.e., the microstructure characterisation and mechanical testing, which further is divided into hardness and impact toughness. First, the weld microstructure features were determined and the chemical composition obtained to gain fundamental knowledge of the investigated weld metals. Second, the hardness was used to describe the mechanical properties of the material, and third, the impact toughness test results and fracture characteristics were evaluated. Based on the obtained results, the following conclusions can be drawn.

6.1 General Microstructure

The weld microstructure was characterised from the base materials to the HAZ and to the multipass weld. The characterised weld joint, with a wall thickness of about 74 mm, is located in the head of the RPV, where the base material on the top is a forging, and a plate on the bottom. Both sides of the weld joint were investigated. The hardness profiles across the weld fusion line were plotted for both base materials, and some differences in the hardness were seen for the base materials, the forging being 16 HV10 softer than the plate with an average hardness of 194 ± 7 HV10. However, the small difference between the base materials at HV1 is considered typical, and the hardnesses of the HAZ showed no differences. In addition to the two base materials, two welding methods had been employed during welding. The inner wall side was welded with the submerged arc welding and stretched up to 16 mm from the outer surface, which had been welded with the manual metal arc welding method. Differences in the weld microstructure were found due to the differences in the chemical composition and heat input. Generally, according to the macrohardness measurements and microscopy investigation, the weld is homogeneous throughout the weld build-up thickness and of good quality.

The features of the heat-affected zones are typical for the SA 533 Grade B Class 1 and SA 508 Class 2 base materials, and the welding heat inputs used in the present study. The dominating phase is bainite and the microstructures of the fine- and coarse-grained HAZ are as expected. The width of the HAZ is consistent throughout the weld. In the mi-

crostructure characterisation with LOM, only individual grains of martensite, yet no large areas of it, are found in the coarse-grained HAZ of the SAW weld. In comparison, in the coarse-grained HAZ of the MMA welded microstructure, locally larger areas of martensite are found, although still sub-millimetre in size. However, such small amounts of martensite do not cause evident embrittlement in the material. According to the hardness measurements, there are no high hardness peaks typical for untempered martensite, or the hardened grains may have been thermally softened and relaxed during the 23 years of RPV operation at 288 °C. A typical hardness for martensite in this type of material would be 340–400 HV. However, in both macro- and microhardness measurements the results remain below 300 HV. Above ca. 340 HV the hydrogen embrittlement must be taken into account in these materials.

The hardness is higher in the heat-affected zone adjacent to the fusion line compared to the base material and the weld metal due to the austenitisation and the quenched microstructure at cooling and the carbon diffusion. However, the hardness profile measured from the base material over the HAZ to the weld metal is typical, and the variation in the hardness is caused by local inhomogeneties and hardened areas in the microstructure. In the general characterisation, ghost lines that are known to have carbon and certain alloying element segregations are found, which typically result in higher hardenability.

At the fusion boundary, epitaxial growth from the solid heat-affected zone to the fusion zone is found, which is typical for welding microstructure. The weld beads of as-welded microstructure showed clear columnar grain structure growing towards the centre of the weld pool. Throughout the weld, the as-welded microstructure is dominated by acicular ferrite. The high nickel and manganese concentration in the weld metal, additional to the non-metallic inclusions, promote the initiation and formation of acicular ferrite. Between the columns, light-coloured areas of pro-eutectoid grain boundary ferrite is found, which is also typical although not as favourable as acicular ferrite due to easy crack propagation along the long grain boundary phase. In low-carbon weld metal, the growth kinetics of Widmanstätten ferrite formation is relatively low. Widmanstätten ferrite is not observed using LOM in the SAW weld, and in the MMA welded microstructure, only a few lath-like structures are seen with the grain boundary ferrite. Due to the low sulphur and phosphorus concentrations, it is considered unlikely that significant high-temperature induced segregations at the grain boundaries would have occurred.

In a multipass weld, the next weld pass and multiple thermal cycles are seen on top of the previous weld, making the weld microstructure complex. Every new weld bead has caused a high thermal effect on the columnar grains of the previous weld bead and therefore have formed the reheated microstructure with the refined grain size within ca. 1 mm wide region in the weld bead. In the middle, several weld passes overlap, hence the previous solidified weld metal is subjected to several thermal cycles. In the reheated microstructure, polygonal ferrite dominates although acicular ferrite and grain boundary ferrite remain, too. The change in the microstructure does not have a significant effect on the toughness properties of the weld. The amount of polygonal ferrite is found to increase

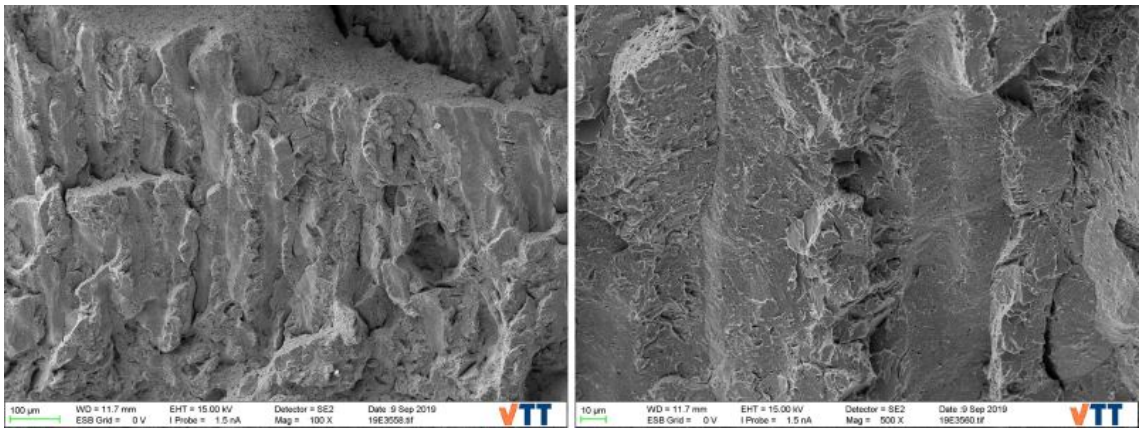

Figure 6.1. *Interdendritic and intergranular fracture in the as-welded microstructure of a brittle fracture specimen.*

with the number of thermal cycles, as the microstructure becomes more affected.

In the microstructure characterisation of the cross-sections of the CVN specimens from the lower shelf area, the fracture occurred in the as-welded microstructure dominating the region around the V-notch in all investigated specimens. Brittle fracture initiated at a secondary particle in all investigated specimens. Brittle fracture initiation is dependent on the crack driving force, which in turn is dependent on e.g. local stress intensity and constraint [64]. The fracture initiation can also be dependent on the particle size and distribution near the location of the maximum crack driving force. The crack propagation, however, is more dependent on the surrounding grain structure and strain state than on the particle distribution. This is because several microcracks may occur in brittle particles, but if the stress is not high enough to break the matrix, the crack is arrested [32].

In addition to the major fracture modes of cleavage, shear, and ductile fracture, intergranular and interdendritic fractures were found in the scanning electron microscopy investigation, as seen in Figure 6.1. Larger regions of the interdendritic-like fracture were found in the fully brittle specimens, but a small area with a similar appearance was also detected in a fracture surface that was otherwise fully ductile. Intergranular fracture mode has also been found in the fractography of SA 533 base material before and after the material has been thermally aged [21]. The amount of interdendritic fracture in the fracture appearance has been shown to be connected to the thermal ageing induced embrittlement [25]. Furthermore, these fracture modes refer obviously to the easiest path of crack propagation along the grain boundary ferrite. However, the fracture surface is not fully brittle, and minor traces of ductile fracture and deformation can be seen.

6.2 Impact Toughness

In the mechanical testing part, thermal ageing and brittle fracture of the weld metal were characterised by the standardised Charpy V-notch impact toughness test. The full transition curve is seen in Figure 6.2, where the orange curve represents the produced data

in the BRUTE project [65]. T2 and T3 refer to trepans 2 and 3, respectively. The red box in the lower part of the curve includes the T2 and T3 data points used in the characterisation of brittle fracture in this work. In comparison, the purple curve represents the baseline data from a Barsebäck 2 surveillance program carried out by Studsvik in 1991 on non-irradiated material.

Since the impact toughness testing is designed to predict e.g. impact of the thermal loading in the metal, a thermal ageing effect should be seen as a shift in the ductile-to-brittle transition temperature towards higher temperatures. However, according to the data available, there is no shift in the transition temperature. The lower shelf region of the transition curve has remained intact, which indicates that the temperature in RPV operation has not affected the brittle fracture behaviour of the weld metal. In Figure 6.2, ΔUS refers to the upper shelf that has decreased by -27 J, as seen in the curves. ΔT_{50} = -9 °C and ΔT_{41} = -2 °C are the shifts in temperature at 50 J and 41 J, respectively. The shifts are so small that they are statistically within the deviation and do not necessarily indicate any real shift in the transition temperature [65].

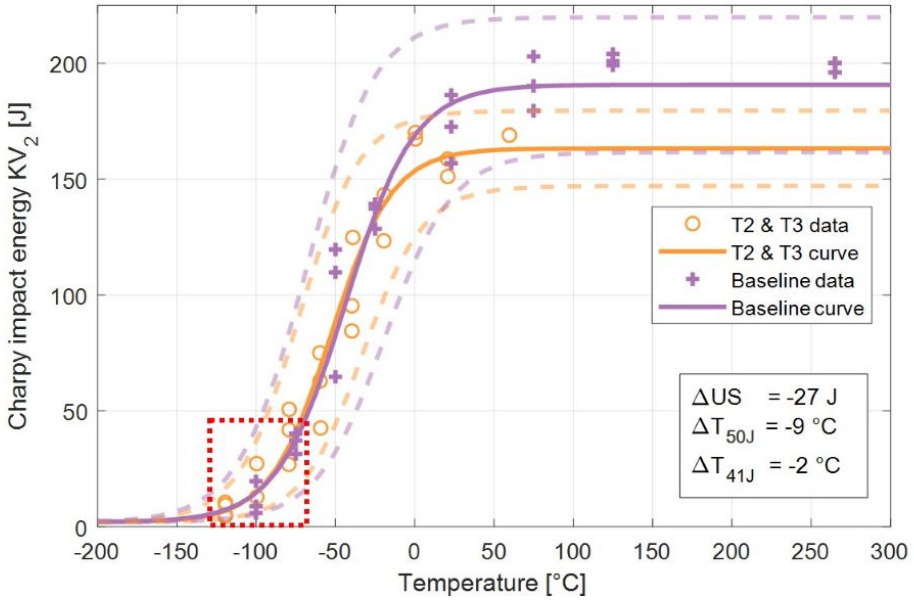

Figure 6.2. *Transition curves from the experiments on T2 and T3 (trepan 2 and trepan 3) with a comparison to the baseline curve obtained in a surveillance program. The red box contains the data points used in the brittle fracture characterisation.*

In the study of Joly et al. [25], the welds of a pressurizer with the same type of weld metal on SA 533 Grade B Class 1 RPV were aged for ca. 27 years at 350 °C, and the material experienced a shift of +100 °C in the transition temperature. The conclusion that can be made is that the thermal ageing kinetics, i.e., time and temperature, is such that 23 years at 288 °C is not enough for thermal ageing to affect the transition temperature of the weld metal in question. The study by Druce et al. [21] showed for the similar base material that there is virtually no effect of thermal ageing at 300 °C in the transition temperature, but a large shift was seen after artificial ageing at 400–550 °C up to 2 $\times 10^4$ hours.

6.3 Microstructure Effect on Brittle Fracture Initiation

The fractography on all nine investigated CVN samples concluded that the leading fracture mode is transgranular cleavage fracture, and the river patterns could be followed to the primary initiation site. Ductile fracture and mild deformation could be seen locally in specimens corresponding to the lower part of the transition curve. Consistently in all the specimens, a particle was found at the primary initiation site. The particles of the specimens CVN 9 and CVN 2B7 are shown in Figure 6.3. The particle remained usually on one half of the fracture surface, but the location could be seen also on the other half as a dent and traces of the particle could be found. This shows the importance of performing fractography on both sides of the specimen halves and not, as usually, only on one of them. An EDS analysis gave the particles an approximate composition with Mn, S, Al, Mg, Si, Ti, Cu, and O, as tabulated in Table 6.1. The main elements are manganese, aluminium, and silicon, which are alloying elements in the steel weld which form oxides and sulphides. Also traces of titanium and copper are from the alloying, but the magnesium in the detected particles may be a residue from the welding process. The size of the particles is approximately 0.5–2.5 μm, as determined from the fracture surface. Delamination of the particle from the matrix is also observed.

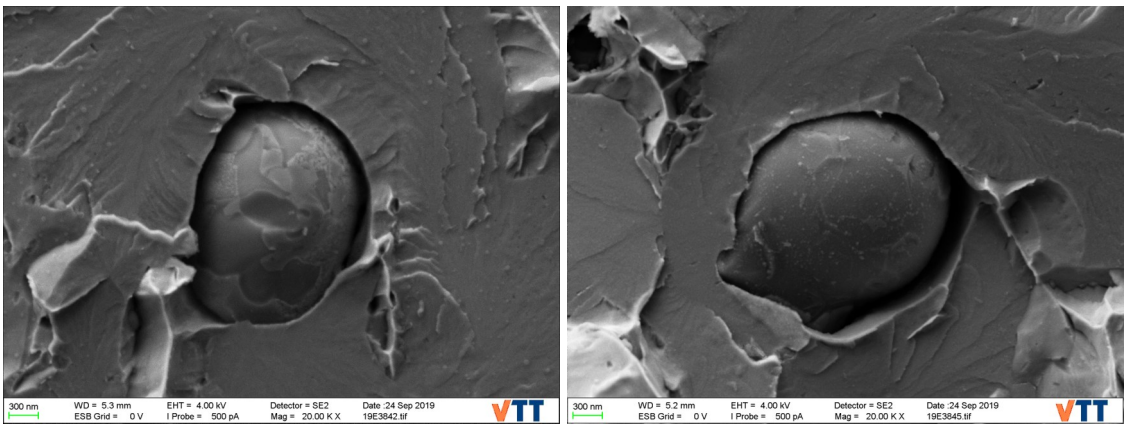

Figure 6.3. *Particle at the primary initiation site in specimens CVN 9 and CVN 2B7. The particle sizes in this case are approximately 1.5 μm and 2.5 μm, respectively.*

According to the EDS analysis, the particles at the primary crack initiation sites are oxides, which are brittle and fulfil the Griffith criterion for brittle fracture initiation. In comparison, the manganese sulphide particles that were found in the base material using an optical microscope are ductile particles and can deform under mechanical loading. Neutron embrittlement causes changes in the microstructure, mainly the formation of nickel- and manganese-rich solute clusters and segregation [66]. Both of these change the plastic properties of the material, and may affect also the brittle fracture initiation [66, 67]. However, the weld under investigation is not irradiated but only thermally affected. Further investigations will be performed on the weld metal taken from the irradiated belt-line weld. The results from these investigations will show, if neutron embrittlement changes the brittle fracture initiation behaviour.

Table 6.1. *Semi-quantitative chemical composition in weight percentage of all initiating particles obtained with EDS. Elements such as Fe, Cr, and Ni are due to the base material and have been omitted from the results.*

Specimen	Mn wt%	S wt%	Al wt%	Mg wt%	Si wt%	Ti wt%	Cu wt%	O wt%
CVN 8	12.4	0.3	5.0	0.1	3.0	0.4	–	7.4
CVN 9	23.7	0.3	18.8	1.1	8.5	0.8	0.2	33.8
CVN 10	23.2	0.4	13.2	0.9	7.4	0.8	–	21.9
CVN 11	4.8	1.3	2.3	0.4	1.5	0.2	2.6	4.6
CVN 12	17.0	0.3	14.3	1.0	7.6	0.6	–	28.9
CVN 2B5	24.0	0.6	13.9	0.4	8.4	0.8	–	25.9
CVN 2B7	25.7	0.5	19.9	1.4	8.4	1.1	0.6	30.1
CVN 2B10	16.0	0.8	12.3	0.8	6.6	0.6	2.6	19.2
CVN 2B11	21.8	0.3	14.7	1.0	8.6	0.8	–	26.7

The microstructure effect on the brittle fracture is demonstrated in the charts shown in Figure 6.4 plotted from the fractography results. In the top left chart, the particle size (μm) is plotted against the impact energy (J), showing that the bigger the particle, the lower the required energy, or the smaller the particle, the higher the impact energy. To highlight this observation, two specimens, CVN 10 and 11, for which the testing parameters were 12.8 J at -99.6 °C and 27.3 J at -99.7 °C, respectively, are compared in the charts. The effect of the particle size on the impact energy is demonstrated in the charts when the testing temperature is the same for both specimens. The result is logical and explained by the classical theory of brittle fracture mechanics, where a second phase particle cracks due to plastic strain in the surrounding matrix and the microcrack acts according to the Griffith crack theory [32].

During impact loading, at some distance away from the V-notch in front of the crack and within the formed plastic zone, the cleavage fracture initiates at the weakest link near the location of the maximum crack driving force, which is the largest particle in the region [44]. Within the plastic zone, there are particles with a more or less random distribution. In Figure 6.4, the chart on the top right shows that impact energy increases with the initiation distance. Therefore, also the size of the particle depends on the distance, as the larger particles result in crack initiation at a smaller distance from the V-notch, in addition to lower impact energy values. This is also shown in the bottom left chart. Furthermore, the bottom right chart shows how the initiation sites locate in the centre of the fracture surface and not on the sides. This is due to the triaxial stress state and the shape of the stress field forming in impact loading, where the maximum tensile stress of the opening mode is in the middle while further in the sides, the loading changes to the secondary shear fracture mode [44].

The secondary particles and inclusions found in the weld metal are typical and expected in submerged arc welds of low-alloyed steel. The size distribution of the inclusions has

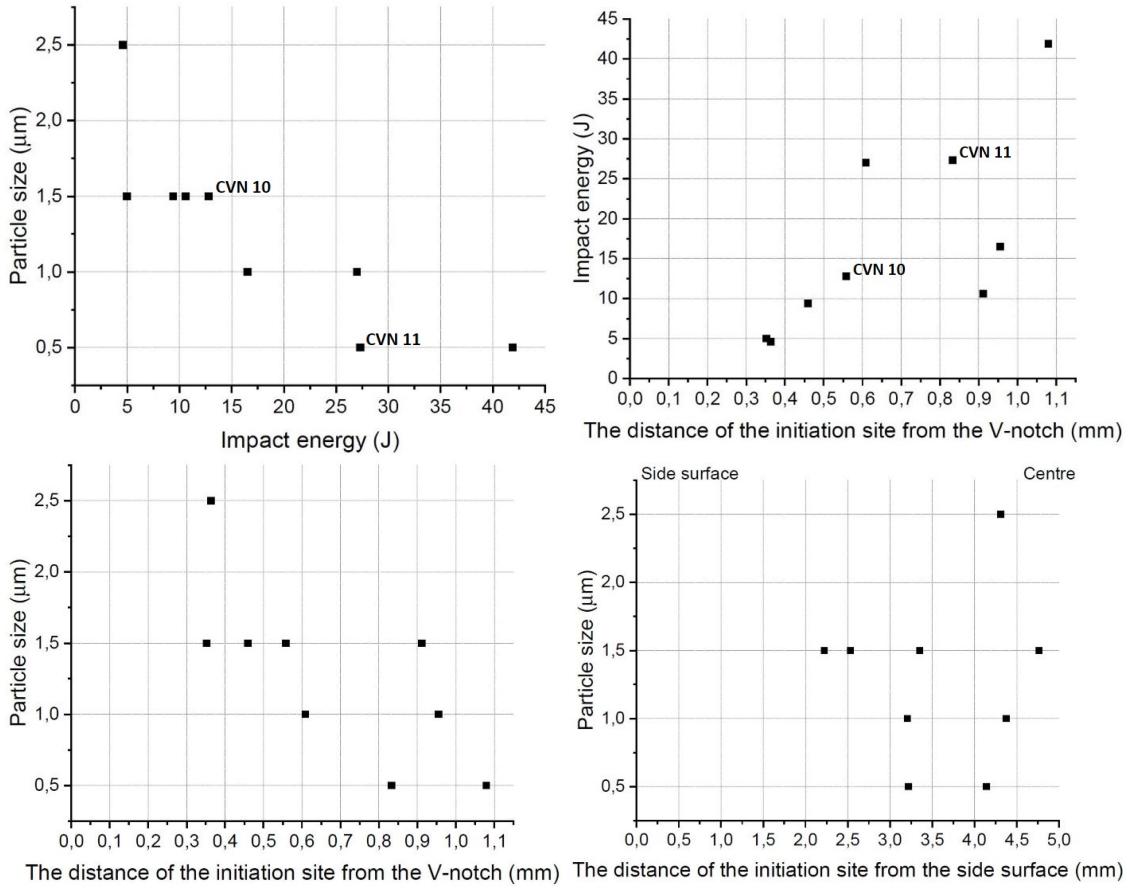

Figure 6.4. *Particle size plotted with impact energy, distance from the V-notch, and distance from the side surface. The impact energy is also plotted with the distance from the V-notch.*

been analysed in a reference study made in a previous project on the same weld. However, the previous inclusion analysis was made using a scanning transmission electron microscopy (STEM) and X-ray spectroscopy, where the magnification is higher than on SEM, which was used in the thesis. The inclusion analysis performed on the investigated weld metal concluded that the inclusion density in the as-welded microstructure is approximately 1.5 times higher than that for the reheated microstructure. Also, the average inclusion size is slightly smaller in the as-welded microstructure. The most typical inclusion sizes are 0.23 μm and 0.27 μm for the as-welded and reheated regions, respectively, following the most typical inclusion area less than 0.05 μm^2 and 0.23 μm^2 for the as-welded and reheated regions. The aspect ratio of all the measured particles is close to one, indicating round-shaped inclusions. Further observations concluded that the inclusion particles were found mainly in the high-angle grain boundaries and have chemical composition mainly of iron, manganese, aluminium, silicon, sulphur and oxygen. Both oxides and sulphides are observed in the as-welded and reheated regions, however, significant majority of the inclusions are Fe-Mn-Al-rich oxides. Hence, the results from the EDS analysis in Table 6.1 can be generally confirmed. Furthermore, comparing to the average inclusion size distribution in the weld metal, the crack initiation has started from very large particles.

Regarding the weld microstructure, the dominating phase in the as-welded microstructure is acicular ferrite and in the reheated polygonal ferrite. The acicular ferrite nucleation tend to be promoted by non-metallic inclusions. Typically, single-phase inclusions, such as some oxides and some sulphides cannot nucleate acicular ferrite, whereas complex inclusions, such as oxy-sulphides and multi-phase inclusions, actively nucleate acicular ferrite [68]. Since a mechanism for acicular ferrite to nucleate is dependent on the surface area of the inclusions, therefore intermediate sized inclusions or small inclusions on a higher density promote effectively the acicular ferrite nucleation [43]. However, often non-metallic oxide inclusions are considered detrimental to the toughness properties, therefore the size and density must be limited. The brittle oxide inclusions also enhance the cleavage fracture nucleation [5].

The effects of thermal ageing and irradiation on the embrittlement of RPV metals have been under research for decades. As there are several different parameters that affect the result, such as temperature, dose, chemical composition, and operation time, there are still many open questions [22, 25, 26, 30, 66, 69]. This thesis provides a comprehensive investigation of the brittle fracture characterisation on the thermally aged weld microstructure of Barsebäck 2 reactor pressure vessel. However, a larger number of specimens of the brittle fracture surfaces is required for confirming the location, particle type, and microstructure of the brittle fracture initiation conclusively. Additionally, it is suggested to investigate further the thermal ageing effect at 288 °C and above, as well as the occurrence of interdendritic fractures also in the ductile fracture regime. Furthermore, different research techniques would also be beneficial such as electron backscatter diffraction (EBSD) for the microstructure and texture characterisation, and focused ion beam (FIB) for preparing specimens of the primary initiation sites for nanoscale TEM analysis. These are, however, out of the scope of this master thesis. Furthermore, a similar study is planned for irradiated weld metal from the belt-line weld of the Barsebäck 2 RPV, where the effect of irradiation on the brittle fracture initiation will be investigated and compared to the non-irradiated material. However, this thesis has shown a correlation between the macroscopic microstructure and the brittle fracture initiation, which is an important observation and underlines the importance of performing thorough investigations all the way from the macroscale down to the nanoscale.

7 CONCLUSION

The investigations included in this thesis are part of the BRUTE project and the all experiments have been performed at VTT Technical Research Centre of Finland Ltd in Espoo, Finland. The specimens are from a decommissioned nuclear power plant Barsebäck unit 2 reactor pressure vessel head weld. The trepans have been cut at the weld joint with forging on the upper side and plate on the bottom side. The weld metal is thermally aged at 288 °C for 23 effective years of operation but has not been subjected to neutron irradiation. In this work, the weld joint has been characterised in terms of its microstructure and brittle fracture mechanisms.

In the beginning, the basic material properties were determined by macrohardness measurements using loads of 10 kgf and 1 kgf. Hardness profiles were plotted according to the measurements from the base materials to the HAZ and to the weld metal. The results concluded that there is no significant differences between the plate and forging base materials but they are slightly softer compared to the weld metal. The highest hardness is obtained at the coarse-grained HAZ right next to the fusion line, where it readily drops towards the base material. Generally, according to the macrohardness, the material is homogeneous and of a good quality. Further, the microhardnesses measured with 300 gf load showed that no differences are seen within the weld metal, i.e., between the as-welded and reheated microstructures.

The microstructure of the base material and fine-grained HAZ is bainitic steel and narrow ghost lines were observed. In the coarse-grained HAZ, more lower bainite was observed and some local martensite grains were found. However, according to the hardness measurements, the amount of martensite is considered more or less harmless. Acicular ferrite dominates in the as-welded microstructure and, between the columnar grains of the solidification structure, grain boundary ferrite is found. The reheated microstructure contains mainly polygonal ferrite, some grain boundary ferrite, and remains of acicular ferrite. In the SEM observations, interdendritic and intergranular brittle-like fracture surfaces were found in the solidification structure, as the obvious crack propagation paths are along the grain boundary ferrite.

The brittle fracture characterisation was started with the Charpy V-notch impact toughness test, from which nine brittle specimens were chosen for fractography. The obtained transition temperature was -75 °C, hence the brittle fracture specimens had testing temperatures below that down to -119.5 °C. The impact energies range from 41.9 J down to 4.6 J. In the SEM analysis, the primary initiation sites were found at some distance

from the V-notch and the primary fracture mode was cleavage fracture. In all investigated specimens, a particle had initiated the fracture and the location was found at the surface of both specimen halves. The initiating particles were usually on a scale 0.5–2.5 μm. The semi-quantitative chemical composition was measured using EDS from the location of the initiation site. According to the elemental analysis using EDS, the particles consisted of mainly manganese, aluminium, silicon, and oxygen. The inclusion analysis defined the size and density of particles within the weld metal. The most probable inclusion size in the as-welded region is 0.23 μm, while that in the reheated region is 0.27 μm. The inclusions in the as-welded and reheated microstructures were similar and mainly roundish oxide particles were found. The chemical analysis confirmed the complex-phase, manganese-rich oxide particles, which are inherently brittle particles. Small amount of ductile manganese-sulphur particles were also found.

The initiating particles were always the biggest particle within the area of the maximum crack driving force. Hence, the larger the particle, the lower impact energy was required for crack initiation and the location was then closer to the V-notch. After the fractography, the CVN specimens were cut into cross-sections as close to the primary initiation site as possible and the microstructure around the V-notch, i.e., at the initiation site, was concluded to be as-welded microstructure in all specimens.

REFERENCES

[1] U. Zerbst, R. Ainsworth, H. Beier, H. Pisarski, Z. Zhang, K. Nikbin, T. Nitschke-Pagel, S. Münstermann, K. P. and D. Klingbeil. Review on fracture and crack propagation in weldments - A fracture mechanics perspective. *Engineering Fracture Mechanics* 132 (2014), 200–276.

[2] P. Haušild, C. Berdin and P. Bompard. Prediction of cleavage fracture for a low-alloy steel in the ductile-to-brittle transition temperature range. *Materials Science and Engineering: A* 391 (2005). DOI: 10.1016/j.msea.2004.08.067, 188–197.

[3] J. Lamarsh and A. Baratta. *Introduction to Nuclear Reactor Theory*. 3rd ed. Prentice Hall, 2001.

[4] J. Roudén. Personal communication. 2018.

[5] C. Liu, D. Northwood and S. Bhole. Inclusions and fracture in submerged arc welds of carbon-manganese pressure vessel steels. *Key Engineering Materials*. Vol. 233–236. 2003, 139–144.

[6] D. Porter and K. Easterling. *Phase Transformations in Metals and Alloys*. 2nd ed. Chapman & Hall, 1992.

[7] H. Bhadeshia and R. Honeycombe. *Steels: Microstructure and Properties*. 4th ed. Elsevier Ltd, 2017.

[8] *ASM Handbook, Vol. 6: Welding, Brazinf and Soldering*. ASM International, 1993.

[9] R. J. Messler. *Principles of Welding - Processes, Physics, Chemistry, and Metallurgy*. Wiley-VCH, 2004.

[10] S. Kou. *Welding Metallurgy*. 2nd ed. Wiley, 2003.

[11] L. Allgood. Submerged Arc Welding. *ASM Handbook, Vol. 6A: Welding Fundamentals and Processes*. Ed. by T. Lienert, T. Siewert, S. Babu and A. V. ASM International, 2011, 335–343.

[12] J. Lukkari. Hitsien laatu ja hitsausvirheet. *Hitsausuutiset* 1 (2000).

[13] S. Knostman. Shielded Metal Arc Welding. *ASM Handbook, Vol. 6A: Welding Fundamentals and Processes*. Ed. by T. Lienert, T. Siewert, S. Babu and A. V. ASM International, 2011, 302–308.

[14] G. Evans. Effect of Manganese on the Microstructure and Properties of All-Weld-Metal Deposits. *Welding Journal* (1980), 64–75.

[15] G. Evans and N. Bailey. *Metallurgy of Basic Weld Metal*. Abington, 1997.

[16] H. Miekk-oja. *Metallioppi*. 4th ed. Otava, 1972.

[17] J. Perepezko and M. Uttormark. Undercooling and Nucleation during Solidification. *ISIL International* 35 (1995). DOI: 10.2355/isijinternational.35.580, 580–588.

[18] M. Ashby and K. Easterling. A first report on diagrams for grain growth in welds. *Acta Metallurgica* 30 (1982), 1969–1978.

[19] S. Liu and D. Olson. The Role of Inclusions in Controlling HSLA Steel Weld Microstructures. *Welding Journal* (1986), 139–149.

[20] A. Glover, J. McGrath and N. Eaton. Toughness Characterization and Specifications for HSLA and Structural Steels. Ed. by P. Manganon. Metallurgical Society of AIME, NY, 1977, 143–160.

[21] S. Druce, G. Gage and G. Jordan. Effect of ageing on properties of pressure vessel steels. *Acta Metallurgia* 34 (1986), 641–652.

[22] R. Xing, D. Yu, G. Xie, Z. Yang, X. Wang and X. Chen. Effect of Thermal Ageing on Mechanical Properties of a Bainitic Forging Steels for Reactor Pressure Vessel. *Materials Science and Engineering: A* 720 (2018). DOI: 10.1016/j.msea.2018.02.036, 169–175.

[23] W. Corwin, R. Nanstad, D. Alexander, R. Stoller, J. Wang and G. Odette. *Thermal embrittlement of reactor vessel steels*. Oak Ridge National Lab. No.CONF-950804–3. 1995.

[24] B. Gurovich, K. E.A, Y. Shtrombakh, O. Zabusov and E. Krasikov. Intergranular and intragranular phosphorus segregation in Russian pressure vessel steels due to neutron irradiation. *Journal of Nuclear Materials* 279 (2000). DOI: 10.1016/S0022-3115(00)00007-6, 259–272.

[25] P. Joly, L. Sun, P. Efsing, J. Massoud, F. Somville, R. Gerard, Y. An and J. Bailey. Characterization of in service thermal ageing effects in base materials and welds of the pressure vessel of a decommissioned PWR pressurizer, after 27 years of operation. to be published in the 19th International Conference on Environmental Degradation of Materials in Nuclear Power Systems. 2019.

[26] K. Lindgren. Effects of Irradiation and Thermal Ageing on the Nanoscale Chemistry of Steel Welds. PhD thesis. Gothenburg, Sweden: Chalmers University of Technology, 2018.

[27] B. Gurovich, E. Kuleshova, Y. Nikolaev and Y. Shtrombakh. Assessment of relative contributions from different mechanisms to radiation embrittlement of reactor pressure vessel steels. *Journal of Nuclear Materials* 246 (1995), 91–120.

[28] R. Hertzberg, R. Vinci and H. J.L. *Deformation and Fracture Mechanics of Engineering Materials*. 5th ed. Wiley, 2013.

[29] M. Wechsler. Radiation embrittlement in the pressure-vessel steels of nuclear power plants. *Journal of the Minerals, Metals & Materials Society* 41 (1989), 7–14.

[30] B. Margolin, V. Shvetsova, A. Gulenko and E. Nesterova. Brittle fracture local criterion and radiation embrittlement of reactor pressure vessel steels. *Strength of Materials* 42 (2010), 506–527.

[31] W. Callister Jr and D. Rethwisch. *Materials Science and Engineering*. 9th ed. Wiley, 2014.

[32] T. Anderson. *Fracture Mechanics Fundamentals and Applications*. 2nd ed. CRC Press, Inc., 1995.

[33] G. Krauss. *Steels: Processing, Structure, and Performance*. 2nd ed. ASM International, 2015.

[34] P. Błoński and K. A. Structural, electronic, and magnetic properties of bcc iron surfaces. *Surface Science* 601 (2007), 123–133.

[35] C. Ersland, I. Vatne and C. Thaulow. Atomistic modeling of penny-shaped and through-thickness cracks in bcc iron. *Modelling and Simulation in Materials Science and Engineering* 20 (2012).

[36] P. Yan, Ö. Güngör, P. Thibaux and H. Bhadeshia. Tackling the toughness of steel pipes produced by high frequency induction welding and heat-treatment. *Materials Science and Engineering: A* 528 (2011). DOI: 10.1016/j.msea.2011.07.034, 8492–8499.

[37] A. Griffith. The phenomena of rupture and flow in solids. *Philosophical Transactions of the Royal Society* A 221 (1920), 163–197.

[38] C. Inglis. Stresses in a plate due to the presence of cracks and sharp corners. *Proceedings* 55 (1913), 219–241.

[39] E. Orowan. Fatigue an Fracture of Metals. Cambridge, MA: MIT Press, 1950, 139.

[40] D. François, A. Pineau and A. Zaoui. *Mechanical Behaviour of Materials, Vol II: Fracture Mechanics and Damage*. 2nd ed. Springer, 2013.

[41] C. Crussard, R. Borione, J. Plateau, Y. Morillon and F. Maratray. A Study of Impact Tests and the Mechanism of Brittle Fracture. *Journal of the Iron Steel Institute* 183 (1956), 147–77.

[42] A. Cottrell and B. Bilby. Dislocation Theory of Yielding and Strain Ageing of Iron. *Proceedings of the Physical Society. Section A* 62 (1949). DOI: 10.1088/0370-1298/62/1/308, 49–62.

[43] D. Sarma, A. Karasev and P. Jönsson. On the role of non-metallic incluisons in the nucleation of acicular ferrite in steels. *ISIJ International* 49 (2009). DOI: 10.2355/isijinternational.49.1063, 1063–1074.

[44] K. Wallin. *Fracture Toughness of Engineering Materials - Estimation and Application*. EMAS, 2011.

[45] J. Landes and D. Shaffer. Statistical Characterization of Fracture in the Transition Regime. *Fracture Mechanics* (1980), 368–382.

[46] W. Weibull. A Statistical Theory of the Strength of Materials. *Proceedings* 151 (1939).

[47] W. Weibull. The Phenomenon of Rupture in Solids. *Proceedings* 153 (1939).

[48] W. Weibull. A Statistical Distribution Function of Wide Applicability. *Journal of Applied Mechanics* 18 (1951), 293–297.

[49] *ASTM E1921-15a Standard Test Method for Determination of Reference Temperature, T_0, for Ferritic Steels in the Transition Range*. Standard. ASTM International, 2016.

[50] K. Wallin. Objective comparison of the Unified Curve and Master Curve methods. *International Journal of Pressure Vessels and Piping* 122 (2014), 31–40.

[51] H. Kerr. A review of factors affecting toughness in welded steels. *International Journal of Pressure Vessels and Piping* 4 (1976), 119–141.

[52] *ISO 6507-1:2018 Metallic Materials - Vickers Hardness Test - Part 1: Test Method*. Standard. Finnish Standards Association, 2018.

[53] M. Van Landingham. Review of Instrumented Indentation. *Journal of Research of the National Institute of Standards and Technology* 108 (2003). DOI: 10.6028/jres.108.024, 249–265.

[54] C. Rios, A. Coelho, W. Batista, M. Goncalves and R. Caram. ISE and fracture toughness evaluation by Vickers hardness testing of an Al3Nb-Nb2Al-AlNbNi in situ composite. *Journal of Alloys and Compounds* 472 (2009), 65–70.

[55] U. Ehrnstén and J. Lydman. Personal communication. 2019.

[56] G. Vander Voort. Light Microscopy. *ASM Handbook, Vol. 9: Metallography and Microstructures*. ASM International, 2004, 332–354.

[57] H. Exner and W. S. Scanning Emissiom Microscopy. *ASM Handbook, Vol. 9: Metallography and Microstructures*. Ed. by G. Vander Voort. ASM International, 2004, 355–367.

[58] *ISO 148-1:2016 Metallic Materials - Charpy Pendulum Impact Test - Part 1: Test Method*. Standard. Finnish Standards Association, 2016.

[59] *ASTM E23 -18 Standard Test Methods for Notched Bar Impact Testing of Metallic Materials*. Standard. ASTM International, 2018.

[60] Z. Que. Personal communication. 2019.

[61] J. Arnold. The Cause and Effect of ”Ghost Lines” in Large Steel Forgings. *Proceedings of the Institution of Mechanical Engineers* 89 (1915), 653–700.

[62] S. Jones and H. Bhadeshia. Competitive Fromation of Inter- and Intragranularly Nucleated Ferrite. *Metallurgical and Materials Transactions A* 28A (1997), 2005–2013.

[63] L. Sirkiä, J. Lydman, U. Ehrnstén and S. Lindqvist. Determination of T0 with Miniature C(T) Specimens for a High-Ni Weld Metal used in a Boiling Water Reactor Pressure Vessel. *Baltica XI Conference*. 2019.

[64] K. Wallin, M. Yamamoto and U. Ehrnstén. Location of Initiation Sites in Fracture Toughness Testing Specimens - The Effect of Size and Side Grooves. *ASME 2016 Pressure Vessels and Piping Conference*. Vol. 1B. American Society of Mechanical Engineers ASME, 2016. DOI: 10.1115/PVP2016-63078.

[65] P. Arffman. Personal communication. 2019.

[66] G. Odette and R. Nanstad. Predictive reactor pressure vessel steel irradiation embrittlement models: Issues and opportunities. *Journal of The Minerals, Metals & Materials Society* 61 (2009), 17–23.

[67] K. Lindgren, M. Boåsen, K. Stiller and P. Efsing. Evolution of precipitation in reactor pressure vessel steel welds under neutron irradiation. *Journal of Nuclear Materials* 488 (2017), 222–230.

[68] J. Shim, Y. Oh, J. Suh, Y. Cho, J. Shim, J. Byun and D. Lee. Ferrite nucleation potency of non-metallic inclusions in medium carbon steels. *Acta Materialia* 49 (2001). DOI: 10.1016/S1359-6454(01)00134-3, 2115–2122.

[69] Y. Nikolaev, A. Nikolaeva, A. Kryukov and Y. Korolyov. Radiation embrittlement and thermal annealing behavior of Cr-Ni-Mo reactor pressure vessel materials. *Journal of Nuclear Materials* 226 (1995), 144–155.

A CHEMICAL COMPOSITION FROM OES ANALYSES

Rewritten results from the original OES Analyses seen on the next pages.

Specimen	Weld Metal Composition %																	
	C	Si	Mn	S	P	Cr	Ni	Mo	Cu	Al	W	V	Ti	Co	B	Fe
3S2 measurement 1	0,051	0,15	1,43	0,008	0,009	0,03	1,58	0,41	0,06	0,024	<0,01	0,006	0,003	0,020	0,0003	base
3S2 measurement 2	0,056	0,14	1,42	0,006	0,008	0,03	1,46	0,41	0,06	0,023	<0,01	0,006	0,003	0,020	0,0003	base
3S2 measurement 3	0,060	0,15	1,38	0,007	0,008	0,04	1,49	0,41	0,06	0,022	<0,01	0,006	0,003	0,020	0,0003	base
3S2 measurement 4	0,055	0,15	1,42	0,006	0,008	0,03	1,47	0,42	0,06	0,021	<0,01	0,006	0,003	0,020	0,0002	base
3S2 measurement 5	0,058	0,16	1,46	0,007	0,008	0,03	1,48	0,41	0,06	0,024	<0,01	0,006	0,003	0,020	0,0002	base
3S2 measurement 6	0,064	0,17	1,45	0,007	0,008	0,04	1,41	0,42	0,06	0,027	<0,01	0,006	0,003	0,020	0,0002	base
3S2 measurement 7	0,038	0,25	1,36	0,006	0,007	0,03	1,20	0,37	0,04	0,002	<0,01	0,020	0,004	0,018	0,0002	base
3S2 measurement 8	0,035	0,25	1,39	0,007	0,007	0,03	1,24	0,36	0,03	0,002	<0,01	0,021	0,003	0,018	0,0002	base

Specimen	Base Material Composition %																
	C	Si	Mn	S	P	Cr	Ni	Mo	Cu	Al	W	V	Ti	Co	As	B	Fe
3S1 measurement 1	0,15	0,16	1,40	0,005	0,004	0,13	0,63	0,48	0,10	0,015	<0,01	0,004	0,002	0,023	0,033	0,0002	base
3S1 measurement 2	0,16	0,16	1,41	0,005	0,004	0,13	0,64	0,48	0,10	0,015	<0,01	0,004	0,002	0,023	0,034	0,0002	base
3S1 measurement 3	0,15	0,16	1,41	0,006	0,004	0,13	0,64	0,49	0,10	0,013	<0,01	0,004	0,002	0,023	0,035	0,0002	base

eurofins | Expert Services
PL 47, 02151 Espoo, Finland, Puh. 020 722 111
Y-tunnus: 2297513-2

ANALYYSITODISTUS
Optinen emissiospektrometri ARL iSpark 8860
(Sisäinen menetelmä: "Metallinäytteiden analysointi ARL 8860 -laitteella")

No. EUFI29-19003352-T1
Sivuja 1/1

Tilaaja: Teknologian tutkimuskeskus VTT Oy / Jari Lydman
Saapumispäivä: 19.6.2019

Tilaus: VTT Jari Lydman, 18.6.2019, til. nro. 693324
Analysointipäivä: 20.6.2019

Näyte	Koostumus %																Anal. n:o.
	C	Si	Mn	S	P	Cr	Ni	Mo	Cu	Al	W	V	Ti	Co	B	Fe	
Brute 3S2 1.mittaus	0,051	0,15	1,43	0,008	0,009	0,03	1,58	0,41	0,06	0,024	<0,01	0,006	0,003	0,020	0,0003	(loput)	138/19
Brute 3S2 2.mittaus	0,056	0,14	1,42	0,006	0,008	0,03	1,46	0,41	0,06	0,023	<0,01	0,006	0,003	0,020	0,0003	(loput)	139/19
Brute 3S2 3.mittaus	0,060	0,15	1,38	0,007	0,008	0,04	1,49	0,41	0,06	0,022	<0,01	0,006	0,003	0,020	0,0003	(loput)	140/19
Brute 3S2 4.mittaus	0,055	0,15	1,42	0,006	0,008	0,03	1,47	0,42	0,06	0,021	<0,01	0,006	0,003	0,020	0,0002	(loput)	141/19
Brute 3S2 5.mittaus	0,058	0,16	1,46	0,007	0,008	0,03	1,48	0,41	0,06	0,024	<0,01	0,006	0,003	0,020	0,0002	(loput)	142/19
Brute 3S2 6.mittaus	0,064	0,17	1,45	0,007	0,008	0,04	1,41	0,42	0,06	0,027	<0,01	0,006	0,003	0,020	0,0002	(loput)	143/19
Brute 3S2 7.mittaus	0,038	0,25	1,36	0,006	0,007	0,03	1,20	0,37	0,04	0,002	<0,01	0,020	0,004	0,018	0,0002	(loput)	144/19
Brute 3S2 8.mittaus	0,035	0,25	1,39	0,007	0,007	0,03	1,24	0,36	0,03	0,002	<0,01	0,021	0,003	0,018	0,0002	(loput)	145/19

ilac-MRA FINAS Finnish Accreditation Service T001 (EN ISO/IEC 17025)

Espoo, 27.6.2019
Eurofins Expert Services Oy

Vastaava testaaja Jouni Penttilä

Asiantuntija Juuso Perolainen

Tulos pätee vain analysoiduille näytteille.
Mittausepävarmuustaulukko toimitetaan pyydettäessä.

eurofins | Expert Services
P.O.Box 47, FI-02151 Espoo, Finland, Phone +358 20 722 111
Value Added Tax (VAT) No. FI 2297513-2

CERTIFICATE OF ANALYSES
Optical Emission Spectrometer ARL iSpark 8860
(In-house method: "*Analysis of metal samples on ARL8860 iSpark OES device*")

No. EUFI29-19003960-T1

Page 1/2

Requested by: VTT Technical Research Centre of Finland Ltd./ Jari Lydman

Date of reception: 6.8.2019

Order: VTT order 7.8.2019, number 694862

Date of analyses: 7.8.2019

Sample	Chemical composition %																Anal. n:o.
	C	Si	Mn	S	P	Cr	Ni	Mo	Cu	Al	W	V	Ti	Co	As	B	
Brute 3S1 1.	0.15	0.16	1.40	0.005	0.004	0.13	0.63	0.48	0.10	0.015	<0.01	0.004	0.002	0.023	0.033	0.0002	170/19
Brute 3S1 2.	0.16	0.16	1.41	0.005	0.004	0.13	0.64	0.48	0.10	0.015	<0.01	0.004	0.002	0.023	0.034	0.0002	171/19
Brute 3S1 3.	0.15	0.16	1.41	0.006	0.004	0.13	0.64	0.49	0.10	0.013	<0.01	0.004	0.002	0.023	0.035	0.0002	172/19
	Fe																
Brute 3S1 1.	(base)																170/19
Brute 3S1 2.	(base)																171/19
Brute 3S1 3.	(base)																172/19

ilac-MRA FINAS Finnish Accreditation Service T001 (EN ISO/IEC 17025)

Espoo, 9.8.2019
Eurofins Expert Services Oy

Senior Laboratory Technician Jouni Penttilä

Business Development Manager Laura Salminen

The results are valid only for the tested samples.

B INCLUSION ANALYSIS

Table B.1. *The fields analysed for incluison size distribution of each sample.*

Field	As-welded			Reheated		
	Avg.Diam. (μm)	Amount of Inclusions	Density Parts/mm^2	Avg.Diam. (μm)	Amount Inclusions	Density Parts/mm^2
1	0.30	168	40965	0.37	87	21210
2	0.31	115	28036	0.34	99	24153
3	0.26	169	41200	0.34	116	28279
4	0.30	199	48514	0.28	123	29986
5	0.28	153	37300	0.29	92	22429
6	0.32	171	41688	0.30	99	24035
7	0.26	200	48758	0.35	101	24623
8	0.28	164	39981	0.33	130	31691
9				0.33	113	27547
Total/Avg.	0.288	1339	40805	0.325	960	25995

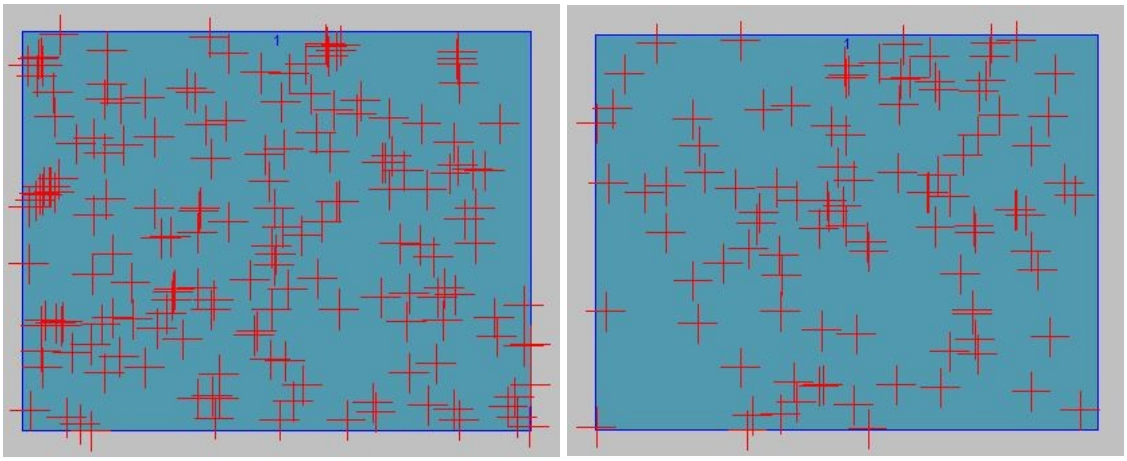

Figure B.1. *Comparison of the inclusion density between as-welded (left) and reheated (right) regions.*